Chavkat Akhmadaliev

Investigation of acoustic waves generated in an elastic solid by a pulsed ion beam and their application in a FIB based scanning ion acoustic microscope

Chavkat Akhmadaliev

Investigation of acoustic waves generated in an elastic solid by a pulsed ion beam and their application in a FIB based scanning ion acoustic microscope

**Forschungszentrum
Rossendorf**

Investigation of acoustic waves generated in an elastic solid by a pulsed ion beam and their application in a FIB based scanning ion acoustic microscope

vorgelegt von
Dipl.-Phys. Chavkat Akhmadaliev

geboren am 23. Mai 1973
in Angren (Taschkent Bez., Uzbekistan, ehem. UdSSR)

Contents

IV

1. Introduction

The rapid growth of the microelectronics industry in the last decades made it possible to produce structures in the sub-micrometer scale on silicon chips and to reach an integration scale under 100 nm. Decreasing the size and increasing the complexity of these structures make a control of quality and defects investigation more difficult. During a long time ultrasound devices are being used for nondestructive investigation of materials, like ultrasound microscopes, scanning photo-acoustic microscopes or scanning electron acoustic microscopes, where acoustic waves are generated by acoustic transducers, focused laser or electron beams, respectively.

Generation of elastic waves in solids by an incident electron or laser beam has got a wide application in nondestructive materials inspection since the early work of White [1]. They can provide a resolution in the micrometer range, but due to the properties of the used beams they have natural limitations of resolution like limited spot size of the focused laser beam because of diffraction and proximity effect in the case of focused electron beam [2]. The generation of acoustic wave in solids by pulsed laser beams has been widely investigated theoretically [1, 3, 4] and experimentally [4-12]. The first attempt to apply ion beams for acoustic microscopy was done by Rose et al. [13] in the 80's, using a broad ion beam implanter. Also several reports were published concerning the ion induced emission of elastic waves in solids using energetic pulsed ion beams [10, 11, 15, 16] and low energy focused ion beam [14].

The aim of this work is to investigate more precisely the acoustic wave generation by pulsed and periodically modulated ion beams in different solid materials depending on the beam parameters and to demonstrate the possibility to apply an intensity modulated focused ion beam (FIB) for acoustic emission and for nondestructive investigation of the internal structure of materials on a microscopic scale. The combination of a FIB and an ultrasound microscope in one device can provide the opportunity of nondestructive investigation, production and modification of micro- and nanostructures simultaneously. The FIB spot size in modern systems is comparable with that of a focused electron beam

and the penetration depth of ions with energy of 20-60 keV is lower than 100 nanometers. This makes it possible to reach a sub-micrometer resolution of a scanning ion acoustic microscope. On the other hand side a FIB with energy of 20-60 keV is a good tool which can be used for the fabrication of nanostructures using ion milling, implantation or ion beam assisted deposition techniques. A FIB system with a liquid metal alloy ion source and a mass separator provides different ion species which can have a variance of sputtering efficiency.

This work consists of the two main experimental parts. In the first part the process of elastic wave generation during the irradiation of metallic samples by a pulsed beam of energetic ions was investigated in an energy range from 1.5 to 10 MeV and pulse durations of 0.5 - 5 µs, applying ions with different masses, e.g. oxygen, silicon and gold, in charge states from 1+ to 4+. The acoustic amplitude dependence on the ion beam parameters like the ion mass and energy, the ion charge state, the beam spot size and the pulse duration were of interest. The main difficulty is to have sufficient current of the ion beam in order to generate a measurable signal on the sample. The ions listed above were chosen due to their highest beam current yielded by the Rossendorf ion accelerators. This work deals with ultrasound transmitted in a solid, i.e. bulk waves, because of their importance for acoustic transmission microscopy and nondestructive inspection of internal structure of a sample.

The second part of this work was carried out using the IMSA-100 FIB system operating in an energy range from 30 to 70 keV. The ion current in the FIB is only some nanoamperes, therefore for the detection of fine vibrations initiated by the beam a special low-noise data acquisition system was used. The scanning ion acoustic microscope based on this FIB system was developed and tested.

2. Interaction of an ion beam with a solid

Energetic ion beams have found broad applications in modern industry and science due to their ability to penetrate deeply into target materials and to change their properties. Some of the processes taking place during the interaction of an ion with a solid, which are important for understanding of the generation of acoustic waves in the target, are briefly described in this chapter.

2.1. Ion stopping in a solid

The energetic projectile ion traveling in a solid medium dissipates kinetic energy on its way via interaction with atomic nuclei, atomic electrons and, in the case of an electrical conductor also with conduction electrons, until the ions are stopped. There are basically four main types of interaction of which only two are significant:

1) Inelastic electronic collisions including ionization,

2) Elastic electronic collisions,

3) Inelastic nuclear collisions leading to Bremsstrahlung, nuclear excitations and reactions,

4) Elastic nuclear collisions with whole or part of the kinetic energy of the incident ions imparted to the atoms or nuclei.

From these, only elastic nuclear collisions and inelastic electronic collisions contribute significantly. During elastic interactions the total momentum and kinetic energy of the system of interacting particles are conserved, inelastic interactions conserve the total momentum but not the kinetic energy. The nuclear collisions dominate at low energies while the electronic collisions predominate at higher energies. The ions are stopped in a certain depth in the target material depending on the sample properties and the ion mass and energy. Interaction of the ions with the target leads to alteration of the material structure and modification of the sample surface and the subsurface region.

2.1.1. Energy loss

The energy loss occurs due to interaction with target electrons and atoms and leads to slowing down of the energetic ion. The penetrating ion in the solid loses the energy to the electrons and rarely collides with nuclei of the target atoms. These collisions can be strong enough to displace the atoms and create vacancies. The recoiling atoms may have adequate energy to start a collision cascade by displacing other target atoms up to final stopping. The energy loss dE per unit path length dR has electronic and nuclear contributions and, assuming that these two stopping processes are independent, it can be expressed as the stopping power:

$$\left(\frac{dE}{dR}\right)_{total} = \left(\frac{dE}{dR}\right)_{E} + \left(\frac{dE}{dR}\right)_{N} \tag{2.1}$$

One of these components dominates depending on the energy, the charge number and the mass of the primary ions as well as on the mass and the charge number of target atoms. High energy ions are slowed down by electronic collisions and at low energies nuclear collisions are dominating, i. e. an ion with initially high velocity is slowed down by electrons, the trajectory is a straight line and at the final part of the path it is stopped by the nuclear interaction which can strongly deflect the ion's trajectory (Fig. 2.1). The total stopping cross section S is defined as the stopping power divided by the atomic density of the target, n:

$$S = -\frac{1}{n} \cdot \left(\frac{dE}{dR}\right) = S_{E} + S_{N} \tag{2.2}$$
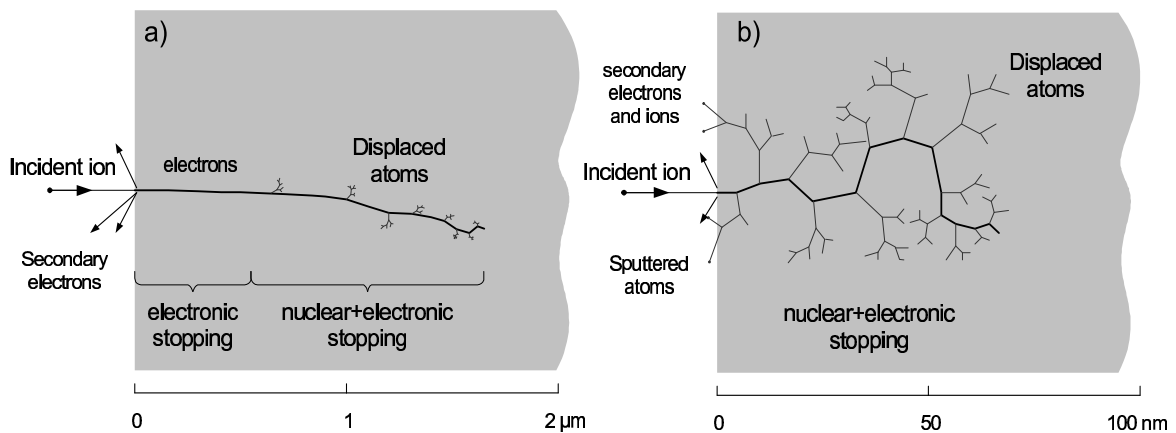
Fig. 2.1. Illustration of a high energy light (a) and a low energy heavy (b) ion penetrating into a solid.

2.1.1.1. Nuclear stopping

At low velocities scattering off the atomic nuclei becomes important (Fig. 2.2). The collision of a projectile ion with a target atom can be described as an interaction of two charged particles, in the binary collision approximation. The collision kinematics can be defined from atom-atom interaction potential. Unfortunately there is no analytical form of the interatomic potential which is valid for all distances. Different methods have been developed for approximation of this potential, and each of them is applicable in a certain range of distances.

For interatomic distances less than 10^{-10} m the most widely used model of the interaction potential $U(r)$ is the Thomas-Fermi potential. In this model the atom is treated as a positive nucleus surrounded by a continuous distribution of electrons [17]. Firsov obtained the Thomas-Fermi potential between two atoms as a screened Coulomb potential with a Thomas-Fermi screening function $\Phi\left(\dfrac{r}{a_F}\right)$:

$$U(r) = \frac{Z_1 Z_2 e^2}{4\pi\varepsilon_0 r} \cdot \Phi\left(\frac{r}{a_F}\right),$$ (2.5)

where Z_1 and Z_2 are charge numbers of atomic nuclei and a_F is the characteristic length
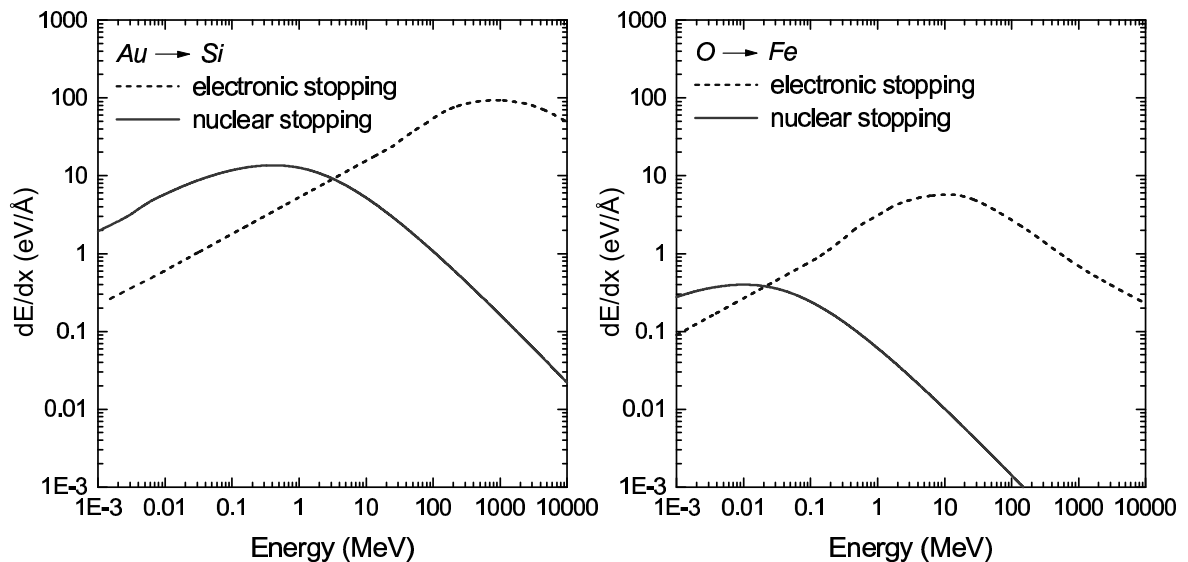
Fig. 2.2. Comparison of the energy loss by nuclear and electronic stopping for heavy ions in a light material (gold ions in silicon (a)) and for light ions in a heavy material (oxygen ions in iron) (b) calculated using the SRIM2000 code.

(screening length) given by Firsov as [18]:

$$a_F = \frac{0.47}{\left(Z_1^{1/2} + Z_2^{1/2}\right)^{2/3}} \text{Å} , \tag{2.6}$$

Several approximations of the screening function are used, like the Wedepohl approximation

$$\Phi(x) = Axe^{-kx^{1/4}} , \quad 0.3 < x < 16 , \tag{2.7}$$

the Sommerfeld approximation [19]

$$\Phi(x) = \left(1 + \left(\frac{x}{5.2}\right)^{0.8}\right)^{3.7} , \tag{2.8}$$

the Lindhard standard approximation [20]

$$\Phi(x) = 1 - \frac{x}{\sqrt{x^2 + 3}} , \tag{2.9}$$

the Molière [21] approximation

$$\Phi(x) = 0.35e^{-0.3x} + 0.55e^{-1.2x} + 0.1e^{-6x} . \tag{2.10}$$

For very short distances Bohr has proposed an exponentially screened Coulomb potential [22]:

$$U(r) = \frac{Z_1 Z_2 e^2}{4\pi\varepsilon_0 r} \exp\left(-\frac{r}{a_B}\right) , \tag{2.11}$$

where a_B is the Bohr screening parameter, given as:

$$a_B = \frac{0.53}{(Z^{2/3} + Z^{2/3})^{1/2}} \text{Å} \tag{2.12}$$

If the projectile ion suffers single elastic collisions with a target atom it loses the energy:

$$T(E, p) = \frac{4m_1 m_2}{(m_1 + m_2)^2} E \cdot \sin^2\left(\frac{\theta(p)}{2}\right) \tag{2.13}$$

where $\theta(p)$ is the deflection angle of the projectile in the center-of-mass system, p is the impact parameter, E is its kinetic energy, and m_1 and m_2 the masses of the ion and target atom, respectively. The deflection angle is calculated using the formula

$$\theta(p) = \pi - \int_{-\infty}^{\infty} \frac{p\,dr}{r^2 \sqrt{1 - \frac{U(r)}{E'} - \left(\frac{p}{r}\right)^2}} \tag{2.14}$$

with the projectile's energy in the center-of-mass system E'.

The corresponding energy loss in the nuclear collisions is defined as

$$\left(-\frac{dE}{dR}\right)_N = n\int_0^\infty T(E,p)\frac{d\sigma(T,E)}{dT}dT, \tag{2.15}$$

and the stopping cross section is

$$S_N(E) = \int T(E,p)\frac{d\sigma(T,E)}{dT}dT, \tag{2.16}$$

where σ is the scattering cross section.

2.1.1.2. Electronic stopping

As it is mentioned above, high energy ions, i.e. ions with high velocities, lose their energy in solid matter mostly via electronic stopping. Penetrating the target a projectile ion is deprived of all its own electrons and interacts with the target electrons as a bare nucleus of charge Z_1e via the Coulomb potential. The scattering can be described by the Rutherford scattering formula. The electronic stopping power can be roughly estimated using Eq.(2.15) for the Rutherford scattering cross section and electron density $n = Z_2n_2$ with atomic density of target atoms n_2 considering the projectiles to be free down to energy transfers $T = I$ and neglecting excitations:

$$\left(-\frac{dE}{dR}\right)_E = \frac{n_2Z_2Z_1^2e^4}{4\pi\varepsilon_0^2 m_e v_1^2}\ln\left(\frac{2m_e v_1^2}{I}\right), \tag{2.17}$$

where I is the mean ionization energy of the target atoms, v_1 is the ion velocity. This formula shows the basic behavior of the stopping power as $\propto Z_1^2$ and $\propto \frac{1}{v_1^2}$ which are given also by an improved theory. Generally the stopping power can be written as

$$\left(-\frac{dE}{dR}\right)_E = \frac{Z_1^2e^4}{4\pi\varepsilon_0^2 m_e v_1^2}n_2B, \tag{2.18}$$

where B is called the stopping number.

For a low energy ion, i. e. the velocity of the ion is lower than the fastest velocity of the target electrons, $v_1 \ll Z_1^{2/3}v_0$, with $v_0 = \frac{4\pi\varepsilon_0 e^2}{\hbar}$ (orbital velocity of the electron in the hydrogen atom, the Bohr velocity), the electronic stopping power is proportional to v_1 or in other words to $\sqrt{E}$ and can be described by the Firsov model which is based on Thomas-Fermi model of the atom [23] :

$$\left(-\frac{dE}{dR}\right)_E = 0.325(Z_1+Z_2)n_2\sqrt{\frac{E(\text{eV})}{A}} \quad \text{eV/Å} \qquad (2.19)$$

where A is the atomic mass of the ion. Lindhard, Scharff and Schiott use a model of a slow heavy primary ion moving in a uniform electron gas [24]. The Lindhard approach is widely cited in the literature as it formed part of the first unified theory of ion penetration in solids, and it has been widely used as the basis for calculating the electronic stopping of ions in matter. The electronic energy loss in this model can be written as

$$\left(-\frac{dE}{dR}\right)_E = \frac{8\pi a_0 e^2 Z_1^{7/6} Z_2}{4\pi\varepsilon_0 (Z_1^{2/3}+Z_2^{2/3})^{3/2}}\cdot\left(\frac{v_1}{v_0}\right) \qquad (2.20)$$

where a_0 is the Bohr radius.

At high energies, for an ion velocity $v_1 >> Z_1^{2/3}v_0$ for the calculation of the electronic stopping power the Bethe-Bloch formula should be used

$$\left(-\frac{dE}{dR}\right)_E = \frac{Z_1^2 e^4}{4\pi\varepsilon_0^2 m_e v_1^2}n_2\cdot Z_2\left[\ln\left(\frac{2m_e v_1^2}{I}\right)-\ln\left(1-\left(\frac{v_1}{c}\right)^2\right)-\left(\frac{v_1}{c}\right)^2\right], \qquad (2.21)$$

where c is light velocity. At a medium energy, where $v_1 \sim Z_1^{2/3}v_0$, for the electronic stopping power interpolation formulae proposed by Biersack [25] or by Andersen [26] can be used.

The experiments in the current work were carried out using pulsed ion beams with energies of 1 to 10 MeV, which can be considered as a medium range, where the both nuclear and electronic stopping must be taken into account, as well as with a low energetic focused ion beam (30-70 keV), where the electronic stopping doesn't play a significant role.

2.1.2. Ion range

The ions entering a solid lose energy and continuously change direction by collision with target atoms. The ion path length (range) and its projection on the ion beam direction (projected range) are random variables. The projected range denotes the depth, where most ions stop. The mean ion path length R_L in the target can be found as [27]:

$$R_L = \int_0^{E_0} \frac{dE}{(-dE/dR)_{total}} \qquad (2.22)$$
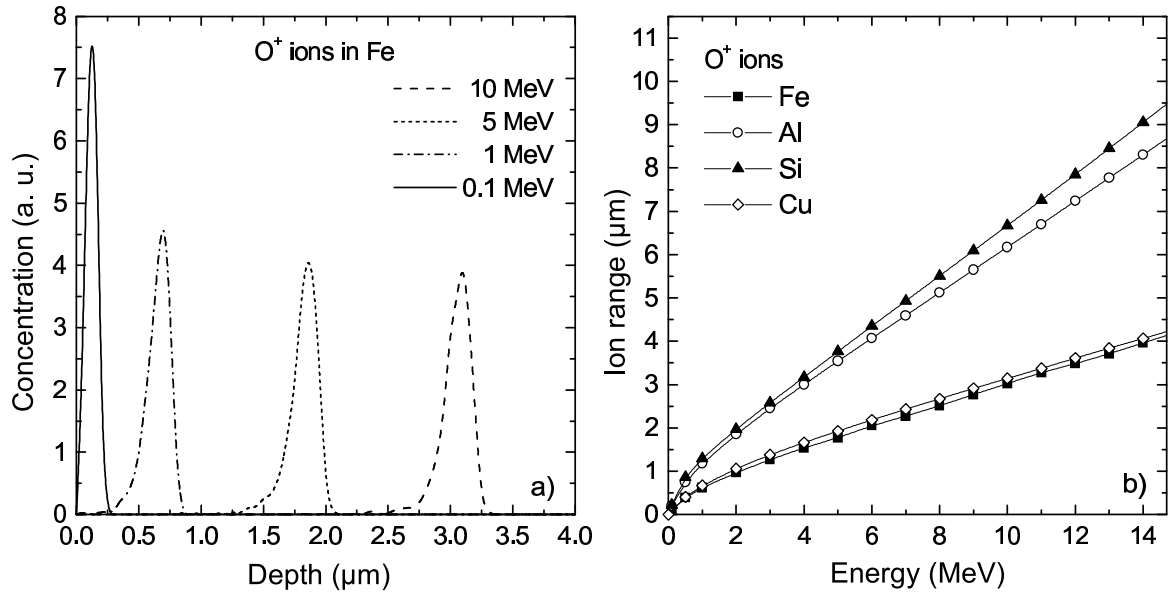
Fig. 2.3. An example of O^+ ion concentration profiles in iron target for different energies (a) and the ion ranges in different materials (b) calculated using SRIM2000 code.

For an energetic ion which exhibits mostly electronic energy loss at the beginning of the path, the ion range can be written as:

$$R_L = \int\limits_{0}^{E_S} \frac{dE}{-(dE/dR)_{total}} + \int\limits_{E_S}^{E_0} \frac{dE}{-(dE/dR)_E} \qquad (2.23)$$

where E_S is an energy limit above which only the electronic stopping can be taken into account. The implanted profile (concentration of the implanted ions) in the target is described by the mean projected range R_P, i. e. mean depth, of the implanted ions:

$$R_P = \frac{1}{N}\sum\limits_{k}^{N} z_k \qquad (2.24)$$

where the z_k is the depth of the k-th ion implanted in the target, N is the number of implanted ions.

Due to the statistical nature of the ion stopping process the implanted dopant concentration $n_D(z)$ in amorphous target can be approximated by Gaussian distribution:

$$n_D(z) = \frac{D}{\sqrt{2\pi}\Delta R_P} \exp\left[-\frac{(z - R_P)^2}{2\Delta R_P^2} \right] \qquad (2.25)$$

here D is the implanted dose and ΔR_P is the statistical fluctuation of the projected range R_P, projected straggle.

Fig. 2.3 shows an example of oxygen ion depth profiles in an iron target for different energies. The profile from low energy ions reside close to the surface, the higher energy ions penetrate deeper in to the sample. For energies lower than some hundred keV there are a lot of ions with the final position close to the target surface. This means that some of the ions and the displaced target atoms can leave the sample, i. e. become reflected or sputtered, respectively. For ions in the keV-range, depending on mass, dose and angle of incidence the sputtering effect must be included in the profile calculations.

2.2.   Radiation damage

Collisions between projectile ions and target atoms lead to displacements of atoms from lattice sites in a crystalline solid. This forms unoccupied lattice sites, i. e. vacancies, and interstitial atoms. Combination of both creates an interstitial-vacancy pair (Frenkel pair). Such defects in a crystal are referred to be point defects. The implanted ion itself finally occupies an interstitial or a vacancy position in the lattice as an impurity atom. If a displaced atom has enough energy, it can displace other lattice atoms from their normal sites before coming to rest. These atoms can in turn displace further atoms forming a displacement cascade. The time scale of the developing cascade is about 10^{-13} s. During such a fast process of energy transfer the small volume around the projectile trajectory is heated up to a very high temperature (thermal spike). A displacement cascade in a simplified model is described by the number of displacements or Frenkel pairs N_d taking place in the cascade. A rough value of this number was obtained by Kinchin and Pease assuming that the displacement requires a sharp energy threshold E_d and the ion energy is high enough, $E_0 >> E_d$, neglecting inelastic energy loss [28]

$$N_d(E_0) = \frac{E_0}{2E_d} \qquad (2.26)$$

for a primary knock-on atom with energy E_0. The displacement threshold energy is the energy required for a target atom to be permanently removed from its original location. For most of the materials the threshold energy is in the range of 15 - 80 eV. Equation (2.26) assumes that the projectile and the target atoms experience only elastic binary collisions and the scattering is thought to be made up of hard-sphere collisions, that is, the particles are viewed as classical "billiard balls". Taking into account inelastic energy losses the formula for the number of displacement can be modified [29]:

$$N_d(E_0) = \xi \frac{E_0 - E_{inel}}{2E_d} \tag{2.27}$$

where E_{inel} is the total inelastic energy loss in the cascade, a constant factor ξ represents the efficiency of the displacement process and describes the loss of Frenkel pairs by dynamic annealing in the dense cascades.

2.3. Sputtering

The ion implantation usually is accompanied by sputtering – the escape of target atoms or atomic clusters from the surface due to physical knock-on processes caused by an incident ion. When a cascade transmits energy higher than the surface binding energy to a target atom close to the surface, the atom can be sputtered. This process is described by the sputtering yield, i. e. the mean number of particles escaping from the surface by a single projectile ion. It depends on the ion mass, energy and the angle of incidence as well as the properties of the target material and it is very sensitive to the surface binding energy. The classical model for calculation of the sputtering yield as a function of ion energy E was proposed by Sigmund [30]:

$$Y(E) = \frac{3}{4\pi^2 c_0} \cdot \frac{1}{U_0} \alpha\left(\frac{M_2}{M_1}\right) S_n(E) \frac{1}{\cos^n(\theta)} \tag{2.28}$$

where U_0 surface binding energy, $S_n(E)$ nuclear stopping cross section at the ion energy E, $\alpha\left(\dfrac{M_2}{M_1}\right)$ is numerical function of ratio of target atom mass M_1 to ion mass M_2 which can be approximated by a polynomial function, c_0 is a constant, n a fit parameter depending weakly on the mass ratio and lying between 1 and 2, θ the angle of incidence. Equation (2.28) has a pole at 90° (ions moving parallel to the target surface), so this expression is valid only for angles smaller than 60-70°. In order to overcome the dilemma of this pole Yamamura et al. [31] proposed to introduce in Sigmund's model an exponential term:

$$Y(E,\theta) = Y(E,0) \cdot \frac{\exp\left(f \cdot \left(1 - \frac{1}{\cos(\theta)}\right)\cos(\theta_{opt})\right)}{\cos^n(\theta)} \tag{2.29}$$

where f is a function of U_0, M_1 and M_2, θ_{opt} is the angle where the sputtering has a maximum. Increasing the ion energy the sputtering yield first grows, reaches the maximum
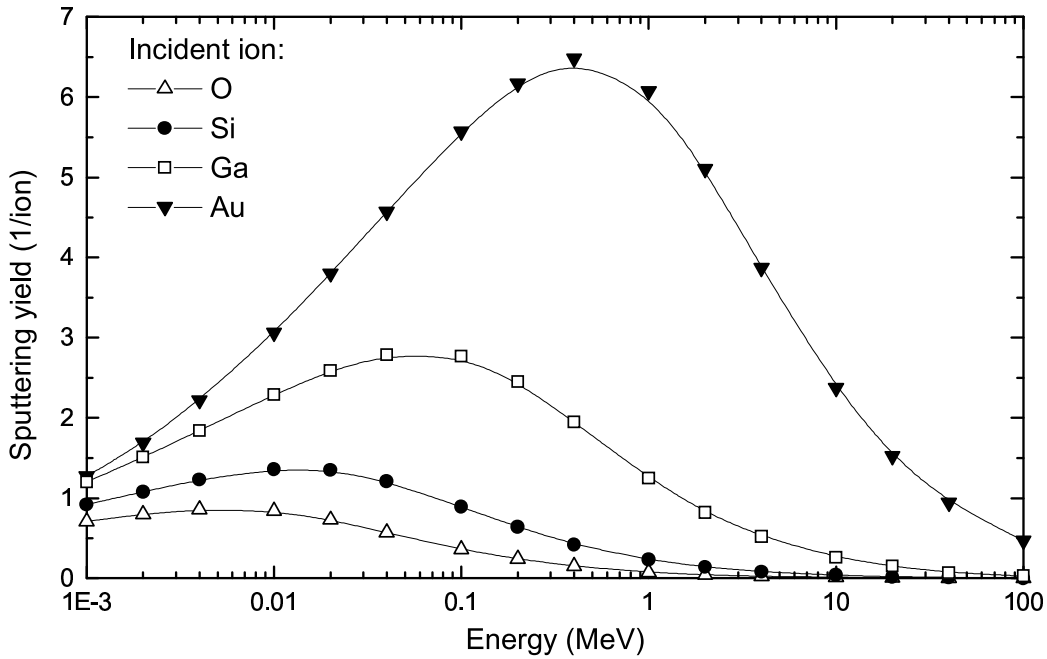
Fig. 2.4. Sputtering yield on Si for different ions as a function of energy calculated for normal incident angle using Sigmund's classical model. Heavier ions have higher yield.

value at certain energy which can be in the range from some keV to some hundreds keV depending on the ion mass and target properties, and then decreases.

For the calculation of the sputtering yield for light ions and low energies the Bohdansky formula is widely used [32]. Not only atoms and ions can be removed from the surface by the incident ions, but also secondary electrons, which are used mostly for surface imaging purposes in focused ion beam systems. The sputtering effect in terms of ion milling has found wide application in nanotechnology [33].

2.4. Channeling

The atoms in a crystalline material exhibit long range order, i. e. they form rows and planes in the crystal. Depending on the value of the incident angle of an energetic ion entering the solid, the ion motion can become constrained to the relatively open spaces in the crystal between adjacent rows of atoms along crystallographic directions with low Miller indexes. If an ion enters into this space, called a channel, the steering forces of the atomic potentials keep the ion directed along the center of this space in the target crystal, the ion can jump into an adjacent channel but keep the direction. The process of channeling of ions can greatly increase the ion range and produce significant distortions in the concentration

profiles of implanted dopants. Because of decreasing of the energy loss per unit distance channeling causes the implantation profile to penetrate deeper than for amorphous material, so the ion range can be increased by a factor of 2-50 [34-36]. The channeled ions lose their energy mainly due to electronic stopping in the target. This leads to a reduction of the losses and makes the ion range longer. There is reduced damage production by the channeled ions because of smaller probability of ion-target-atom collisions, resulting in the displacement of atoms.

There are many different oriented channels in a crystal lattice. In order to channel the target the incident ions must be well aligned to one of the channels. However, in some of the channels the amount of channeling ions is negligible, while in others it is significant. This is determined by the probability that the ion enter the channel and the capability of the channel to keep the ions in this direction. It depends on the channel opening and on the density of the atoms in the walls. The smaller opening leads to lower probability of the ions entering, the wall with higher atomic density retain the ions better and keep them in the channel. The channeling takes place if the angle of incidence of implanted ions to a channel is smaller than a critical angle, which depends on the atomic numbers of the ion and the target atoms, the ion energy and the distance between the atoms in the channel walls [37, 38]. Depending on the incident angle the implanted profile can be changed, i. e. the projected range can be deeper than for a random non-channeling case, and the concentration profile exhibits a secondary maximum or a long tail deeper in the crystal than the primary peak for random implantation [34-36, 38]. The presence of a thin layer of amorphous material on the surface of the crystal, for instance oxide layer, can reduce or even completely eliminate the ion channeling due to randomizing of the directions of incident ions passing through the layer. If the implanted dose reaches a critical value, the channeling reduces due to increasing of the damage density in the lattice, making the crystal more irregular or amorphous.

3. Generation of elastic waves in a solid by a pulsed ion beam – the ion acoustic effect

The interaction mechanisms responsible for ion induced generation of acoustic wave in a solid sample are quite manifold. Any property of the primary ion beam itself or any processes which take place during interaction of the ions with the solid and cause a mechanical deformation of the sample can initiate the acoustic signal. These processes include specimen transient heating due to dissipation of the energy of the incident ions in a material, momentum transfer from the initial ions and sputtered particles, local material modification leading to the change of volume and stresses in the sample, piezoelectric or electrostrictive effects in dielectric materials due to the charge generated by the ion beam, magnetostrictive coupling of the magnetic field of the beam in magnetic materials, direct coupling of excess charge carriers generated by the incident beam within semiconductors, and a heat contribution of these carriers during their recombination process. In the current work it will be shown that the ion induced thermal effect is the main reason of acoustic wave generation during ion bombardment.

3.1. Elastic waves in an isotropic solid medium

The theory of elasticity of solids is described in detail elsewhere [39-42]. The basics of the solid's elasticity are briefly described in the Appendix A.

In gases and liquids there is only one mode of an elastic wave with the displacement of particles parallel to the direction of sound propagation. In a solid material a variety of acoustic wave modes are possible. The wave motion in isotropic elastic solids is associated with three bulk modes of propagation which correspond to three perpendicular components, one longitudinal and two transversal (shear) to the direction of wave propagation. Each of these modes has an own characteristic velocity, although in isotropic solids the two transversal velocities are degenerate. For an infinite half-space solid, in addition to bulk longitudinal and transversal waves, Rayleigh modes must be considered

[5, 43]. For a solid plate with two free surfaces the picture becomes much more complicated by multiple reflection, mode conversion, and possibility of Lamb wave generation [44].

Hooke's law for the isotropic case can be written as [39]

$$\sigma_{ij} = \lambda \delta_{ij} \sum_k u_{kk} + 2\mu u_{ij} \, . \tag{3.1}$$

where σ_{ij} represents the stress tensor, λ and μ are Lamè elastic constants of the material, u_{lm} is the strain tensor and δ_{ij} is the Kronecker delta.

The equation of motion for the vector of displacement $\vec{u}$ is

$$\rho \frac{\partial^2 u_i}{\partial t^2} = \frac{\partial}{\partial x_k} \sigma_{ik} + f_i \tag{3.2}$$

with the mass density ρ and the resultant of body forces per unit of volume f_i. For an isotropic medium Eq. (3.2) simplifies

$$\mu \frac{\partial^2}{\partial x_k \partial x_k} u_i + (\lambda + \mu) \frac{\partial^2}{\partial x_i \partial x_k} u_k + f_i = \rho \frac{\partial^2}{\partial t^2} u_i \, , \tag{3.3}$$

or in other words

$$\mu \Delta \vec{u} + (\lambda + \mu) \vec{\nabla} \, div \, \vec{u} + \vec{f} = \rho \ddot{\vec{u}} \, . \tag{3.4}$$

Because of the following identity

$$\Delta \vec{u} = \vec{\nabla} \, div \, \vec{u} - rot \, rot \, \vec{u} \, , \tag{3.5}$$

Eq. (3.4) can be simplified by splitting the displacement vector $\vec{u}$ in two components, the longitudinal $\vec{u}_L$, and the transversal $\vec{u}_T$ ones:

$$\vec{u} = \vec{u}_L + \vec{u}_T \, , \quad rot \, \vec{u}_L = 0 \quad div \, \vec{u}_T = 0 \, . \tag{3.6}$$

Substituting the relations (3.6) into equation (3.4) and neglecting the vector of body force density $\vec{f}$ one gets:

$$\rho \frac{\partial^2 \vec{u}_L}{\partial t^2} = (\lambda + 2\mu) \vec{\nabla} \, div \, \vec{u}_L$$

$$\rho \frac{\partial^2 \vec{u}_T}{\partial t^2} = -\mu \, rot \, rot \, \vec{u}_T \tag{3.7}$$

The relations between the differentials

$$\nabla \, div \, \vec{u}_L = \Delta \vec{u}_L \qquad rot \, rot \, \vec{u}_T = -\Delta \vec{u}_T \tag{3.8}$$

provide the following wave equations for $\vec{u}_L$ and $\vec{u}_T$:

$$\frac{\partial^2 \vec{u}_L}{\partial t^2} - c_L^2 \Delta \vec{u}_L = 0,$$

$$\frac{\partial^2 \vec{u}_T}{\partial t^2} - c_T^2 \Delta \vec{u}_T = 0 \tag{3.9}$$

with wave velocities c_L and c_T given by the formulae

$$c_L = \sqrt{\frac{(\lambda + 2\mu)}{\rho}}, \qquad c_T = \sqrt{\frac{\mu}{\rho}}. \tag{3.10}$$

In Table 3.1 the Lamè coefficients λ and μ, the Young modulus Y, the density and the wave velocities for several materials are summarized [45].

In the presence of body forces the vector of force density $\vec{f}$ can also be represented as a sum of longitudinal $\vec{f}_L$ and transversal $\vec{f}_T$ vectors, so the wave equations (3.9) can be written in this case:

$$\frac{\partial^2 \vec{u}_L}{\partial t^2} - c_L^2 \Delta \vec{u}_L = \frac{\vec{f}_L}{\rho}$$

$$\frac{\partial^2 \vec{u}_T}{\partial t^2} - c_T^2 \Delta \vec{u}_T = \frac{\vec{f}_T}{\rho} \tag{3.11}$$

Finally any longitudinal vector can be expressed as a gradient of a scalar field because of Eq. (3.6) as well as any transversal vector can be expressed as a rotor of a vector field. This can be used to reduce number of equations in the system down to four.

The problem of propagation of elastic waves in a solid can be solved using several methods, for instance employing Green's function [3, 46, 47] or using the finite elements method (FEM), the boundary elements method (BEM) [48] or the method of finite differences [49].

In anisotropic media different directions in the transversal plane are not equivalent as in the case of an isotropic solid. Therefore two transversal wave modes are not degenerated and there are three possible modes of elastic waves. The phase velocities of these modes can be obtained using the common equation of motion Eq. (3.2) which leads to the

Table 3.1 *Mechanical properties of materials*

Material	ρ (kg/m^3)	Y (GPa)	λ (GPa)	μ (GPa)	v	c_L (m/s)	c_T (m/s)
Aluminum	2700	73.6	54.6	25.6	0.34	6260	3080
Iron	7870	196	112.3	78.5	0.29	5850	3230
Copper	8930	88.3	106.1	45.6	0.35	4700	2260
Silicon(amorph.)	2330	110.3	35.5	45.2	0.22	5886	3770

following wave equation for the sinusoidal wave component in a crystalline material

$$(\rho\omega^2 - k^2 c_{iklm} n_k n_l \delta_{mi})u_i = 0, \tag{3.12}$$

where k and ω are wave number and angular frequency, respectively, n_m are components of the unit propagation vector $\vec{n}$, and c_{iklm} is the tensor of elastic constants.

3.2. Acoustic emission in an isotropic solid by a pulsed ion beam

A beam of particles irradiating a surface of a solid acts mechanically on the target in several ways: first of all, the momentum of the particles is transferred to the target atoms and leads to a mechanical force in direction of the beam; secondly, the interaction of the particles with the target provides a deformation of the sample (Fig.3.1). The dissipation of the energy of the particles produces strong heat in a small region of the material leading to a thermal expansion of the volume. The heating of the surface can give rise to an evaporation of the material from the surface. Additionally the ion beam can sputter target atoms from the surface. These provide an additional momentum transfer to the target. Also the ion beam can modify the surface and subsurface region of the sample by incorporation of projectile ions which can lead to a change of the material density. All these effects give rise to elastic waves.

3.2.1. Momentum transfer

A pulse of an electron, an ion or a laser beam has a certain momentum which is transferred to the target atoms during the surface irradiation. This occurs on a time scale which is defined mostly by the pulse length and, in the case of a very short pulse, also by the time of the cascade development in the material. The momentum transfer leads to a resulting force applied to the surface of the target. This force during a pulse, provided by a beam of charged particles is given by:

$$F = \sqrt{2ME} \cdot \frac{I}{q}, \tag{3.13}$$

where E is the energy of particles, M is the mass, q is the charge of a particle in the beam, I is the beam current. As it is seen the force depends on square root of the energy. This force is localized in the small area corresponding to the beam size.

The sputtering effect during the ion beam irradiation causes an additional contribution to the momentum. The amount of the sputtered ions and generated secondary electrons depends on the ion species, their charge state and as well as the material properties, like atomic mass number and binding energy [33]. Due to low value of velocities of the sputtered particles their contribution in the total momentum transfer is negligibly small.

Impurities on the sample surface, which can be evaporated from the surface during irradiation, also provide additional momentum. The influence of laser evaporation of a liquid coating is well investigated, a review can be found in Ref. [5]. A similar surface impurity evaporation effect is expected in the case of acoustic wave generation by means of electron or ion beams.

3.2.2. Local heating

Another process which has a great importance in the sound generation is the local transient heating of the sample due to energy loss of the ions in the material. Transient local heating of a solid produces an elastic wave in the target material as a result of the motion due to thermal expansion of the heated region. The inhomogeneous temperature distribution $T(\vec{r},t)$ in an isotropic material with a bulk modulus of elasticity of $B = \lambda + \dfrac{2}{3}\mu$ and a linear thermal expansion coefficient α leads to a body force density [4]

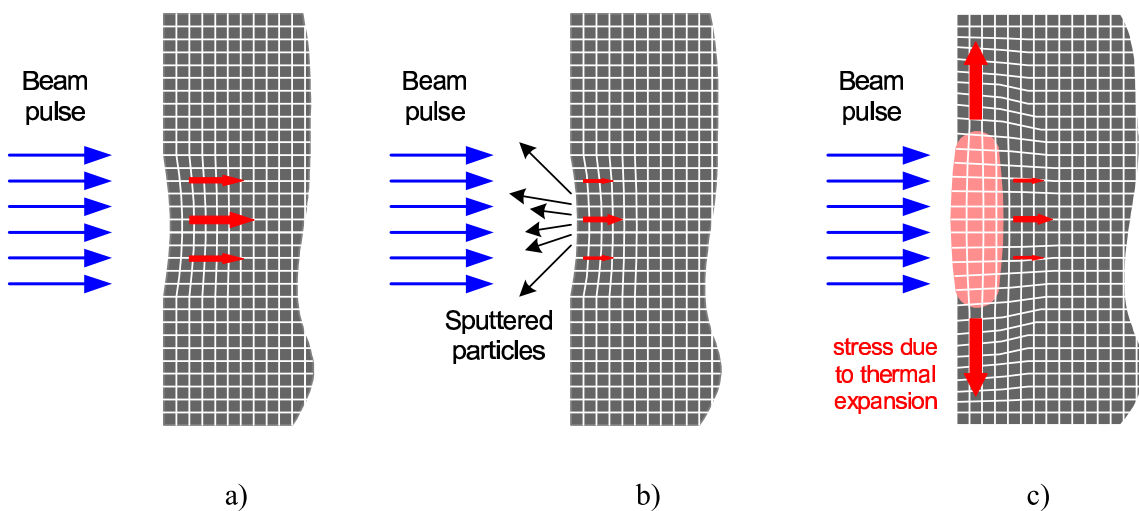a)   b)   c)

Fig. 3.1. The main mechanisms of generation of an elastic wave by a pulsed ion beam in a solid target: a) momentum transfer from the beam; b) momentum transfer from the sputtered particles; c) deformation of the sample due to a transient heating.

$$\vec{f}(\vec{r},t) = -3B\alpha\vec{\nabla}T(\vec{r},t) \tag{3.14}$$

The stress tensor has additional term corresponding to the thermal stress:

$$\sigma_{ij} = \lambda\delta_{ij}\sum_k u_{kk} + 2\mu u_{ij} - \alpha(3\lambda+2\mu)(T-T_0)\delta_{ij} \tag{3.15}$$

The heating process in the material can be described by the thermal diffusion equation, which is written as

$$-\kappa\Delta T + \rho C_p \frac{\partial T}{\partial t} = Q(\vec{r},t) , \tag{3.16}$$

where C_p is specific heat at constant pressure, κ is the heat conductance of the material and $Q(\vec{r},t)$ is the heat power density. One can solve this equation using the FEM, the BEM and the method of finite differences as well as by integration using Green's function. The Green's function for this equation is

$$G(\vec{r},\vec{r}',t,t') = \begin{cases} 0, & t \le t' \\ \dfrac{1}{\sqrt{4\pi D(t-t')}^3}\exp\left(-\dfrac{(\vec{r}-\vec{r}')^2}{4\pi(t-t')D}\right), & t > t' \end{cases} \tag{3.17}$$

where D is the diffusivity defined as:

$$D = \frac{\kappa}{C_p\rho} \tag{3.18}$$

If the surface temperature is very high it is necessary to take in to account also thermal radiation from the surface which is proportional to T^4, according to the Stefan-Boltzmann's law. The excitation of an elastic disturbance in a solid can be provided by local transient heating using microwaves, pulsed laser beam and pulsed electron or ion beams.

3.2.3. Local target modification

The process of heating of a target region can lead to changing of properties of the sample, like melting and crystallization of amorphous material or phase transitions. Laser or electron beams need enough intensity in order to melt the irradiated volume. An ion beam can provide amorphisation of the irradiated volume even without strong heating. All these effects influence the mechanical properties of the target surface, first of all they change the density of the material. This is also one of the reasons of elastic waves generation. The

intensity of this effect is strongly connected with material properties and the beam parameters.

3.2.4. Other mechanisms

Besides the effects described above there are also other possible reasons of transient elastic deformation of a sample under ion, electron or laser beam irradiation, but the contribution of these mechanisms in the final acoustic wave are usually quite small, however in certain conditions they can have a crucial influence.

For instance, an electrically insulating sample is locally charged up by the beam of charged particles. The fast charging process causes a local deformation because of Coulomb force and gives rise to an elastic wave. At a certain critical amount of charge value the sample discharges with a breakthrough which creates a shock wave.

Also in a piezoelectric or electrostrictive material electrical charging takes place like in insulating samples. The piezoelectric effect leads to an enhanced local deformation which may be much stronger than in the case of a normal insulator.

Formation and propagation of cracks in crystalline materials initiated by an ion pulse also can be a source of acoustic waves. Chemical or even nuclear reactions induced by incident ions in the target can also lead to local heating and as a result to thermal elastic waves.

3.3. Thermal elastic waves generated by a pulsed ion beam
3.3.1. Thermal effect

The pulsed irradiation leads to a fast rise of the temperature near the surface of the sample in a small volume, where the energy dissipates, with following heat diffusion in the sample and thermal radiation from the surface and cooling down to reference temperature. The calculated temperature as a function of depth and radial distribution in iron are shown in Fig. 3.2a and Fig. 3.2b. The heated volume in the target is taken according to the typical ion beam parameters used in the experimental work (see chapter 4), with a spot diameter of 2 mm and mean ion range R_P of about 1.8 μm, corresponding to 5 MeV oxygen ions in iron. The radial distribution of the power density shows a Gaussian shape, similar to the ion beam profile. Because of the relatively large diameter of the heated area and the short
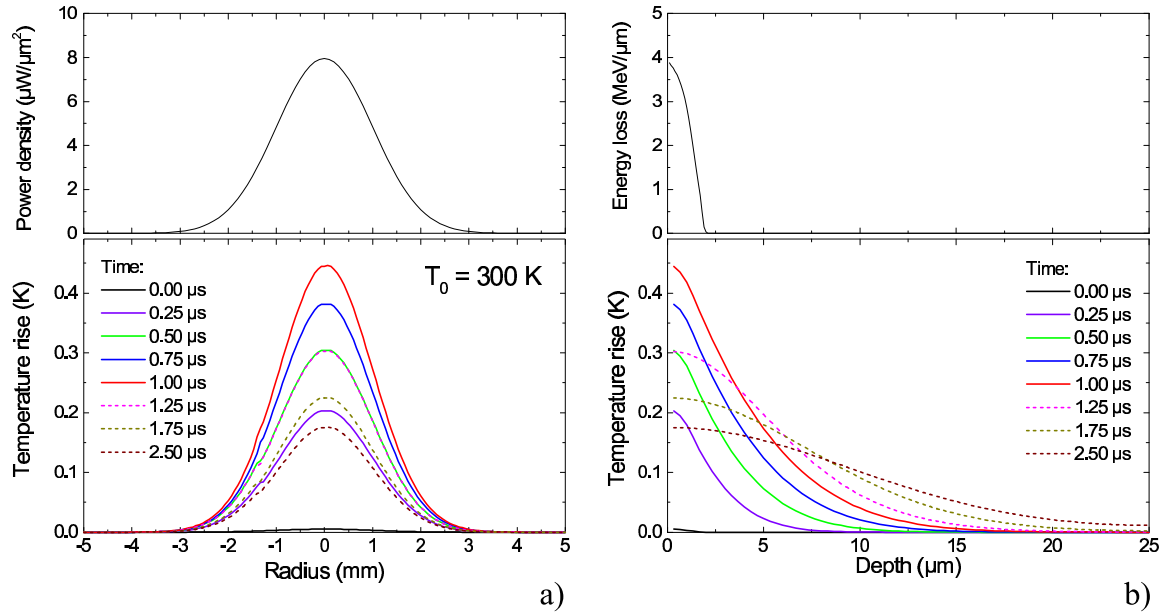
Fig. 3.2. Calculated temperature distribution in an iron sample induced by a 1 μs long heating ion pulse: a) radial distribution, b) dependence on depth with the corresponding power density distribution and energy loss. All distributions are calculated for an O^+ ion beam with a pulse power of 50 W at energy of 5 MeV. The maximum is reached at the end of the pulse (1 μs).

time scale, a change of the shape of the radial temperature distribution in the solid is negligible except the decrease of the amplitude. This occurs due to heating of a thin subsurface layer with a thickness comparable to the depth of the heat diffusion, corresponding to the ion beam pulse duration. Fig. 3.3a demonstrates the time dependence of the temperature after the initial heating at these conditions. In case of a periodically modulated heating the temperature rise has also a periodic behavior, as it is shown in Fig.3.3b, so a periodic thermal wave propagates in the medium. This leads to either the generation of a single pulse or a periodic elastic wave in the target, respectively. For a better understanding it is useful to apply the concept of thermal waves [6]. A solution of equation (3.16) can be written as a periodic function in time:

$$T(\vec{r},t) = T_0(\vec{r}) \cdot \exp(i\omega t) \qquad (3.19)$$

with the angular frequency ω. Substituting the solution into Eq. (3.16) one obtains:

$$-\kappa \Delta T + \rho C_p \cdot i\omega T = Q(\vec{r},t) \qquad (3.20)$$

For the one-dimensional case the dependence of the temperature on the depth z has an exponential behavior:

$$T(z,t) = T_0 \cdot \exp(kz) \cdot \exp(i\omega t) \qquad (3.21)$$

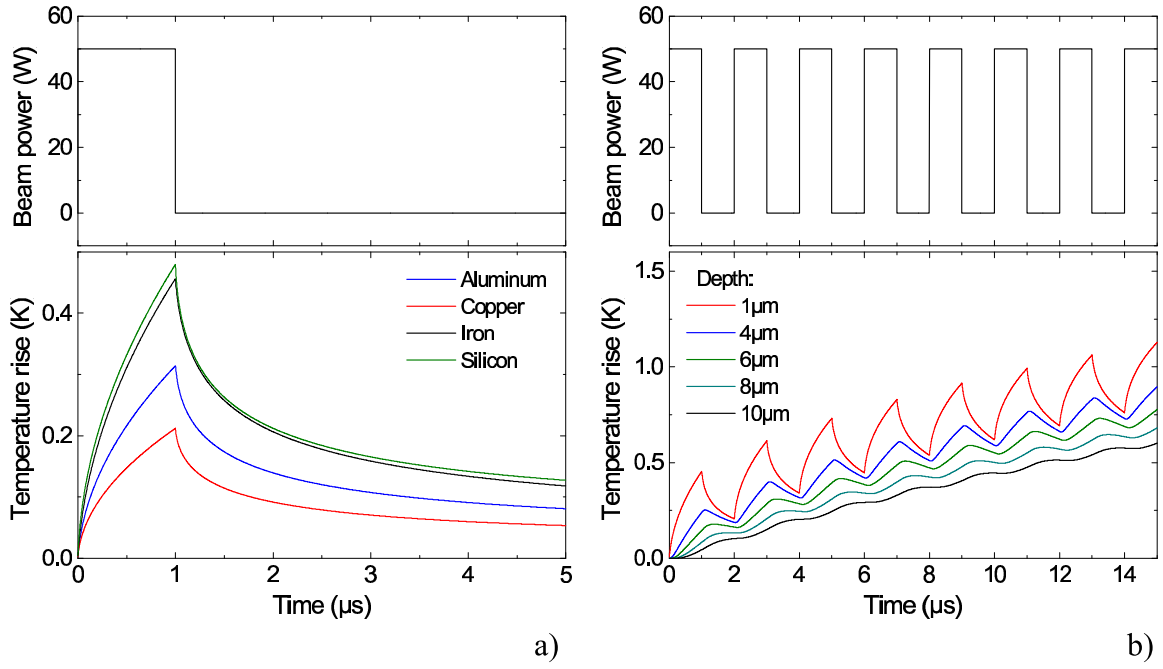where the coefficient k is defined as

Fig. 3.3. Temperature of a target surface as a function of time: a) induced by a single heating pulse of 5 MeV O^+ ion beam in different materials, b) periodical heating in iron sample, and corresponding power of the pulse of 50 W.

$$k = \pm\sqrt{\frac{i\omega C_p \rho}{\kappa}} = \pm(1+i)\sqrt{\frac{\omega C_p \rho}{2\kappa}} = \pm(1+i)d_{th} \qquad (3.22)$$

The solution is a highly damped wave with a decay length constant

$$d_{th} = \sqrt{\frac{2\kappa}{\rho C_p \omega}}, \qquad (3.23)$$

which is called thermal diffusion length. This parameter represents the characteristic depth where the oscillations of the temperature can be observed. It plays the similar role as the skin depth in the case of electromagnetic waves in metals. This is an important parameter which defines the lateral resolution of an acoustic microscope using thermal elastic waves.

The heat power is defined by the dissipation of the energy of the ions in the material. As it was mentioned above, the process of the ion energy dissipation in a solid depends on the ion mass and energy as well as on the properties of the target material. The values of total energy loss dE/dx, calculated for oxygen ions in an iron target as a function of depth are shown in Fig. 3.4. The projected ranges R_p of different ions are functions of their mass and energy, so the heated volume is also different. The temperature distributions calculated for 1, 4, 7 and 10 MeV oxygen ions in iron are shown in Fig. 3.5a. One can see that all four curves have the same shape and only the amplitudes differ. The calculations were done for 1 µs-pulse with current of 10 µA. Fig. 3.5b shows the corresponding maximum temperature
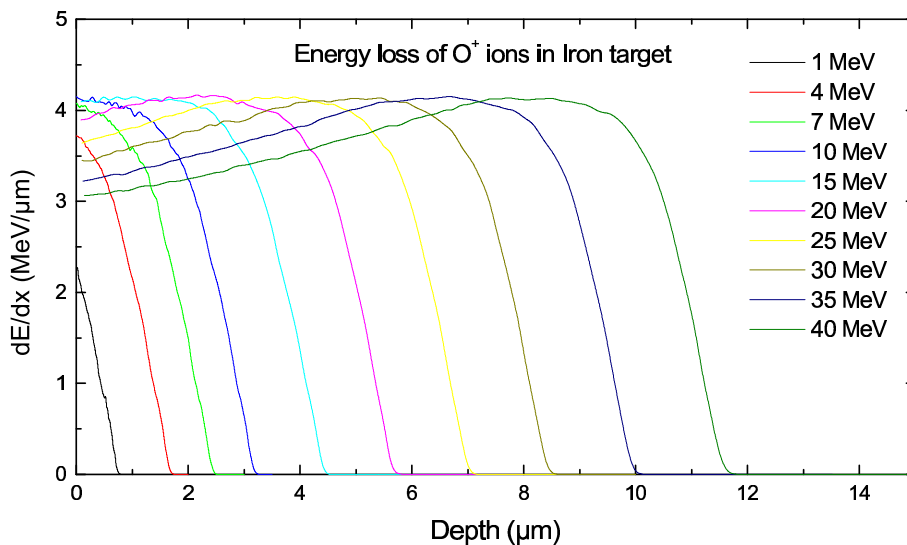
Fig. 3.4. Total energy loss of oxygen ions in an iron sample as a function of depth calculated for energies from 1 to 40 MeV using SRIM 2000 code.

as a function of the energy. This dependence demonstrates a linear behavior in the energy range from 1 to 10 MeV. The main reason for this is the quite high thermal conductivity leading to the fast thermal diffusion in the given time scale, which corresponds to a time immediately after the 1 μs long beam pulse. For a material with a low thermal conductivity the temperature dependence on the energy appears close to a linear function at energies lower than 2 MeV, but at increasing energy this behavior becomes nonlinear with the tendency to a saturation (Fig. 3.6 and 3.7). A higher thermal conductivity coefficient leads

Fig. 3.5. The temperature in a sample along the beam axis as a function of depth calculated for irradiation of an iron sample by a 1 μs pulse of O^+ ion beam with the current of 10 μA (a) and corresponding dependence of the maximum temperature on the ion energy (b).

Fig. 3.6. The maximum temperature rise as a function of ion energy for different coefficients of the thermal conductivity κ (W/m·K) calculated for the specific heat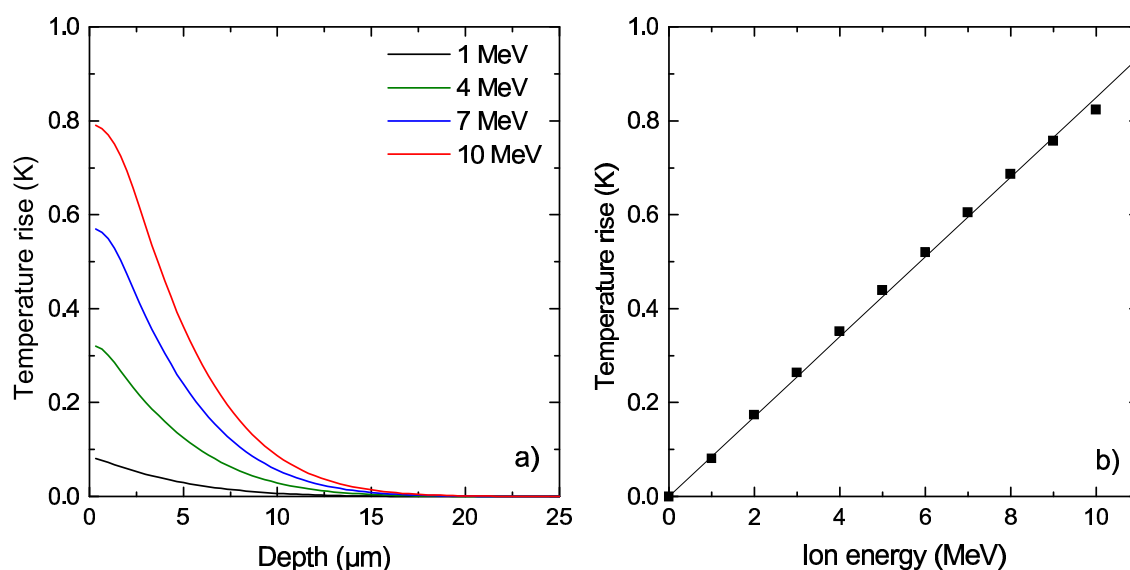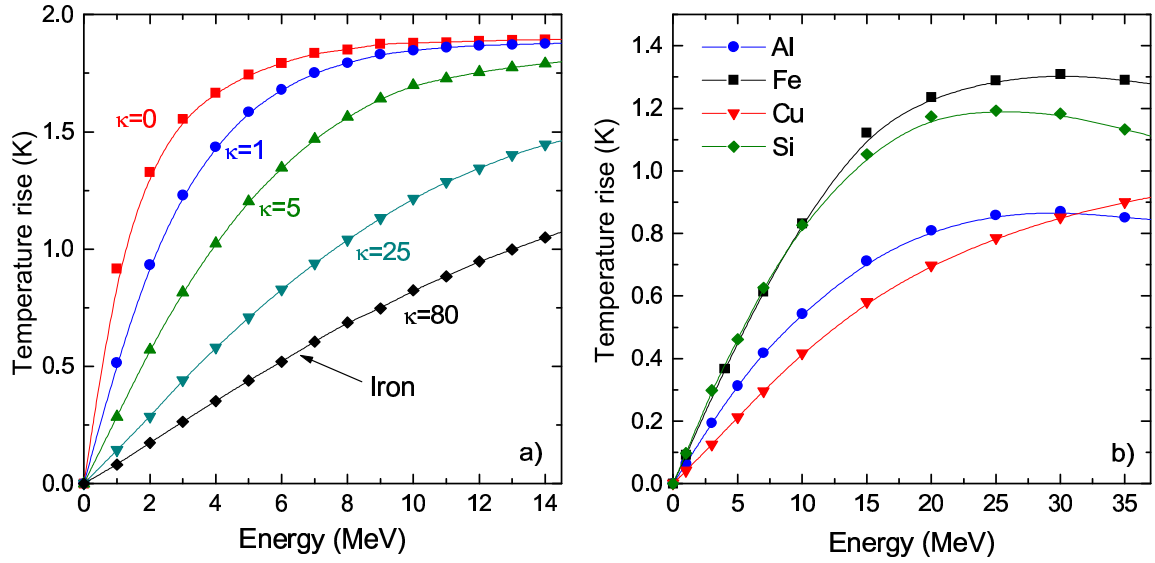 and density of iron (a) and for different materials, namely aluminum, iron, copper and silicon (b). The points were calculated for a 1 μs long pulse.

to more linear curves and lower temperatures. At higher energies all these curves come to saturation at the certain temperature value (Fig. 3.6), but with increasing time they become more linear due to thermal diffusion. A simple criterion of linearity can be written using the diffusivity D (Eq. (3.18)) as:

$$\sqrt{D \cdot t} > R_P, \qquad (3.24)$$

where t is a characteristic time of observation after the heating. The left side of this expression corresponds to the diffusion length after the time t. The thermal conductivity of the solid plays an important role in the heating process and reduces the influence of the ion range R_p. In the case of large time scale the diffusion occurs of larger distance than the ion range and the depth of the heated volume. So in spite of the different projected ranges for different energies the shape of the temperature distribution is nearly the same and the maximum of the temperature is proportional to the energy in the range up to 10 MeV for the 1 μs long ion beam pulses.

Table 3.2 Thermal properties of materials

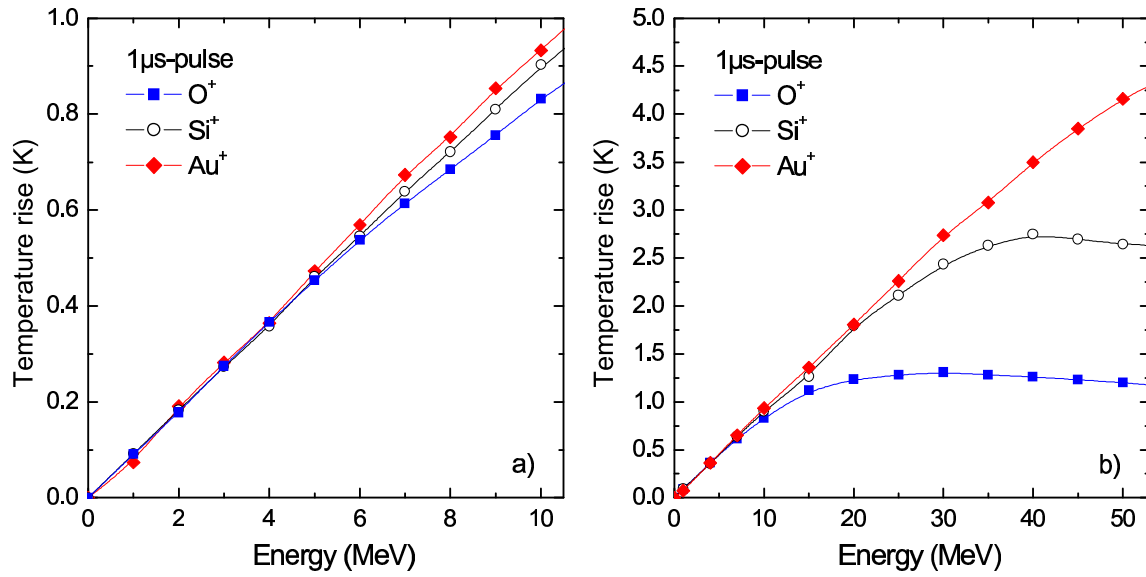| Material	C_p (J/kg· K)	κ (W/m· K)	α (10^{-6} 1/K)	D (10^{-6} m^2/s)
Aluminum	897	237	23.1	98
Iron	450	80	11.85	22.5
Copper	385	401	16.5	116
Silicon(amorph.)	705	145	2.8	90

Fig. 3.7. Dependence of the heating on the ion energy calculated for different ions: O^+, Si^+ and Au^+ in the energy ranges of 0-10 MeV (a) and 0-50 MeV (b).

In Fig. 3.6b the values of temperature rise, calculated for aluminum, copper, iron and silicon are shown. Copper has the highest thermal conductivity and density and low specific heat, therefore the temperature rise is lowest in the graph. As a light material with relatively low thermal conductivity and high specific heat, silicon reaches higher temperatures by the same heating power. The thermal parameters of the used materials are summarized in Table 3.2.

The penetration depth and energy loss in a target depends also on the mass of the used ion. A heavier ion is stopped in the target close to the surface and loses energy faster, a light ion can penetrate deeper and heats a larger volume in the sample. The calculated maximum values of the temperature in an iron sample for oxygen, silicon and gold ions are presented in Fig. 3.7. In spite of the mass difference of the ions the values are nearly similar at energies lower than 10 MeV (Fig. 3.7a). The ion ranges of the low energy ions are relatively small. Due to thermal diffusion the thickness of the heated volume on the target surface is larger than the ion ranges and is nearly the same for all ions. It is defined by the thermal diffusion length in the material, $\sqrt{D \cdot t}$, for the taken time scale (some µs). So the heat density and temperature rise do not depend on the ion mass. A further increase of the energy leads to saturation, the temperature providing by heating with lighter ions tends to saturation at lower energies, as it is to be seen in Fig. 3.7b. The high energy ions penetrate deeper in the target and heat thicker layer of material. The heat cannot diffuse in this depth during this time so the main parameter defining the temperature rise is the ion

range which depends on the ion mass. A light ion has larger ion range and heats bigger volume than a heavy ion and therefore the temperature rise is smaller.

3.3.2. Elastic waves induced by local transient heating

Several publications on the theory of the thermal elastic wave generation by pulsed laser beams have been reported [1, 3-5]. If the power densities are insufficient to cause melting, the origin of the thermal acoustic emission by a pulse of ions is similar as for a laser beam. Therefore the parameters of the generated elastic wave should be comparable. The thermal expansion of a small volume which is heated by the penetrating ions leads to local stress in the sample. A pulsed ion beam provides a pulse of mechanical stress which gives rise to an elastic wave in the material. The density of the developed force is proportional to the gradient of the temperature as it is defined by Eq. (3.14) and the components of the stress tensor are proportional to the local temperature rise (Eq. (3.15)). Relaxation of the thermal stress leads to the strain which can be written as:

$$u_{ij} = \alpha \cdot (T - T_0) \cdot \delta_{ij} \qquad (3.25)$$

This expression and the Eq. (3.15) show that the thermal stress amplitude and displacement are expected to be proportional to the incident ion energy, to the ion beam current and to
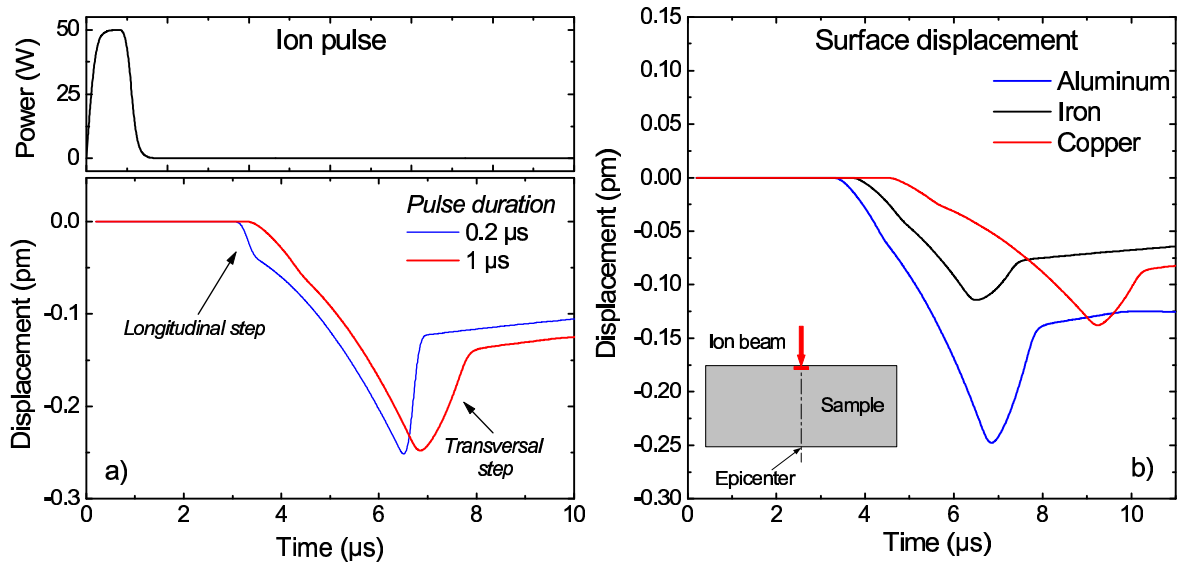

Fig. 3.8. Calculated normal surface displacements at epicenter of an iron sample with an ion pulse duration of 200 ns and 1 μs and equal energies per pulse of 50 μJ (a) and the surface displacements on aluminum, iron and copper (b) for a 1 μs long 5 MeV O$^+$ ion beam pulse with a current of 10 μA.

the pulse duration at the time scale where temperature is proportional to the ion energy. In this work the bulk waves propagating through a thick sample and the detection on the opposite side (epicenter) are of special interest.

The vector field of the elastic displacements in a solid can be numerically calculated using Eq. (3.4). The calculation scheme is explained in Appendix B and more in details in [49]. The predicted surface displacement as a function of time at the epicenter, i.e. at the point opposite to the point of generation, is shown in Fig. 3.8a. The two curves represent a surface motion, calculated for a 20 mm thick aluminum plate and a 50 µJ ion pulse with duration of 200 ns and 1 µs, respectively. The curves are close to the one reported by Doyle [4], Rose [3], Hutchins [5], Dewhurst [9], Scruby [12], McDonald [16] and Sinclair [50]. The lateral size of the plate was taken to be much larger then the thickness in order to avoid influence of the side surfaces. The longitudinal wave is predicted as a step like depression of the surface with the following low-frequency motion. This step is better pronounced by a shorter ion pulse as it is seen in Fig. 3.8a for the 200 ns pulse. The curve obtained for a 1 µs pulse is more smooth and here the longitudinal step is nearly invisible. The transversal component is a large step like elevation of the surface arriving later then the longitudinal one. Rose [3] has shown that the ratio of the transversal to the longitudinal step displacement amplitudes depends on the Poisson ratio of the material, v:

$$\frac{A_T}{A_L} = -\frac{2(1-v)}{1-2v} = \left(\frac{c_L}{c_T}\right)^2 \tag{3.26}$$

For aluminum with $v = 0.34$ one finds a ratio of 4.13, for copper and iron the ratios are 4.32 and 3.43, respectively. The ratio of the longitudinal arrival time to the transversal one is defined by the ratio of their velocities and is close to 1:2. The curves for all three materials calculated for the same thickness are shown in Fig. 3.8b. The main differences are in the amplitudes of the displacements and the arrival time which depends on the properties of the materials. Excellent agreement between theory and experimental data obtained using a laser beam was observed [3-5, 9, 12, 50].

3.4.   Summary

The expected important mechanisms of the ion acoustic effect are momentum transfer and transient local heating of the target. The momentum transfer provides the elastic wave with the amplitude proportional to the square root of the incident ion energy. The expected

temperature rise and the amplitude of the thermal elastic waves should linearly increase with ion energy at least up to 10 MeV for a microsecond time scale. By the dominance of one of these factors in the measured energy dependence one can decide which of these mechanisms gives the main contribution.

4. Experimental investigation of the ion acoustic effect

For the investigation of the ion-acoustic effect in a solid sample it is necessary to apply a powerful pulsed ion beam providing enough energy per pulse to generate a detectable acoustic signal in the target. For this purpose the 3MeV-Tandetron accelerator [51, 52] was chosen. Acoustic waveforms in different materials were measured using different ion species and charge states, namely Si^{2+}, Si^{3+}, O^+, O^{2+}, O^{3+}, O^{4+}, Au^{2+}, Au^{3+}, Au^{4+} with an energy in the range from 1.5 to 10 MeV. The ion beam current was between 2 and 40 μA depending on the ion species, charge state and adjustment of the ion source and the accelerator. In order to reach a good time resolution for the measurements of the acoustic waveforms, the pulse duration must be as short as possible on the one hand and long enough in order to have sufficient energy per pulse on the other hand. The accelerator itself is not equipped with a fast beam blanking system. Therefore a high voltage pulser was designed to provide a short high-voltage pulse with variable duration in the range from 0.5 to 5 μs. The voltage was applied to two flat electrodes of the electrostatic corrector located between the accelerator and the low-energy injector magnet. Investigation of acoustic waves was carried out using polycrystalline metallic samples (aluminum, iron and copper) and a monocrystalline silicon sample. Acoustic waveforms transmitted through the sample were detected on the back surface. The dependence of the surface displacement on ion energy, charge state, flux and the ion beam spot size were obtained as well as the acoustic waveform at different distances from the epicenter (center of the back side) of the target.

A set of experiments with a low-energy focused ion beam (FIB) was carried out using the IMSA-100 FIB [14,53,54]. The focused ion beam operates in the energy range 30-50 keV (for single charged ions) with a maximum beam current of about 3-5 nA. Si^{2+}, Ge^{2+}, Ga^+ and Au^+ ions were used for the measurements. Due to the FIB power of about 100 μW the estimated amplitude of the surface vibration is lower than 10^{-15} m at a beam modulation frequency of 10 kHz. The only possibility to register the signal was to operate with a FIB modulation at the resonance frequency of a high-quality piezoelectric sensor, followed by

signal processing using the lock-in technique. In this manner the dependence of the amplitude of the elastic waves on the ion flux and the FIB spot size was obtained. The same measuring equipment and this FIB system are used to demonstrate the application of the ion-acoustic effect in an acoustic microscope [55, 56]. The experimental work with the FIB system is described more in detail in chapter 5.

4.1   Experimental equipment - high energy ion beam facilities at the Research Center Rossendorf

4.1.1 3-MeV Tandetron accelerator

Experiments with high energy ion beams were carried out at the Rossendorf 3MeV-Tandetron accelerator. This equipment was built by High Voltage Engineering Europe (HVEE) and put into operation in 1993 [51,52]. The scheme of the accelerator is shown in Fig. 4.1. The accelerator is equipped with two ion sources for the production of nearly all ions of the periodic table of elements. One injector is accommodated with a duoplasmatron source Model 358 from HVEE which is used mainly for the emission of He ions and other noble gas ions. It operates with a charge exchange channel filled with lithium vapor for recharging of the initially positive ions emitted from the plasma through the 0.3 mm aperture in the anode electrode of the source into negative ions. They are further separated and turned by the low energy magnet and injected in to the Tandetron for the following acceleration. The other injector is accommodated with a heavy ion sputter source Model
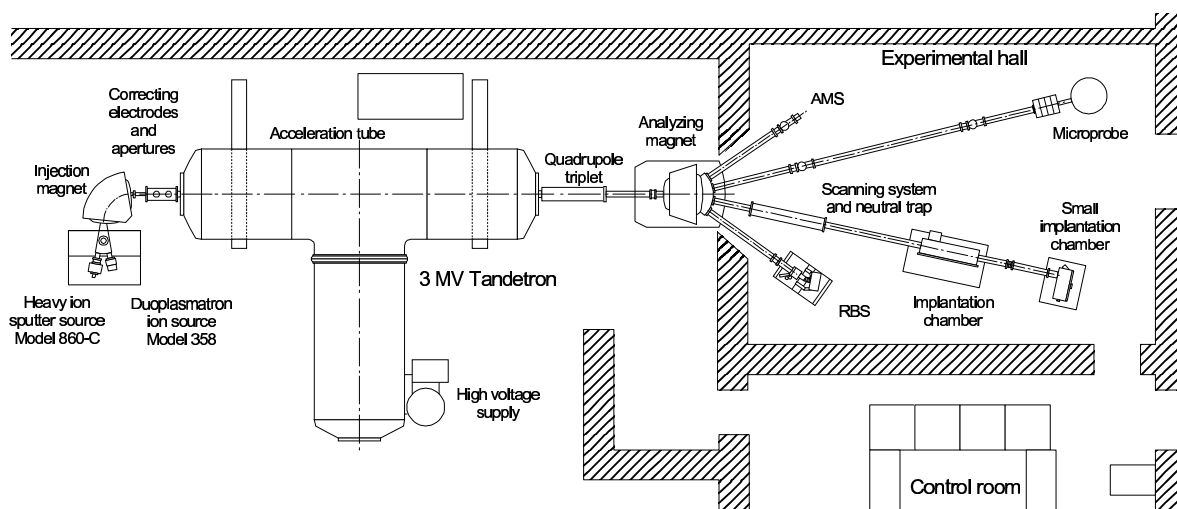

Fig. 4.1. 3MeV-Tandetron at Research Center Rossendorf.

860-C from HVEE. A low pressure cesium vapor is admitted to the source and ionized on the spherical ionizer surface which is held at approximately 1100°C. The positive Cs ions are accelerated towards the target from which atoms are sputtered. The negative ions are accelerated by the same target-ionizer potential of about 25 keV. The source is capable to produce nearly all ions with negative charge. Typical ion beam currents which are measured between the low energy injector magnet and the accelerator are given in Table

Table 4.1 *List of ions produced HVEE 3MV Tandetron*

Isotope	Emitted ion	Ion current (μA)	Source material
^{1}H	H$^-$	10-40	TiH$_2$
^{2}H	D$^-$	20-40	TiD$_2$
^{4}He	He$^+$	2-4.0	He-gas
^{7}Li	Li$^-$	1.7-2.4	LiO$_2$+W
^{11}B	B$^-$	2.0-4.0	B+W
^{12}C	C$^-$	40-80	Graphite
^{14}N	(CN)$^-$	1-15	BN+C
^{15}N	(CN)$^-$	2-2.5	Na^{15}N$_3$+C
^{16}O	O$^-$	40-140	Fe$_2$O$_3$
^{19}F	F$^-$	20-35	LiF+W
^{27}Al	Al$^-$	0.6-2.0	Al
^{28}Si	Si$^-$	50-130	Si-monocrystall
^{31}P	P$^-$	10-45	GaP
^{35}Cl	Cl$^-$	8-33	CsCl+W
^{39}K	K$^-$	0.2	KHCO$_3$+Ag
^{48}Ti	Ti$^-$	5-10	TiH$_2$
^{52}Cr	(CrH)$^-$	2-8	Cr+TiH$_2$
^{58}Fe	Fe$^-$	2-4	Fe$_2$O$_3$
^{58}Ni	Ni$^-$	20-35	pure Ni
^{63}Cu	Cu$^-$	5-25	Cu
^{64}Zn	(ZnO)$^-$	0.5-1.0	ZnO+W
^{74}Ge	Ge$^-$	5-13	Ge
^{75}As	As$^-$	9-20	GaAs
^{80}Se	Se$^-$	5-20	CdSe
^{79}Br, ^{81}Br	Br$^-$	10-30	CsBr+W
^{93}Nb	(NbC)$^-$	1.2-1.5	Nb+C
^{105}Pd, ^{106}Pd	Pd$^-$	0.6-0.9	Pure Pd
^{107}Ag	Ag$^-$	4-6	Pure Ag
^{112}Cd, ^{113}Cd, ^{114}Cd	Cd$^-$	0.1-0.2	Cd+W
^{115}In	In$^-$	0.3-0.5	InO$_2$+W
^{120}Sn	Sn$^-$	2.0-7.0	Sn, Sn+W
^{121}Sb, ^{123}Sb	Sb$^-$	0.8-1.4	Sb+Pb
^{127}I	I$^-$	20-50	CsI+W
^{166}Er, ^{167}Er, ^{168}Er	(ErO)$^-$	0.9	ErO+W
^{195}Pt, ^{196}Pt	Pt$^-$	25-30	Pt
^{197}Au	Au$^-$	60-75	Au

4.1. These values refer to the current of low energy negative ions. An immersion lens (Q-snout) allows low injection voltage and increases the injection energy from about 25 keV to the terminal high voltage and focuses the ion beam into the stripper channel. The stripper gas (N_2) is circulated by a turbomolecular pump installed inside the terminal with typical pressure of about $2 \cdot 10^{-6}$ mbar which allows to have a recharging efficiency of 80 - 100%. The terminal voltage is generated by a capacitive coupled cascade, measured and stabilized by a generating voltmeter and insulated by SF_6 gas with a pressure of about 8 bars. After acceleration the ion beam is focused by a triplet of electrostatic quadrupole lenses. The final heavy ion beam consists of mostly 2+ and 3+ charged ions which have a current contribution of about 30-40 % of the total current each. Ions with a specific charge state are separated by the analyzing magnet. Behind the analyzing magnet a Rutherford Back Scattering (RBS) chamber, an implantation beam line and a nuclear microprobe are installed. In the implantation beam line the ions pass through the x-y-scanning system. The scanning area is sufficient to allow implantation in wafers up to 5" and 4" in diameter inside of big and small implantation chambers, respectively. In the current work the scanning system was deactivated, only the offset was used for changing the position of a pulsed beam hitting a certain point of the target surface. Oxygen, silicon and gold ions were chosen for these experiments because of the high available ion current (Table 4.1). The sample with the attached sensor, a moveable Faraday cup and preamplifiers were installed inside of the small implantation chamber with base pressure in the range of 10^{-6} mbar.

4.1.2 Ion beam switch and measurement of the pulse current

4.1.2.1 Ion beam switch

For the experiments it was necessary to form relatively short pulses of the ion beam. Since the accelerator itself is not equipped with a blanking system providing microsecond-long pulses of the ion beam, a high voltage (HV) pulse generator was designed and built for switching of the MeV-ion beam. This device is based on a powerful radio-frequency tetrode tube RS685 from AEG which can operate as a switch for a voltage as high as 3 kV. The initial rectangular-shape negative signal with amplitude of 10 V is provided by a pulse generator PM5771 from Philips. This generator has a switching time of about 20 ns. The signal is amplified by the first cascade of the device up to 200 V and applied to the grid of
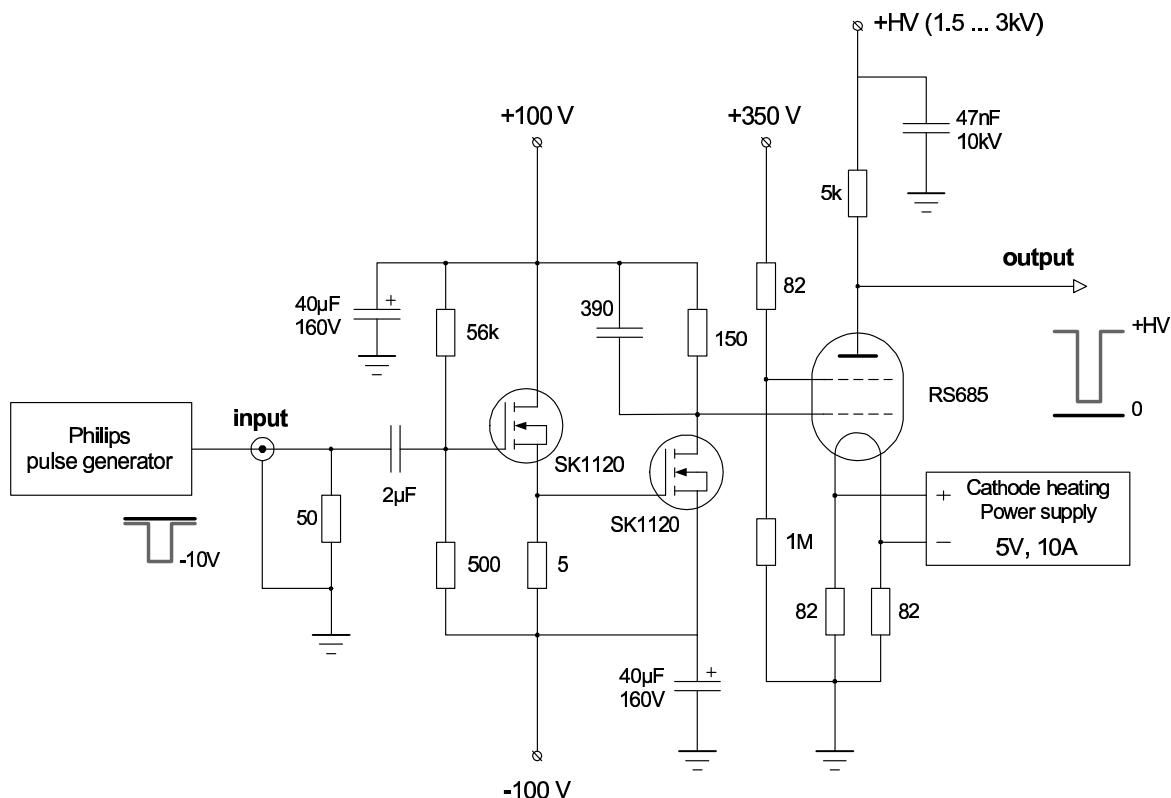
Fig. 4.2. Electrical scheme of the high voltage switch.

the tetrode tube. The anode of this tube is kept under constant high voltage. In Fig. 4.2. the principle scheme of the beam switch is given. The pulsed high voltage is applied on two electrode plates of the ion beam corrector which are placed just after the source module and injection magnet. So they are used as the blanking electrodes. The plates are about 10 cm long with a distance of about 5 cm. The ion energy at this place is 20 - 25 keV which allows to chop the beam before acceleration with a blanker voltage of 1200 - 1500 V. The dependence of the transmission function of the blanker on the applied voltage is shown in Fig. 4.3a. The high voltage from the switch is applied to the top plate, the bottom plate kept under permanent potential nearly equal to the low level voltage of the switcher, i. e. of about 100-200 V, so the beam moves aside and cannot pass the 10×12 mm rectangular aperture of the Tandetron entrance. The reason of applying a positive potential on the other electrode is that the low level voltage on the output of the switch cannot be at ground potential due to the high resistance between cathode and anode of the electronic tube even if it is completely open. During a short time the beam blanker switches the voltage on the top plate from high level to low level, equal to that on the bottom plate and back, so only a short pulse of the ion beam passes through the aperture. Duration of the initial signal coming from the pulse generator defines the duration of the HV pulse on the output of the
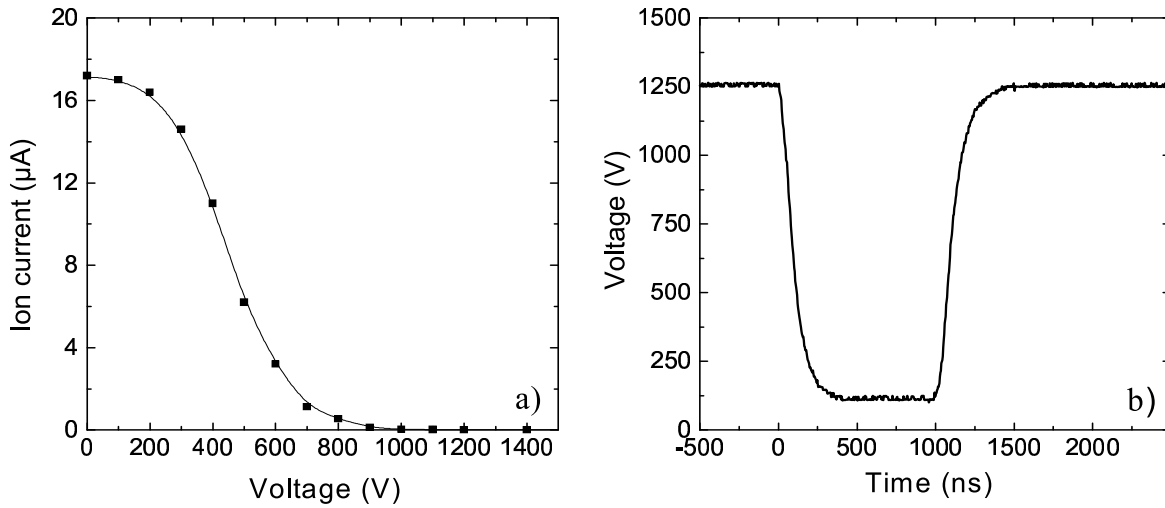
Fig. 4.3. The Si⁻ ion injection current, measured in the entrance of the Tandetron accelerator as a function of the voltage applied on the corrector electrodes (a) and a 1μs-pulse of voltage on the output of the beam switch (b).

switcher. The initial signal is amplified by the cascade based on the two high voltage MOS FET transistors SK1120. This cascade transforms the input signal switching from 0 to −10 V into the pulsed voltage from −100 V to +100 V with a slope of 80-100 ns. This signal finally drives the grid of the tetrode acting as switch of the high voltage. The voltage slew rate providing by this device is nearly 5000 V/μs which corresponds to the switching time from the high voltage level (1250 V) to the low level (100 V) of about 200-250 ns. The maximum anode current for this type of tetrode is nearly 1 A corresponding to the
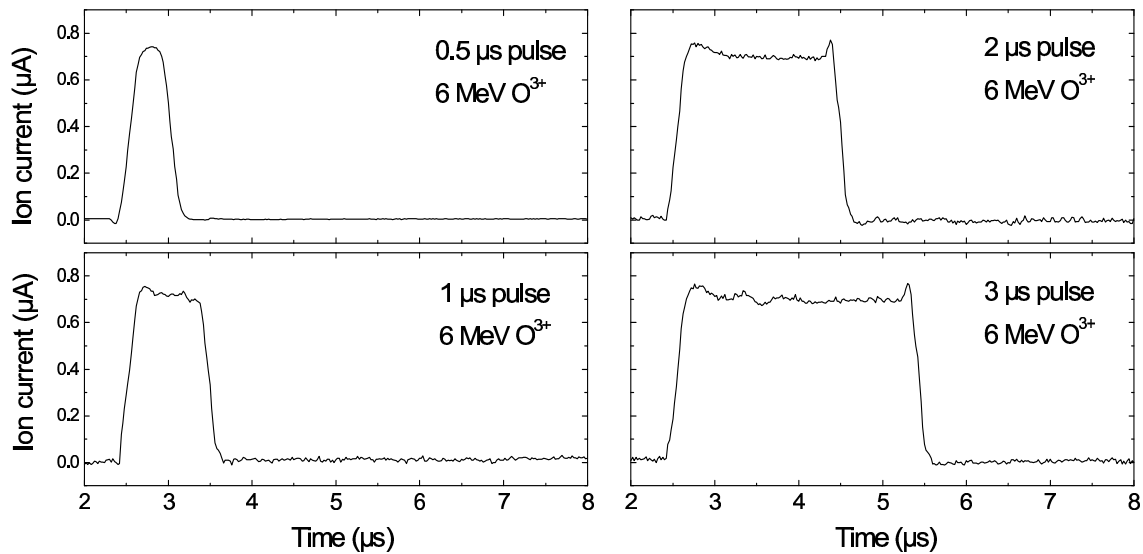

Fig. 4.4. Example of ion beam pulses: 0.5 μs, 1 μs, 2 μs and 3 μs long pulses of a 6 MeV O³⁺ ion beam.

minimum resistance of about some kΩ. The capacitance of the blanker plates and the connecting cables is of the order of 50 pF. Taking into account the internal resistance of the tetrode tube and the small value of capacitance results in a time constant of 250 ns (Fig. 4.3b). In order to decrease the influence of the capacitance, cables without coaxial screening, only with HV insulation were taken. The obtained minimum ion beam pulse duration was about 500 ns. In Fig. 4.4 typical shapes of an O^{3+} ion beam pulse are given. The needed repetition rate of the pulses is less than 100 Hz in order to have no mixing of the acoustic signals generated in the sample by subsequent pulses. This leads to a mean power consumption of the tube of not more than 0.3 W at the voltage of 3 kV and a pulse length of 1 μs. The used HV power supply can provide only 20 mA and therefore a capacitor was used additionally as a charge storage in order to keep the constant voltage. The value of the capacitor of 47 nF gives a time constant of about 200 μs which is much longer than the longest used pulse. After acceleration the ion beam is focused on the target plane by a triplet of quadrupole lenses.

4.1.2.2 Ion beam current and profile measurements

For measurement of the AC current of the ion beam and controlling the shape of the pulses
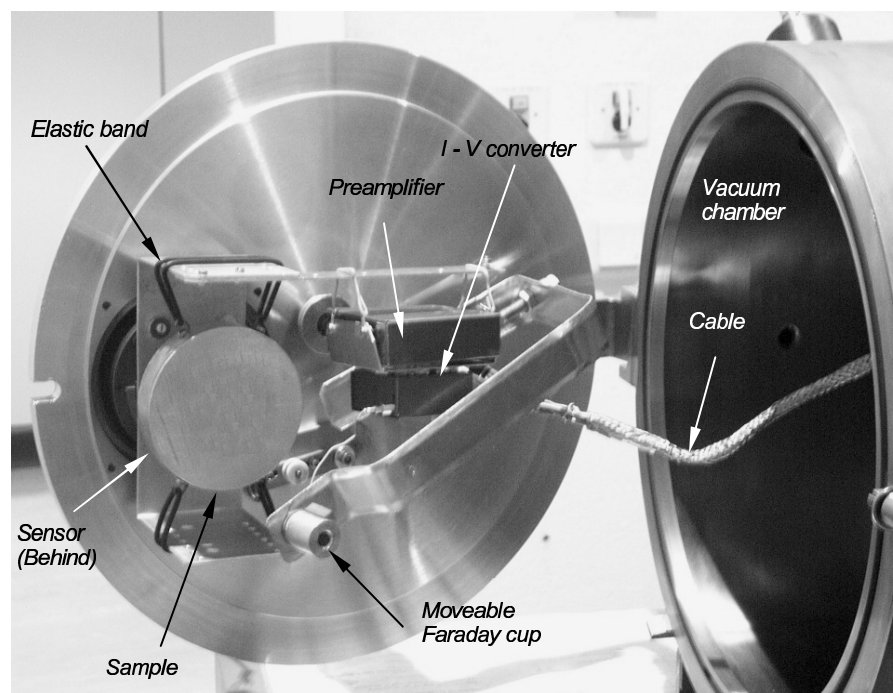

Fig. 4.5. The vacuum chamber with installed experimental set-up: aluminum sample hanging on ribbon bands, preamplifier, current-to-voltage converter and movable Faraday cup.

a movable Faraday cup with a high frequency current-to-voltage (I-V) converter is employed. From the measured current the power and the total energy as well as the ion flux in each pulse can be deduced. In the simplest case the cup can be made as a flat piece of metal introduced in the ion path. The value measured by such a cup has to be corrected because many charged secondary particles escape from the cup. To prevent this effect the cup can be formed as a cylindrical box with a small hole in the center of the front side. So the ejected secondary particles hit the side cylindrical wall and stay inside the cup. In order to suppress all secondary electrons and to obtain a good accuracy of the measurements, an additional strong magnet around the cup and a positive potential offset at the entrance of the Faraday cup can be applied. The cup used in this work for precise current measurements was a 25 mm long hollow cylinder made from aluminum with an attached CoSm magnet on one side in order to catch the secondary electrons. Additionally a negative voltage of about 60-100 V was applied between the bottom of the cup and the outer housing. The diameter of the opening entrance is 10 mm. This Faraday cup is fixed on a holder which can move it into the ion beam. The holder is driven using a vacuum feedthrough on the wall of the implantation chamber (Fig. 4.5). For amplifying a short current signal coming from the cup a high frequency I-V converter is applied. It is based on a NE5539 high frequency operational amplifier and a FET transistor in the input with 100 Ω resistor shunting its gate. The voltage amplification of this device is about 400 corresponding to I-V converting factor of about 40 mV/μA. The converter operates in the frequency band from 500 Hz to 15 MHz with the slew rate of the signal of about 25 V/μs. To reduce parasitic influences the converter is placed in a metallic housing in the vacuum chamber close to the Faraday cup.

The accelerator is equipped with a beam profile measuring device which is located near the entrance of the implantation chamber. This system consists of two crossed wires moving in horizontal and vertical directions, respectively. The current collected from these wires during the movement through the beam and their coordinates give an information about the cross section profile of the beam. This device can also be used for determination of the ion beam diameter, needed for evaluation of the signal amplitude as a function of the beam intensity. The profile of a well adjusted and focused ion beam has nearly a Gaussian shape. For estimation of the beam diameter the full width at half maximum (FWHM) of the profile was taken. In the most cases about 2 mm could be achieved.

4.2 Detection of small surface vibrations

The displacement of a surface element can be described by a 3-dimensional vector. In this work only one component of the displacement, normal to the surface was measured. This normal displacement is in the case of laser beam generated thermal acoustic waves in the range of some pm per mJ pulse energy depending on the material and thickness of the used sample [5]. A powerful laser can yield the surface displacement in the range of some nanometers. Such a motion of the surface can be detected using a capacitive transducer, demonstrated by Hutchins et al. [5, 57, 58]. The advantage of the application of non-contacting sensors like electrostatic, electromagnetic or optical devices, is that they have no mechanical contact with the investigated surface. But in comparison with piezoelectric transducers they have a lower sensitivity. For example, the electrostatic device described by D. Hutchins has sensitivity down to 10^{-12} m [57]. The sensitivity depends on the electrode area, the gap between the electrode and the surface and the applied d. c. voltage as well as the noise level of the electronics. Sensors for detecting a fine surface movement based on the piezoelectric effect have a much higher response, they can detect a displacement in the range of $10^{-14} - 10^{-15}$ m. Devices made from a piezoelectric material are small, cheap, very simple and they have a very high sensitivity especially at their resonance frequencies. But for waveform registration the sensor must have a homogeneous response in a broad frequency bandwidth without significant resonance. Polymer piezoelectric materials are soft plastics and have a quite high coefficient of wave dissipation, so their frequency characteristics are nearly flat with lower sensitivity than in the case of ceramic or crystalline piezoelements. There are also a variety of optical methods of detection of ultrasonic surface motion. The laser-interferometer [60] or the laser beam deflection (knife edge technique) methods [59] can also be used for displacement detection. The knife edge technique is the simplest optical method. The detection limit of such a device is in the order of some picometers. Detectors based on the laser interferometer are more complicated, need a stable low noise laser and complex electronics. Such devices are very expensive and usually not compact. An electromagnetic transducer relies on the interaction of an ultrasound wave with a static magnetic field, imposed on the sample surface with a strong permanent magnet. Such sensors are less sensitive than piezoelectric devices by several orders of magnitude, but this is compensated by a wide bandwidth of the order of 20 MHz [59, 61].

4.2.1 Piezoelectric sensors based on PZT ceramics and PVDF polymer films

Piezoelectric sensors are the most common type of sensors used for ultrasonic measurements. Piezoelectricity is the link between electrical and mechanical phenomena. It was discovered in 1880 on Rochelle salt by the brothers Jaques and Pierre Curie. It is defined as a change in electric polarization with change in applied stress, which is usually referred as the direct piezoelectric effect. In piezoelectric bodies polarization is coupled to stress and vice versa. Piezoelectric sensors are most often used for ultrasonic measurements. The active element of such sensors is a piezoelectric slab or rod usually fabricated from a ferroelectric pure monocrystalline (lithium niobate $LiNbO_3$, lithium tetraborate $Li_2B_4O_7$, quartz SiO_2), or polycrystalline ceramic (lead zirconate titanate $Pb_X(Ti,Zr)_{1-X}O_3$ (PZT ceramic), barium titanate $BaTiO_3$) or a film of piezoelectric polymer material (polyvinylidine fluoride PVDF). A typical structure of a piezoelectric crystal is shown in Fig.4.6. It presents the elementary cell of perovskite type solids like $CaTiO_3$, $BaTiO_3$, $PbZrO_3$ etc. At temperatures higher than the critical temperature T_c the elementary cell is cubic (Fig. 4.6a). At lower temperatures the crystal has a tetragonal distorted elementary cell (Fig. 4.6b). In consequence the distance between positive and negative ions changes. This change is usually very small, however this displacement leads to polarization of the elementary cell with electrical dipoles. Such polarized cells form piezoelectric domains. In ceramics the directions of polarization of the microcrystalline domains are distributed randomly therefore it cannot have piezoelectric behavior. Only after a so called polarization process in a high electric field the ceramic material becomes piezoelectric. This process takes place at temperatures close to T_c . After cooling down the total polarization of the ceramic becomes stable. A following heating of the polarized ceramic aggravates its piezoelectric properties. Mechanical compression or strain of a piezoelectric slab parallel to the direction of its polarization leads to a deformation of all elementary cells and the resulting electric charge appears on the surfaces of the slab. On changing the slab thickness by Δx_e the resulting voltage between the surfaces is

$$U_e = h_{33} \cdot \Delta x_e, \tag{4.1}$$

where h_{33} is the piezoelectric constant of deformation. The electric charge, q, generated in the piezoelectric slab is proportional to the applied force F :

$$q = -d_{33} \cdot F , \tag{4.2}$$

where d_{33} is the piezoelectric charge constant of the material. The electric field E induced in the piezoelectric slab due to the stress σ can be expressed using the piezoelectric voltage constant of the material g_{33} :

$$E = -g_{33} \cdot \sigma, \tag{4.3}$$

In the inverse piezoelectric effect the slab thickness changes upon application of an electric field. This change can be described by

$$\Delta x_s = d_{33} \cdot U_s, \tag{4.4}$$

here Δx_s is the thickness change, and U_s is the applied voltage between the surfaces of the slab perpendicular to the direction of polarization. The properties of different piezoelectric materials are summarized in Table 4.2.

In the case of a 3-dimensional deformation the picture becomes more complicated.

The vector of electric polarization $\vec{P}$ has two components: one proportional to the vector of electric field $\vec{E}$ and one to the stress tensor σ_{ij} [41]:

$$P_k = \varepsilon_0 \cdot \varepsilon_{kj} \cdot E_j + d_{kij} \cdot \sigma_{ij} = \varepsilon_0 \cdot \varepsilon_{kj} \cdot E_j + d_{kM} \cdot \sigma_M; \tag{4.5}$$

where ε_0 is the permittivity of free space, ε_{kj} is the permittivity tensor, $M = 1$ to 6; $i, j, k = 1$ to 3. The matrix d_{kij} is called the piezoelectric strain matrix containing 27 components.

Due to the inverse piezoeffect the strain matrix u_{ij} has an additional term corresponding to the mechanical response on the applied electric field:

(a)   (b)

⬤ A^{2+}- Pb, Ba, other divalent metall
⬤ O^{2-}- Oxygen
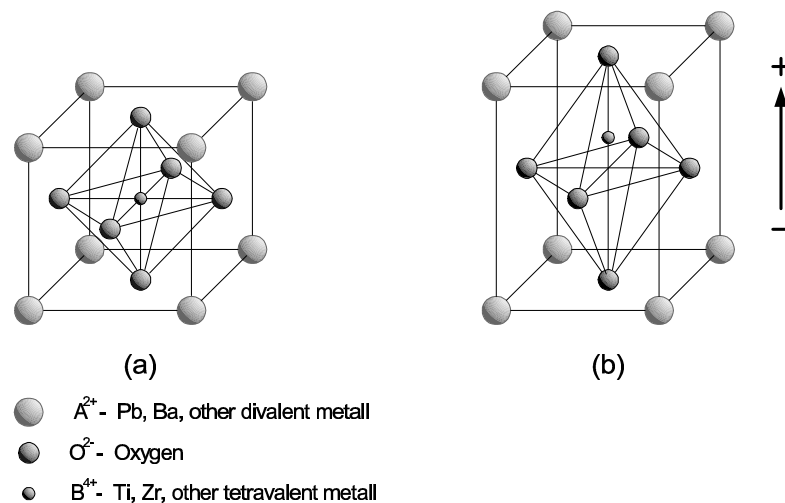• B^{4+}- Ti, Zr, other tetravalent metall

Fig. 4.6. Crystal structure of a traditional piezoelectric ceramic. (a) at temperature above the Curie point; cubic lattice with symmetric arrangement of positive and negative charges. (b) at temperature below the Curie point; tetragonal lattice, the crystal shows an electric dipole.

$$u_{ij} = d_{ijk} \cdot E_k + s_{ijml} \cdot \sigma_{ml} \quad \text{or} \quad u_M = d_{Mk} \cdot E_k + s_{ML} \cdot \sigma_L \tag{4.6}$$

where s_{ijml} is the compliance matrix.

The active piezoelectric element of an acoustic sensor is usually clamped or glued to the surface of a specimen. The main disadvantage of the active element made from ceramic or crystalline material is its pronounced frequency response with a lot of resonances which occur due to the wave reflection from the surfaces of the solid. The fundamental thickness resonance of the sensor occurs when its thickness is exactly half of the wavelength. If the measurements are preformed at fixed frequency and a wide bandwidth is not necessary it is much better to operate at a resonance frequency of the sensor using a piezoelectric with high mechanical quality factor in order to have the highest sensitivity. For wide-bandwidth devices one has to suppress these resonances which distort the shape of the measured signal. One solution was described by Proctor [62]. He proposed to damp the transducer system using a massive brass electrode. Another possibility for the suppression of these resonances is to use a backing material, fabricated from a material with an impedance close to that of the piezoelement. This is usually a polymer loaded with metal powder. It can

Table 4.2 *Properties of piezoelectric materials (PZT and PVDF)*

	APC 880	APC 855	PVDF
Density (g/cm^3)	7.6	7.5	1.78
Dielectric constant, ε	1000	3250	11
Dielectric loss factor, tg(δ)	0.0035	0.02	0.06
Piezoelectric charge Constant (10^{-12} m/V)			
d_{33}	215	580	23
d_{31}	-95	-270	-16
d_{15}	330	720	30
Piezoelectric voltage constant (10^{-3} Vm/N)			
g_{33}	25	19.5	236
g_{31}	-10	-8.8	164
g_{15}	28	27	308
Young's modulus (10^{10} N/m2)			
Y_{11}	9.0	6.1	n. d.
Y_{33}	7.2	4.8	0.03-0.1
Mechanical quality factor, Q_m	1000	75	n. d.
Curei point, T_C (°C)	310	250	~110

absorb an acoustic wave transmitted through the sensor without any reflection. A polymer piezoelectric film also can be a good solution to provide a flat frequency response without any significant resonance [15], but it has a lower sensitivity because of its small piezoelectric constants.

4.2.2 Electrostatic and electromagnetic transducers

The electrostatic transducer relies on a change of capacitance caused by motion of the surface relative to a fixed electrode with an applied d. c. voltage (Fig. 4.7a). This change can be expressed through the distance d between the electrode and the surface and the surface displacement δd:

$$\delta C = -\frac{\varepsilon_0 A}{d^2}\delta d = -C\frac{\delta d}{d} \tag{4.7}$$

The sensitivity of this device depends on the area A of the electrodes, the gap between the electrode and the surface d and the applied d. c. voltage U as well as on the roughness of the surface and it is limited by the noise of employed electronics [58,65,66]. The surface displacement can be easily defined by measuring the variation of the electric charge δq on this electrode using a charge sensitive amplifier:

$$\delta q = U \cdot \delta C = -U \cdot \frac{\varepsilon_0 A}{d^2}\delta d \tag{4.8}$$

Thus the sensitivity of the transducer is limited by the noise level of the charge sensitive amplifier used for measurements. For a typical noise level of 10^{-16} C (~600 electrons) in a frequency bandwidth of about 1-3 MHz the corresponding sensitivity is about 2 pm for a sensor with $A = 30$ mm^2, $d = 20$ μm and $U = 100$ V, i. e. the sensitivity to surface
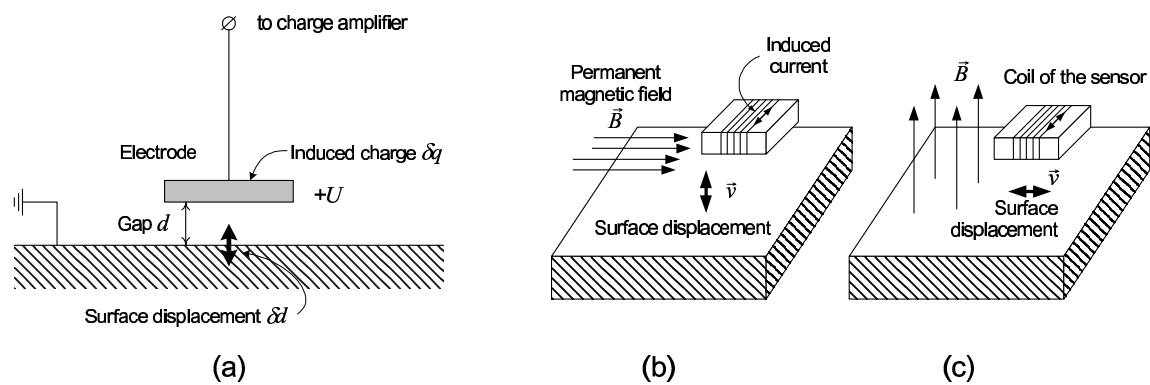

(a)   (b)   (c)

Fig. 4.7. Schematic diagrams of the capacitance (a) and electromagnetic (b, c) transducers.

displacement is in the order of 10^{-12} m as it was reported by Scruby at al. [58]. By increasing the bandwidth the sensitivity gets worse because of a higher noise level. The sensor performance can be improved by increasing the d. c. voltage U and the electrode area A or reducing the distance d, but all these parameters have their own limits caused by break down of the voltage, flatness and roughness of the surface. A capacitive detector can be fabricated using silicon micro-technology. These ultrasonic transducers are mostly resonant sensors with minimum detectable vibration of about $2 \cdot 10^{-16} \, \text{m}/\sqrt{\text{Hz}}$ which corresponds to about 0.5 pm for the frequency bandwidth of 10 MHz [65, 67, 68].

The electromagnetic transducer is another type of a non-contact detector, which relies on the interaction of the ultrasound wave with a static magnetic field, imposed on the sample usually a rare-earth permanent magnet (e.g. CoSm) [7, 8, 61]. During the vibration of the surface with a sufficiently high electrical conductivity, eddy currents are induced at the surface in the presence of a static magnetic field. These currents can be picked up by a suitable coil. The type of acoustic mode detected by this device depends on the coil geometry and the magnetic field distribution of the magnet. In general, if the static magnetic field B is normal to the surface, the electromagnetic sensor will be sensitive to shear waves, while with B parallel to the surface the longitudinal bulk mode will be detected by the device as it is illustrated in Fig. 4.7 (b) and (c). The current induced in the measuring coil is proportional to the velocity, i. e. the first derivative of the surface motion.

Electrostatic and electromagnetic sensors do not rely on a surface of a sample, so they can be used for a moving material or in other cases where contamination of the surface must be avoided. These sensors have a several orders of magnitude lower sensitivity than piezoelectric devices, but a much wider bandwidth. That means that these sensors are able to measure transient movement of a sample without distortion of the signal.

4.2.3 Optical methods of registration of surface motion

There are a variety of optical methods for the registration of a surface motion employing a laser beam.

The knife edge method. This is the simplest optical method of vibration detection. The principle of such a device is shown in Fig. 4.8a. It is based on the deflection of the laser beam reflected from the surface caused by ultrasound motion. If the surface reflects enough light this deflection can be registered by a suitable optical position sensitive detection system, for instance, using a knife edge and a photodiode. Sometimes this
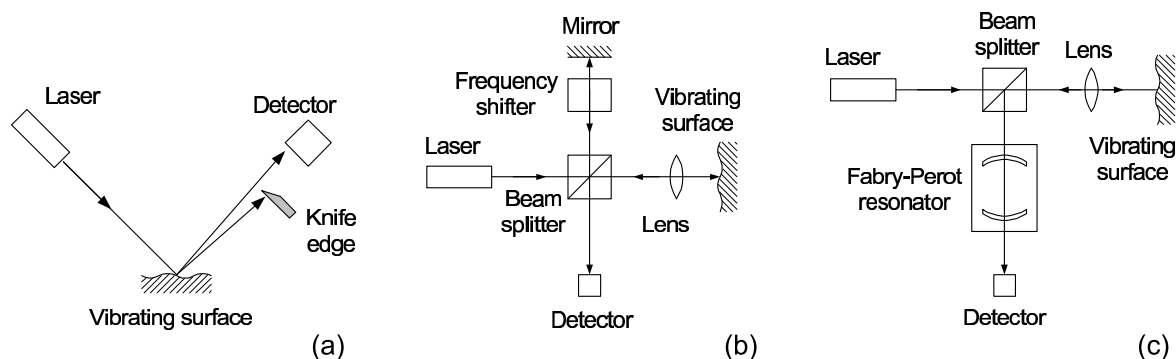
Fig. 4.8. Principles of optical methods: (a) the knife edge technique, (b) schematic of a heterodyne interferometer probe, (c) an interferometer with a confocal Fabry-Perot resonator.

method is applied also with a small cantilever which has a polished top surface for perfect reflection of the laser beam like in an atomic force microscope (AFM). So the sensitivity of the device can be improved and is especially well suited for detecting vibrations on a surface with low reflection coefficient. The minimum detectable amplitude of the vibrations in this method is limited by the noise level of the laser itself and the noise contributions of the photodiode and the electronics. The sensitivity is growing proportional to the distance between the reflecting point and the knife.

Interferometry. In the interferometer type sensor a laser beam splitter is used, which causes some part of this beam to be deflected onto a reference mirror, while the remaining part is reflected from the investigated surface. Then these two beams are recombined at a photodetector as it shown in Fig. 4.8b. Ultrasonic vibration of a surface causes the beam intensity at the detector to change due to interference and forms the detected signal. Using a frequency shifter (e.g. a Bragg cell) allows to extract the low frequency and the device to be more stable. The result is known as heterodyne interferometer, allowing to detect displacements of approximately 2-20 pm [66, 69]. Another type of interferometer is based on the Doppler shift of reflected laser beam by changes in the velocity of the surface movement. One of the methods is to use a confocal Fabry-Perot resonator to detect the laser light frequency changes (Fig. 4.8c). Such a resonator has a maximum of transmission at a well defined optical resonance frequency. Any shift of the frequency caused by the Doppler effect in the beam reflected from the vibrating surface leads to a change in the beam intensity. The detection limit of the optical devices is of the order of some pm [70]. Optical systems with high sensitivity are usually very expensive and quite big in size, so they cannot be introduced into the vacuum chamber in a simple manner.

4.3   Experimental arrangement and results

4.3.1   The experimental set-up

The experimental set-up used in these experiments is illustrated in Fig. 4.9. The needed negative ions are selected by an injection magnet from the initial jet emitted by the ion source. The ion pulse being formed by the blanker and passing the aperture is accelerated and recharged in the Tandetron up to the final energy of some MeV. After the second magnet the selected ions move straight on to the target in the implantation chamber. The bulk elastic waves generated by the ion pulse in the target material are detected by the sensor attached on the back surface of the sample. The signal coming from the sensor is amplified by the preamplifier and digitized using the digital oscilloscope Tektronix 2221A. Via an IEEE488 bus (General Purpose Interface Bus, GPIB) the signal is transferred to a personal computer where it is stored for further analysis. For measuring the current and duration of the ion pulse a Faraday cup is moved temporarily into the ion path. The pulsed current signal is transformed into a voltage and amplified by an I-V converter. For centering the beam on the front side of the sample an aluminum plate with a round aperture of 50 mm in diameter is installed at 20 mm distance in front of the sample surface. A part of the secondary electrons emitted from the sample surface is collected on this plate and forms a current pulse which is amplified and transferred into voltage by the I-V converter and used as a trigger for the oscilloscope.
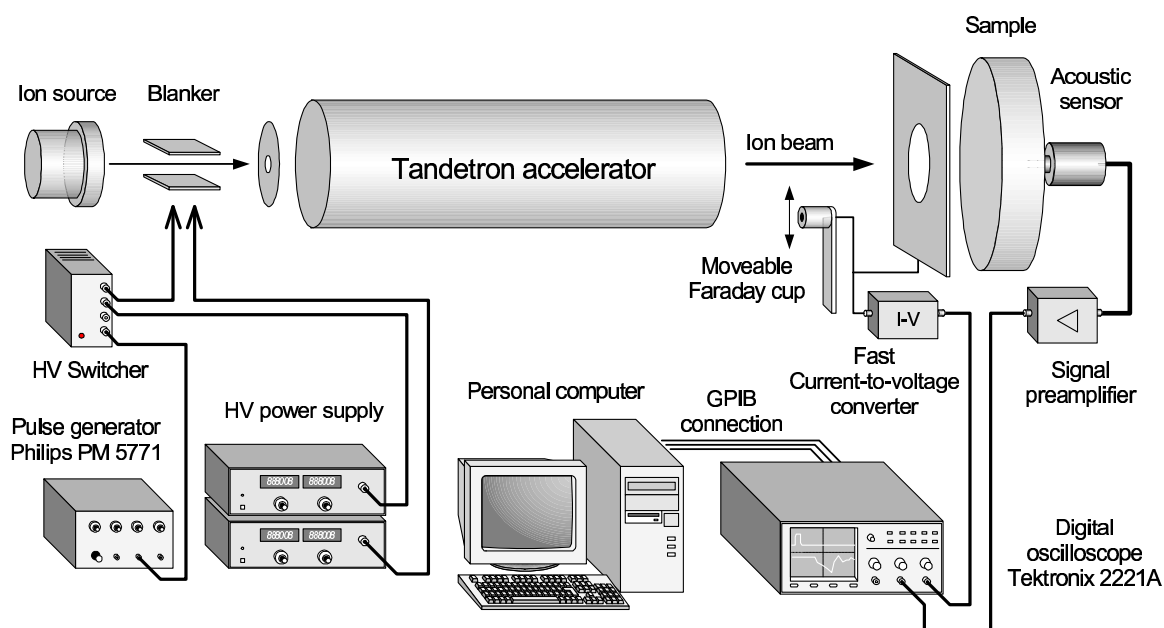

Fig. 4.9. Experimental set-up.

4.3.2 The surface displacement registration system

4.3.2.1 Acoustic sensor

A microsecond long pulse of the ion beam provided by the 3 MeV-Tandetron accelerator usually has an energy of some hundreds of μJ. For example, a 12 MeV Si^{3+} ion pulse with a duration of 1 μs and a typical current of 20 μA has the energy of 80 μJ. This is some orders of magnitude lower than the energy of the laser pulse used by Hatchins and Dewhurst [9]. Compared to that work the surface motion on the back side of the target should be in the range of 10^{-13} m for a 20 - 25 mm thick aluminum sample. This fact underlines a requirement to apply a highly sensitive sensor to detect this motion with a good resolution. Therefore it was decided to employ a piezoelectric sensor for this purpose. For waveform measurement two types of piezoelements are used: a lead zirconate titanate (PZT) piezoceramic APC-855 produced by American Piezo Ceramics (APC) with a mechanical quality factor Q of about 100 and a polymer PVDF film from PIEZOTECH S. A. with a very low Q-factor. As the active element of the sensor a small disc of the PZT ceramic with a diameter of about 2 mm and a thickness of 1 mm was used. This element was installed between two electrodes in a socket as it is shown schematically in Fig. 4.10. The front electrode was made from a soft steel, 3 mm long. Such a layered structure can be
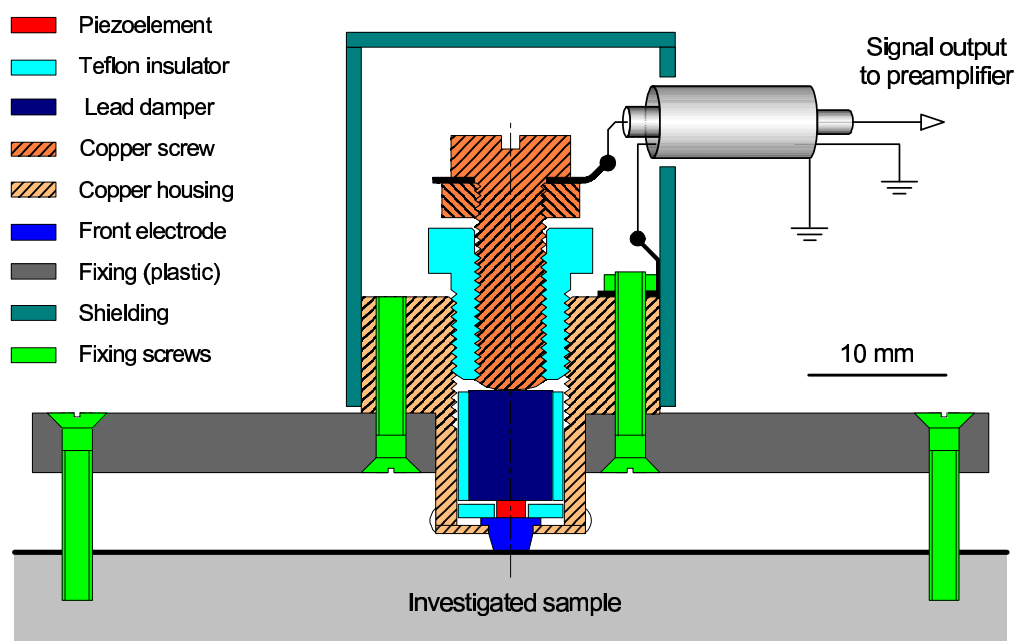

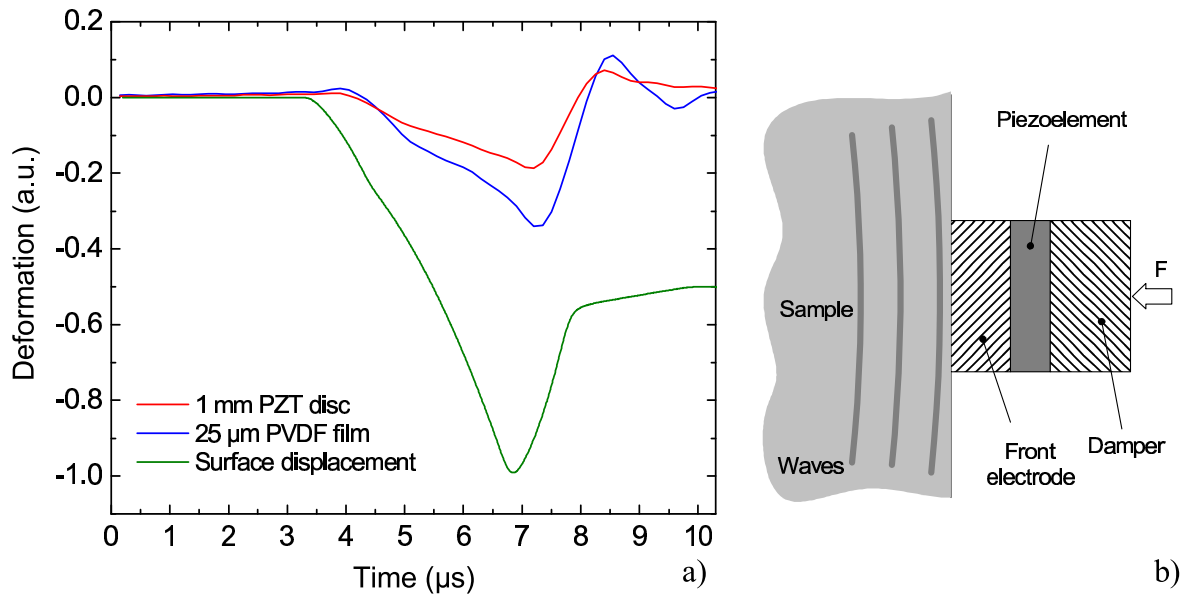**Fig. 4.10.** Design of the surface displacement detector.

Fig. 4.11. Calculated deformation of the piezoelements, namely 1 mm thick PZT disc and 25 μm thick PVDF film, in comparison with the initial surface displacement of an aluminum sample (a). The simplified layered model used for the piezoelectric sensor with applied constant pressing force F (b).

described by a simple model shown in Fig. 4.11b and explained in Appendix. If the sensor touches the investigated surface on an area which is small compared to the distance to the acoustic source, the wave propagating in this structure has the properties of a nearly plane longitudinal wave. So the wave propagation can be roughly described by one-dimensional model. Using this geometry an estimation of the deformation of the piezoelement can be done. In Fig. 4.11a the calculated changes of the thickness of a 1 mm thick PZT disc and a 25 μm thick PVDF film are plotted. As sample material aluminum was used. These deformations are 2.9 and 5.3 times lower than the initial surface displacement for PVDF
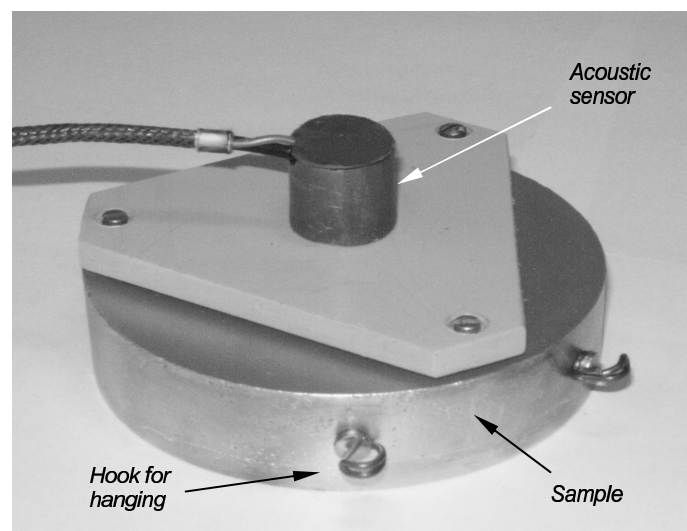

Fig. 4.12. Aluminum sample with attached acoustic sensor. View from back side.

and PZT sensors, respectively. For an iron sample the values are 1.4 and 2.7, and for copper 2.4 and 4.7, respectively. According to the calculation there is no significant dependence of the amplitude on the thickness of the front electrode in the range of 2-5 mm. This thickness leads to a time delay between the surface displacement and the deformation of the sensor. Increasing the front electrode thickness leads to weak oscillations of the signal which change the shape of the waveform. The sensor is slightly pressed on the surface with an estimated force of not more then 20 N. Varying the pressing force in the range from 0 to 20 N shows no visible changes of the signal shape in the calculations which was also seen during the experiment. This can be explained by the providing pressure of about 10 MPa which is negligible in comparison to the elastic constants of the sample and the front electrode (50-200 GPa). The sensor has low sensitivity at low frequencies, because the applied force is proportional to the square of the frequency. This leads to a cutting of the long tail which is in the right half of the waveform of the initial surface displacement (see Fig 4.11a). The piezoelement is damped by means of the second electrode attached to the back side of the sensor. This electrode was made from lead and was introduced in a thin teflon tube for insulating from the metallic housing. The damper is about 8 mm long and 6 mm in diameter. Lead has nearly the same acoustic impedance as the APC-855 piezoceramic and therefore the wave reflected from the interface has very little effect. On the other hand, lead is a dense and soft material, has high attenuation of acoustic waves [71] and just a small part of the wave reflected from the back side of the lead electrode comes to the PZT and can form a weakly decaying standing wave in it, leading to a weak resonance. So the softness of the lead reduces the resonant effects. As a result the sensor has a quite smooth characteristic. This electrode is pressed onto the piezoelement using a copper screw which is fixed in the socket by a teflon tube with a vent on its outer side. Additionally, in order to achieve a good contact, an electroconductive glue was applied between the electrodes and the PZT. The softness of the teflon tube protects the sensor from overpressing and breaking and provides an additional damping effect. The socket itself was made from a brass alloy and was introduced into an outer metallic shielding in order to provide additional protection of the cable from electrical influences. The front electrode is grounded together with the sample by means of a thick flexible wire. The signal is received from the back side electrode via a double screened cable.

The second type of sensors is based on a 25 μm thick PVDF film metallized from both sides which was introduced in the same socket. The electrodes area was 1×1 mm^2. The

sensor was prepared from a stress gauge with a sensitive area of 1mm^2 by cutting. In order to prevent a short cut between these two electrodes the polymer film itself was cut with a bigger area of about 2×2 mm^2. The acoustic sensor was attached to the back side of the sample by means of 3 screws fixing the holder made from a PEEK plastic material as it is shown in Fig. 4.12.

4.3.2.2 Preamplifier

The signal from the sensor is fed into a high frequency preamplifier with a -3 dB level bandwidth from 0.5 kHz to 8 MHz and an amplification factor of about 20000. The frequency characteristic is shown in Fig. 4.13. In the input cascade this preamplifier has a low-noise high-frequency N-channel MOS-FET (field effect transistor) to obtain a high input resistance. The sensor is connected with the preamplifier by a double shielded short cable with a protective screen in order to reduce any influence of parasitic capacitance of the connection. The protected inner shielding of the cable was set on the potential of the source electrode of this FET. This potential is equal to that on the gate of the transistor. This removes any parasitic influence of the cable capacitance which can shunt the sensor at high frequencies and strongly reduce the voltage of the pulsed signal provided by the high-resistance signal source (the piezoelement). The dependence of this voltage U on the sum of all capacities C_n and the electric charge q collected on the electrodes of the transducer,
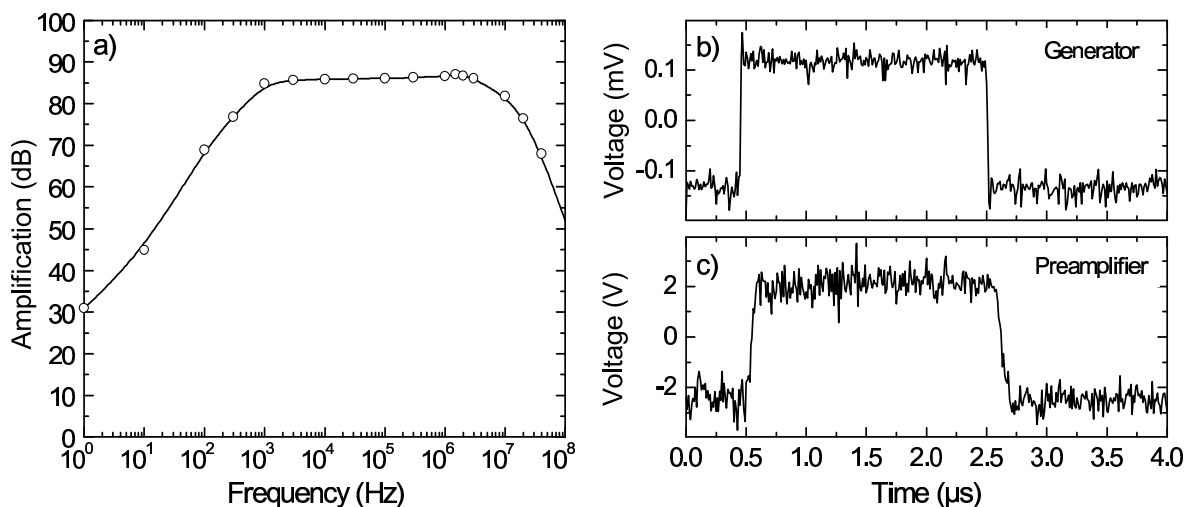

Fig. 4.13. Amplification of the preamplifier as a function of frequency (a) and the test signal from generator on input (b) and on output of the preamplifier (c).

can be written as $U \sim \dfrac{q}{\Sigma C_n}$. The charge q yielded by the piezoelement depends only on the applied force (Eq. 4.2). Any additional parasitic capacitance leads to a reduction of the resulting voltage. In the following cascades low-noise high-frequency operational amplifiers type AD797 and two high frequency amplifiers NE5539 are used. The electronic scheme is shown in Appendix C. The preamplifier is located in the metallic housing and was hanging close to the sensor-sample system in the vacuum chamber in order to reduce all electrical influences as well as to insulate it from mechanical vibrations caused by the vacuum pumps.

4.3.3 Measurements of ion induced elastic waves

4.3.3.1 Experimental procedure

The samples used in this experiment are disc shaped with parallel surfaces. The parameters of the materials can be found in Table 3.1. The longitudinal and the shear waves reach the back surface of the sample one after another with a time difference of:

$$\Delta t = L \left(\frac{1}{c_T} - \frac{1}{c_L} \right), \tag{4.9}$$

where L is the thickness of the sample. This time difference should be much longer than the ion beam pulse length which is about 1 μs. Increasing the thickness of the sample can expand the time scale of the measured waveform. Additionally, the diameter D of the sample should be much greater than the thickness, so that reflections from the side walls arrive the detector much later in order to prevent an interference of the reflected longitudinal wave with the direct shear wave. That means the arrival time of the direct shear wave t_{Shear} must be much shorter than that of the reflected longitudinal wave t_{R_Longit}:

$$t_{Shear} \ll t_{R\_Longit} \qquad t_{Shear} = \frac{L}{c_T} \qquad t_{R\_Longit} = \frac{\sqrt{L^2 + D^2}}{c_L} \tag{4.10}$$

The thickness can be estimated:

$$L \ll D \frac{c_T}{\sqrt{c_L^2 - c_T^2}} \tag{4.11}$$

Usually the shear wave velocity c_T is approximately 2 times lower than that of the longitudinal mode c_L, therefore the thickness of the sample must be smaller than the radius.

The maximum sample diameter which fits into the experimental chamber is about 100 mm, so the thickness was chosen to be about 20 mm in order to allow also measurements of the elastic displacement at a certain distance from the epicenter and to obtain the directivity diagram of the elastic waves. A thicker sample yields a weaker elastic displacement due to the $\frac{1}{L}$ dependence.

In this work metallic samples, like aluminum, iron and copper were investigated as well as silicon. The samples were grounded to prevent a charging up and thus an influence on the signal. In order to reduce the parasitic mechanical vibrations coming from the vacuum system of the beam line, the sample with the attached detector and the preamplifiers are hung in the vacuum chamber by means of two elastic viton bands as it is shown in Fig. 4.5. Digital averaging of the measured signal was employed to improve the signal-to-noise ratio.

The ion induced acoustic emission in aluminum, iron, copper and silicon samples were investigated using oxygen, silicon and gold ions with energies from 1.5 MeV up to 12 MeV. The ion beam was adjusted to obtain a maximum current, centered and focused on the front surface of the sample. The smallest spot diameter of the beam was measured as low as 2 mm using the beam profile-meter. This was done with a constant current of all used beams. After that the beam switch is turned on and the needed pulse duration was adjusted. The oscillogram of the pulsed beam current and the time resolved acoustic waveform measured at the epicenter on the back side of the sample are digitized by the oscilloscope and saved in a PC using LabView code. The surface displacement was registered by PZT or PVDF sensors and compared.

4.3.3.2   Comparison of the PZT and the PVDF sensors

The first measurements were carried out with an aluminum sample and a PZT sensor. A 4.5 MeV Si^{2+} ion beam was used. The pulse current was about 25 μA and the duration 1 μs (Fig. 4.14a). The signal has well pronounced longitudinal and shear steps (Fig. 4.14b). The longitudinal wave needs 3.9 μs in the sample to travel from the front side to the center of the sensor, but the shear component needs about 7.2 μs, corresponding to the wave velocities of about 5900 m/s and 3000 m/s, respectively, taking into account the length of the front electrode of the sensor. These signals are close to that one obtained by Deemer using energetic Si^{3+} and low energy Ar^+ ions and PVDF sensor [15]. From the amplitude of
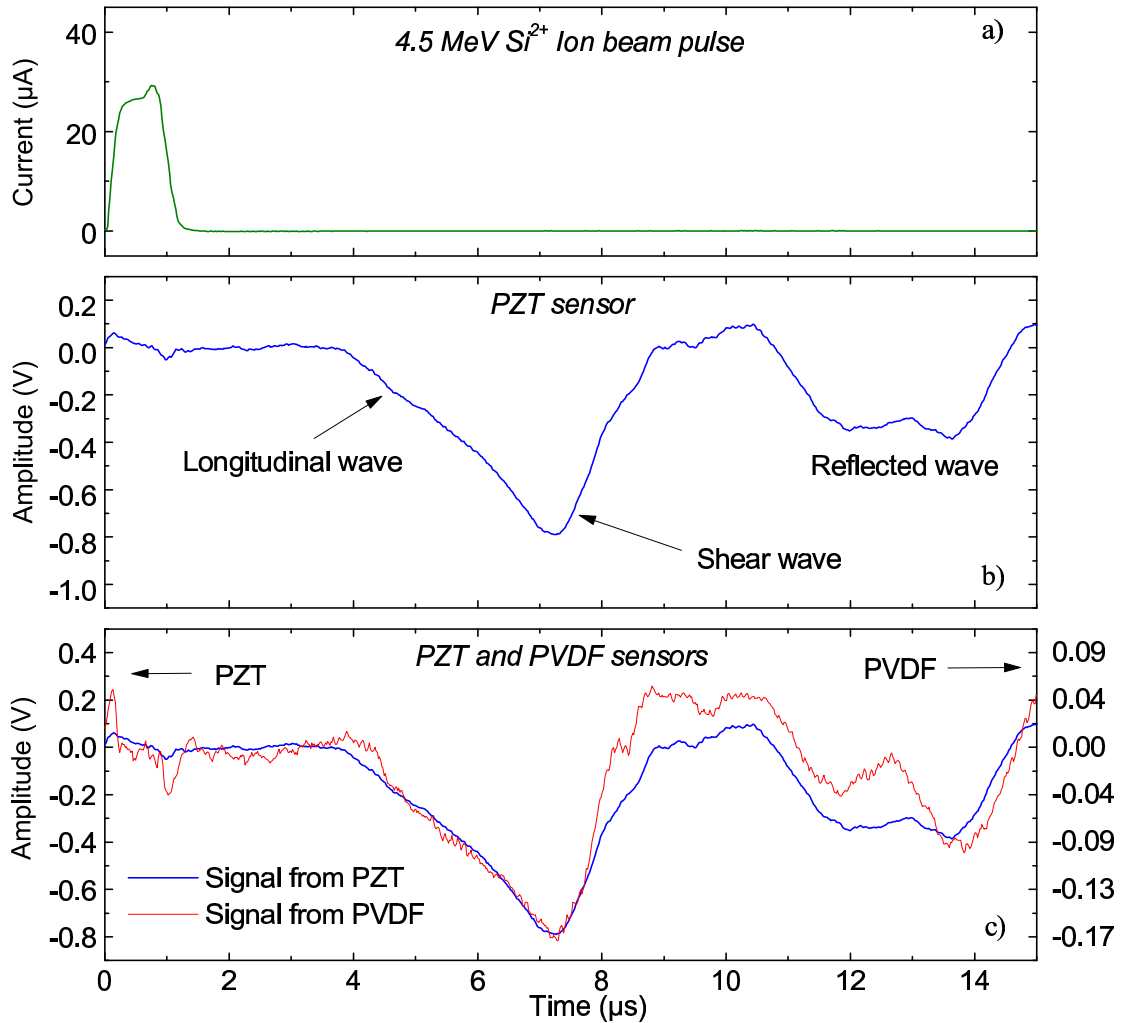
Fig. 4.14. A 1 μs long pulse of Si^{2+} ion beam with energy of 4.5 MeV (a); the elastic waveform measured by the PZT sensor (b). Comparison of the elastic waveforms from the PZT and the PVDF sensors (c). The waveforms are plotted with respect to the signal amplitude to compare the shape.

the signal using the sensor model, described above, the surface displacement can be estimated. The amplitudes of the shear component of the signal of 0.78 V and the longitudinal component of about 0.2 V, measured with ceramic sensor, correspond to a deformation of the PZT disc of about $4.2 \cdot 10^{-14}$ m and $1.1 \cdot 10^{-14}$ m, respectively. This corresponds to a surface displacement of about 0.22 pm and 0.06 pm at an ion pulse energy of about 60 μJ corresponding to 3.7 pm/mJ and 0.9 pm/mJ, respectively. These values are roughly 1.3 times lower then the values of 4.67 pm/mJ and 1.22 pm/mJ using a laser beam generation method and a capacitance transducer on the surface of a 25 mm thick aluminum sample, which is 25% thicker, reported by Hutchins et al. [5]. For a 20 mm thickness due to the $\frac{1}{r}$ behavior the values for the laser excitation should correspond to 5.83 pm and 1.53

pm. The measurement was repeated using a PVDF polymer sensor. The results, obtained by the polymer sensor are 0.17 V and 0.04 V corresponding to the deformation of the PVDF film of about $7.2 \cdot 10^{-14}$m for the longitudinal and $1.7 \cdot 10^{-14}$m for the shear components leading to a surface displacement of about 3 pm/mJ and 0.7 pm/mJ, respectively. The elastic deformation Δx of a slab with a thickness l, a surface area A and a Young's modulus Y_{33} by an acting force F in the one the dimensional case can calculated by the expression:

$$\Delta x = \frac{l}{Y_{33} \cdot A} \cdot F \qquad (4.12)$$

For a 1 mm thick PZT disc of APC-855 with a diameter of 2 mm the coefficient in front of F is $6.63 \cdot 10^{-9}$ m/N and for the used 25 μm PVDF film with an area of 2×2mm^2 the value is $12.5 \cdot 10^{-9}$ m/N, i.e. the polymer piezoelement is 1.9 times more deformable than the ceramic one. In spite of the larger deformation the amplitude of the signal measured with the PZT sensor is 4.5 times higher then that of the signal measured by PVDF. This is a result of lower sensitivity, i.e. lower piezoelectric constant of the polymer piezoelement. The voltage U proved by the piezoelement depends on its deformation Δx, Young modulus Y_{33} and the piezoelectric voltage constant g_{33} as $U = g_{33} \cdot Y_{33} \cdot \Delta x$ (see Appendix D). The
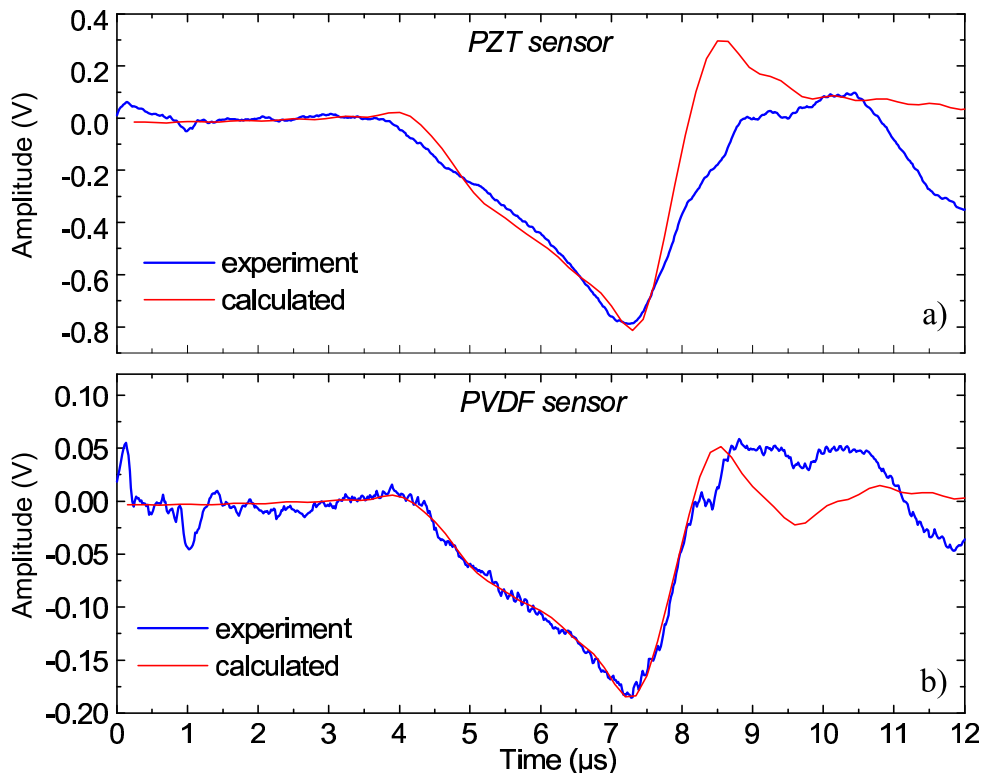

Fig. 4.15. The same experimental waveforms as in Fig. 4.15 and the calculated signal from the PZT (a) and PVDF (b) sensors (qualitatively).

product of the two parameters of the piezoelement, $g_{33} \cdot Y_{33}$, characterizes its sensitivity. Thus for the PZT ceramic the value is about $9.6 \cdot 10^8$ V/m and for PVDF – only $1.2 \cdot 10^8$ V/m. Their ratio is 8.1. Taking into account the ratio of the deformations Δx (Eq.4.12), one obtains a ratio of the yielded signal of 4.3, very close to the measured value of 4.5. A comparison of the waveforms is shown in Fig. 4.14c. These waveforms are obtained by averaging data sets containing about 1000 curves each. In Fig. 4.14c the same curves are normalized with respect to the amplitude to compare the waveforms. Obviously they slightly differ: the signal yielded by the PVDF sensor has somewhat steeper slopes, the longitudinal step is more pronounced. This can be a result of a wider frequency band width of the mechanical characteristic of the PVDF sensor and so as a result of the high frequency components of the signal. This can also be seen on the calculated waveforms in Fig. 4.11a. The shapes of the waveforms are very close to the signal calculated using the simplified sensor model and the theoretical surface displacement of an aluminum sample caused by a thermal elastic wave (see Fig. 4.15). The expected signal shape calculated for the PVDF sensor fits the experimental waveform (Fig. 4.15b), however the signal yielded by the PZT sensor deviates a little bit from the calculated one, but qualitatively it has the same shape. A possible reason may be the thickness of the piezoelements: the polymer element is much thinner than the ceramic one, the PZT element has the diameter-to-thickness ratio of 2 and therefore for more precision the waves, propagated in the sensor, will differ from the plane wave which is used in this model. In general, the waveforms in both cases (PZT and PVDF sensors) have the same structure. Therefore for further investigations the PZT sensor was employed because of higher sensitivity.

4.3.3.3   Dependence of the ion acoustic effect on the ion beam parameters

In Fig. 4.16a waveforms generated in aluminum by a Si^{2+} ion beam with different pulse durations of 0.5 μs, 1 μs and 2 μs are shown. For comparison of the shape they are plotted with a normalized amplitude in Fig. 4.16b. With increasing duration of the beam pulse the signal slopes become gentler. In Fig. 4.16c a comparison of the measured using PZT sensor and calculated waveform from 0.5 μs long ion pulse are shown. In this case the calculated curve fits the experimental one better than in Fig. 4.15a. There is also some variation of the shear wave arrival time, because for the longest ion pulse (2 μs) the signal maximum comes nearly 0.5 μs later. The signal amplitude is proportional to the ion beam

pulse duration and the ion current. These were more precisely measured using 7 MeV O^{3+} ions, demonstrated in Fig. 4.17. A similar result was obtained by Kimura et al. [10] using periodically modulated low energy H^+ ions on a silicon target and Kambara et al. [11] using Xe ions on an Al_2O_3 sample.

Additionally with the same beam of 7 MeV O^{3+} ions the dependence of the signal on the beam spot size (Fig. 4.18a) was investigated, also plotted in terms of corresponding power density (Fig. 4.18b). There was no significant dependence of the acoustic emission on the power density found in the range of 100-1000 W/cm^2 measured at the constant total beam power, corresponding to a spot size of 2 to 6 mm in diameter. This fact can be explained by the dependence of the expanding volume of the sample on the temperature rise δT [5]:

$$\delta V = 3\alpha V \cdot \delta T = 3\alpha V \cdot \frac{P\tau}{VC_p\rho} = 3\alpha \cdot \frac{P\tau}{C_p\rho} \,. \tag{4.13}$$
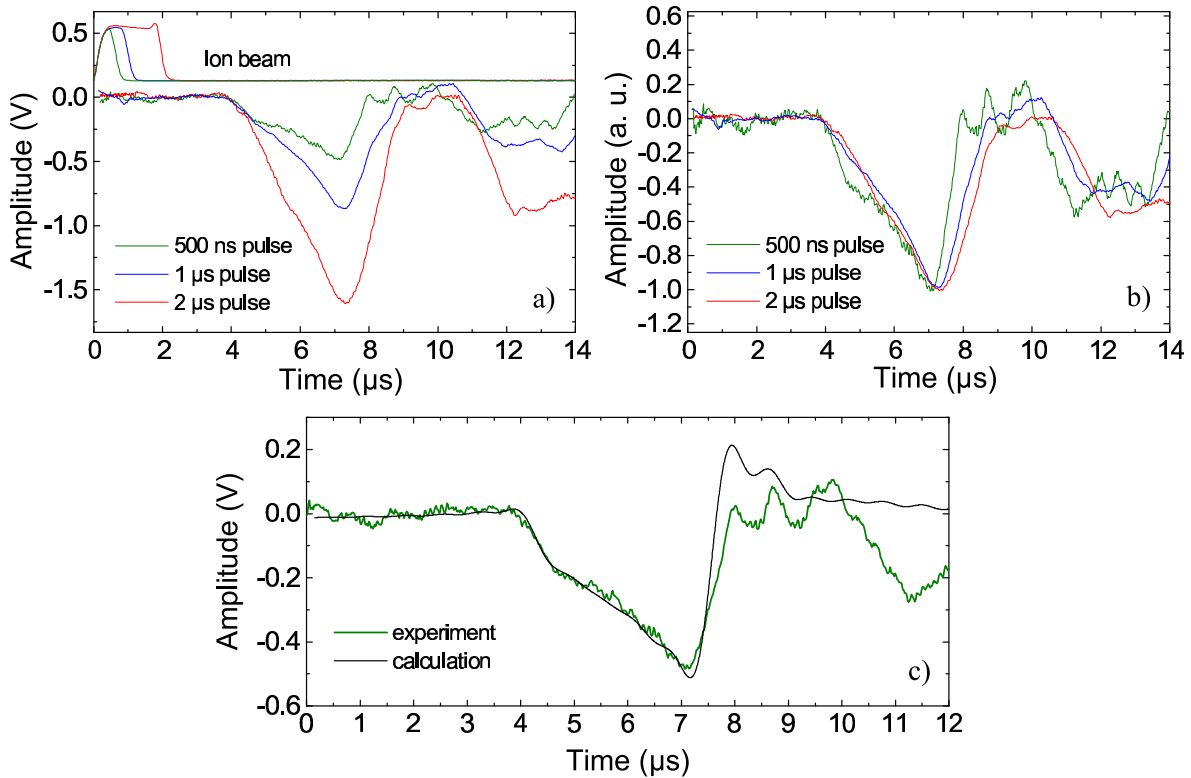

Fig. 4.16. The elastic waves generated in an aluminum sample by a 5 MeV Si^{2+} ion beam with pulse durations of 0.5 μs, 1 μs, 2 μs and measured using the PZT sensor. The waveforms plotted in graph (a) are normalized with respect to the beam current. Graph (b) shows the same curves normalized by amplitude of the signal. In graph (c) the waveform obtained using 500 ns ion pulse and the calculated signal are shown for comparison.
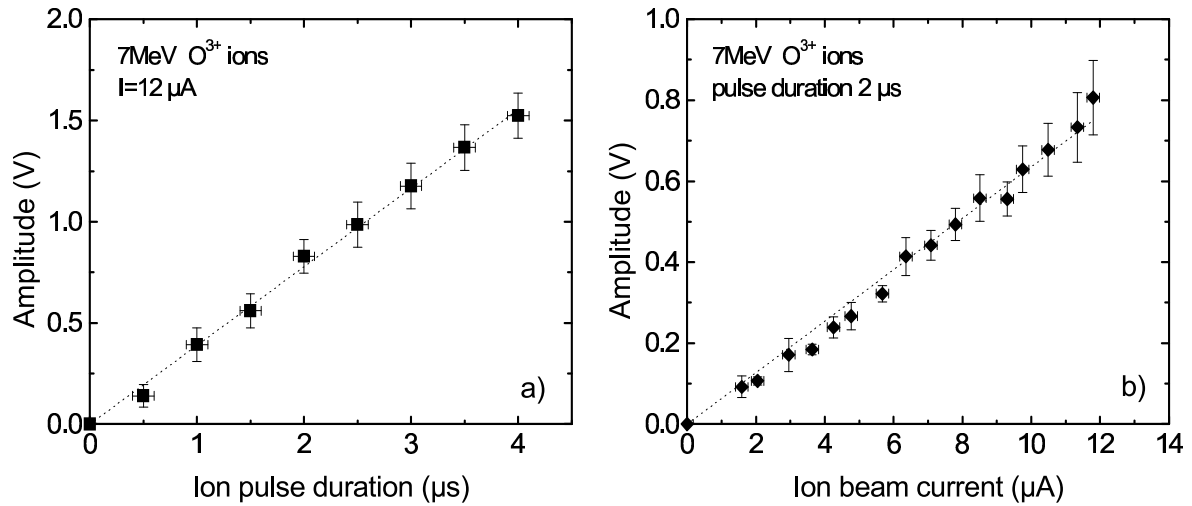
Fig. 4.17. Amplitude of the elastic waves as a function of the ion beam pulse duration at constant current of about 12 μA (a) and as a function of the ion beam current at constant pulse duration of 2 μs (b) measured using a pulsed O^{3+} ion beam with energy of 7 MeV on a aluminum target. The signal was measured at epicenter.

So the volume change δV due to thermal expansion in a sample does not depend on the heated volume V itself. This means that the beam spot size has no influence on the intensity of the wave. The same behavior was found by Dehurst et al. [9] in the case of laser induced acoustic emission in the power density range of 2-16 W/cm^2.

The energy dependence of the ultrasound pulse generation can explain the main mechanism of the process. The thermal elastic effect linearly depends on the energy, however the mechanical momentum transfer from the incident ions generates a sound wave
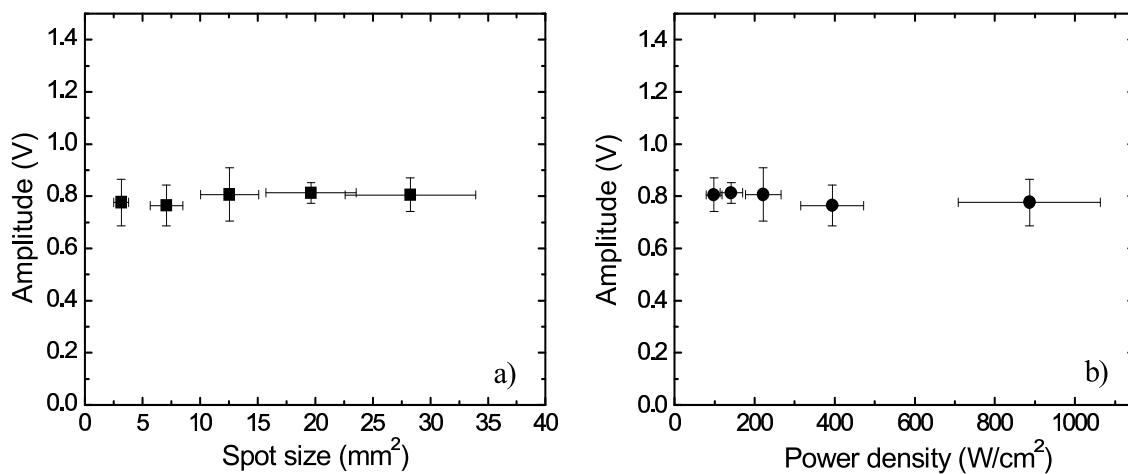

Fig. 4.18. Amplitude of the elastic waves as a function of the spot size (a) of a pulsed O^{3+} ion beam with an energy of 7 MeV and a pulse duration of 2 μs at a constant current of 12 μA. The same data points are shown in terms of ion beam power density (b).
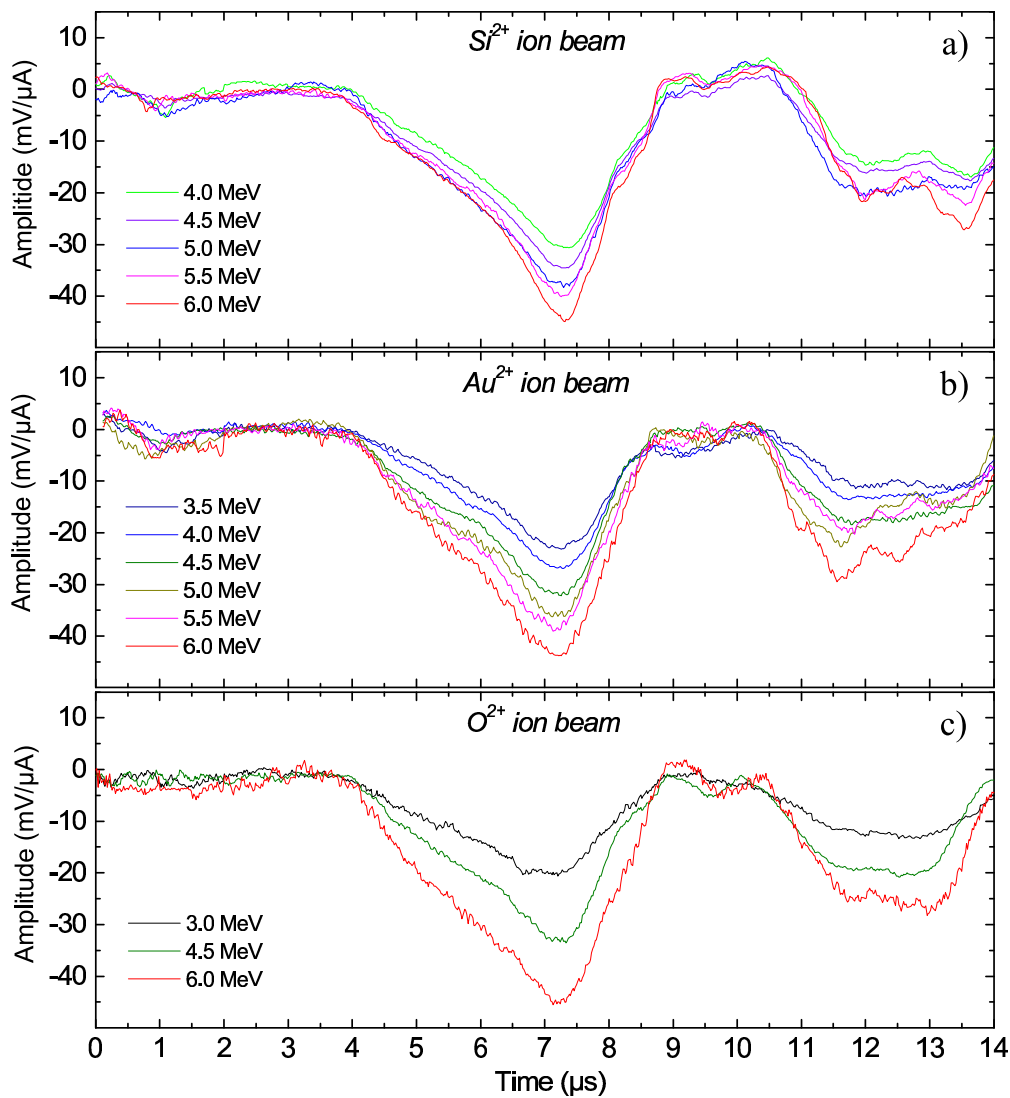
Fig. 4.19. Waveforms measured on an aluminum sample using different ions with equal charge state, namely Si^{2+}(a), Au^{2+}(b), O^{2+}(c) and different energies. The pulse duration is 1 μs. The signal is normalized with respect to the ion current.

with an amplitude proportional to the square root of the ion energy. So by analysis of this dependence one can find out which effect dominates. For this purpose ions with different energies in the range from 2 MeV to 6 MeV were used. The obtained waveforms for oxygen, silicon and gold ion beams, all with an equal charge state of 2+ are presented in Fig. 4.19. The amplitude of the signal is normalized with respect to the ion current. The shapes of the curves show no visible changes at different energies. Due to the lower current in the case of oxygen and gold ions the corresponding signals are more noisy than the signal obtained using silicon ions. The amplitude values for the shear components are plotted in Fig. 4.20. The amplitude increases linearly with the energy. The same behavior was found by Deemer for Si^{3+} ions in the energy range 7-12 MeV and Ar^+ ions with
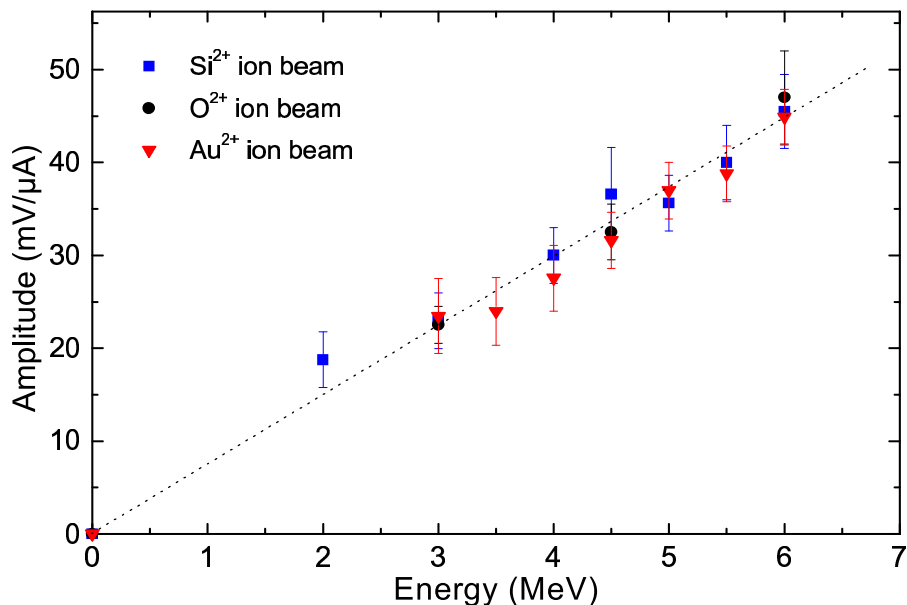
Fig. 4.20. The signal amplitude as a function of the ion beam energy for Au^{2+}, Si^{2+}, O^{2+} ions. The signal is normalized with respect to ion current.

energies 4-11 keV [15]. All experimental data points can be fitted by a straight line. This means that there is no significant dependence on the mass of the incident ions and momentum transfer not important. Only the energy of the pulse is the important parameter for sound generation in this energy range. Also the charge state dependence of oxygen ions in the range from 1+ to 4+ was investigated and the corresponding acoustic signal in aluminum was measured. The results are shown in Fig. 4.21. Fig. 4.21a demonstrates the signal amplitude as function of energy for different charge states. The signal amplitude in this graph was normalized with respect to the electric current of the ion beam pulses. All data points can be fitted well by linear functions. These fits show a different slope for each charge state, steepest for the lowest charge state. The amplitude of the signal is lower for ions with higher charge because of the lower power of the ion beam pulse with the same electric current. The four points in Fig. 4.21b are extracted from Fig. 4.21a and normalized with respect to the ion flux and energy in order to see an effect of the charge state of the incident ions. In Fig. 4.22 the acoustic waveforms generated by a 6 MeV Au ion beam are shown for charge states of 2+, 3+, and 4+ corresponding to a current of 18, 8.5 and 1.7 µA, respectively. The signal is normalized with respect to the energy of a pulse. The lower beam currents also lead to relatively higher noise. Thus the acoustic signal from the 1.7 µA 4+ beam is more noisy. According to the discussion above one can conclude that there is no visible dependence of the waveforms on the ion charge state in the range up to a charge of 4+.
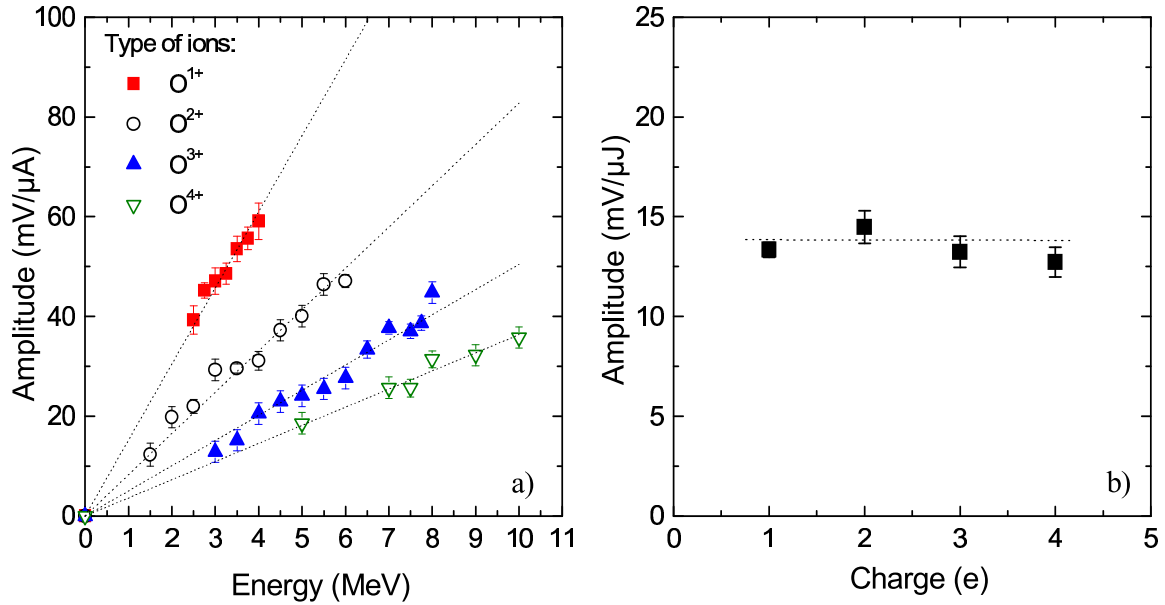
Fig. 4.21. Energy dependence of the acoustic signal measured on aluminum at different energies of the incident oxygen ions corresponding to charge states 1+, 2+, 3+ and 4+ (a). The pulse length is 1 μs. The data points in b) are given as a signal amplitude per unit of the ion current, in a) per unit of ion pulse energy.

The irradiation of a sample by an ion beam, pulsed or continuous, leads also to a modification of the material near the surface in the depth about R_p and can change its thermal and elastic properties during the implantation. Waveforms which were measured at a different times after starting the irradiation look nearly the same, as it shown in Fig. 4.23
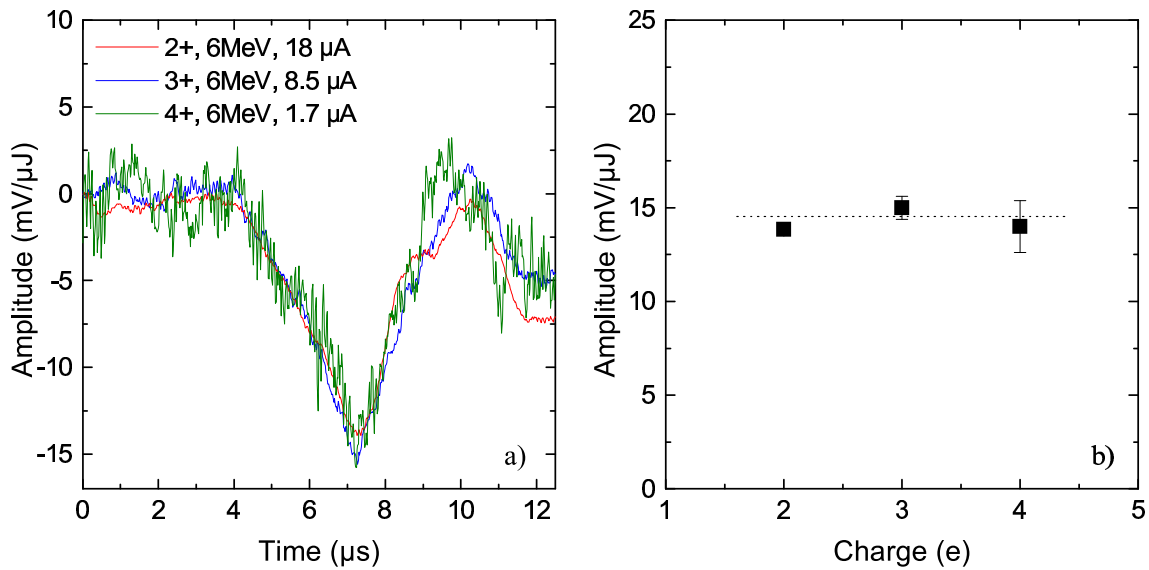

Fig. 4.22. Waveforms obtained by a 6 MeV Au ion beam with a pulse duration of 1 μs and charge states 2+, 3+, 4+ (a) and corresponding amplitude dependence on the ion charge (b). The signal is normalized with respect to the ion pulse energy.
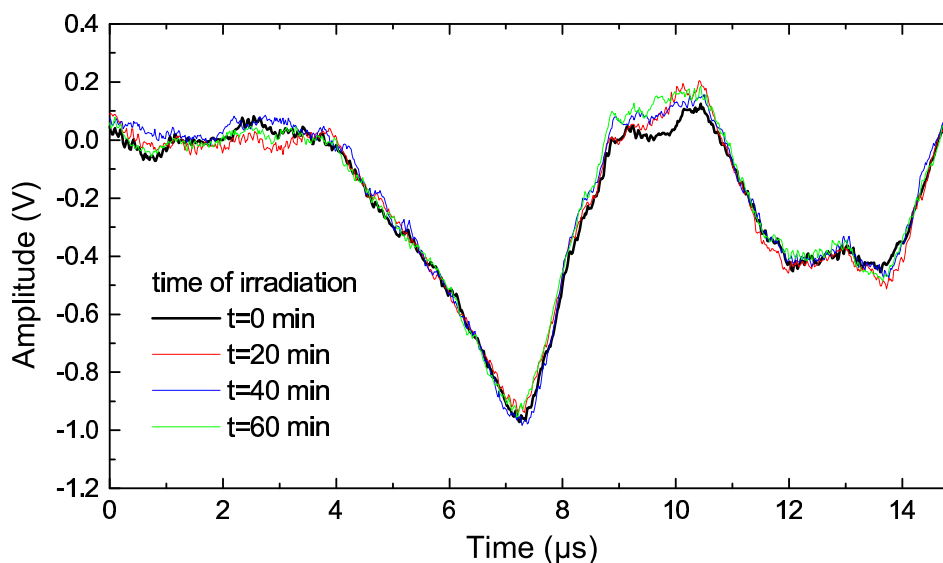
Fig. 4.23. The acoustic waveforms measured on Al sample using 1 µs long pulses of a Si^{2+} ion beam with energy 4.5 MeV and current of about 30 µA in a pulse. The waveforms were obtained at different time after starting of irradiation by the pulsed beam with repetition time of 10 ms.

within one hour of pulsed beam operation. The dose which was integrated during this time is about 10^{15} cm^{-2} corresponding to a peak density of $5 \cdot 10^{18}$ cm^{-3}, or in other words, only 80 ppm of density of the aluminum, $6 \cdot 10^{22}$ cm^{-3}. This value cannot change the material parameters significantly, but nevertheless to prevent accumulation of this effect during a long time, the target surface was polished and cleaned after each set of measurements. In order to avoid the direct exposition of the sample surface on the continuous ion beam the movable Faraday cup was used for blanking during the beam profile measurements. By a much higher dose the acoustic signal can be strongly changed as it was found by Adliene et al. [72] in the case of 100 keV Ar^+ and H^+ ions incident on an aluminum target. The influence of the dose started from the value of about 10^{16} cm^{-2} with the Ar ion range of about 100 nm, corresponding to a peak density of implanted ions of about 10^{21} cm^{-3}, i.e. some percent of the target density. It was also shown by Sieger et al. [73] that the intensity of the acoustic emission does not change during implantation of 4 MeV protons in aluminum with a dose of $5 \cdot 10^{18}$ cm^{-2}. The heat diffusion decreases the effect of the material modification because of reduction of the relative weight of the modified volume in the heated one.

In order to investigate the waveforms at a certain polar angle from the epicenter, the ion beam was scanned over the front surface of the aluminum sample with an increment of 2 mm. For a sample with a diameter much larger than the thickness this is equivalent to the
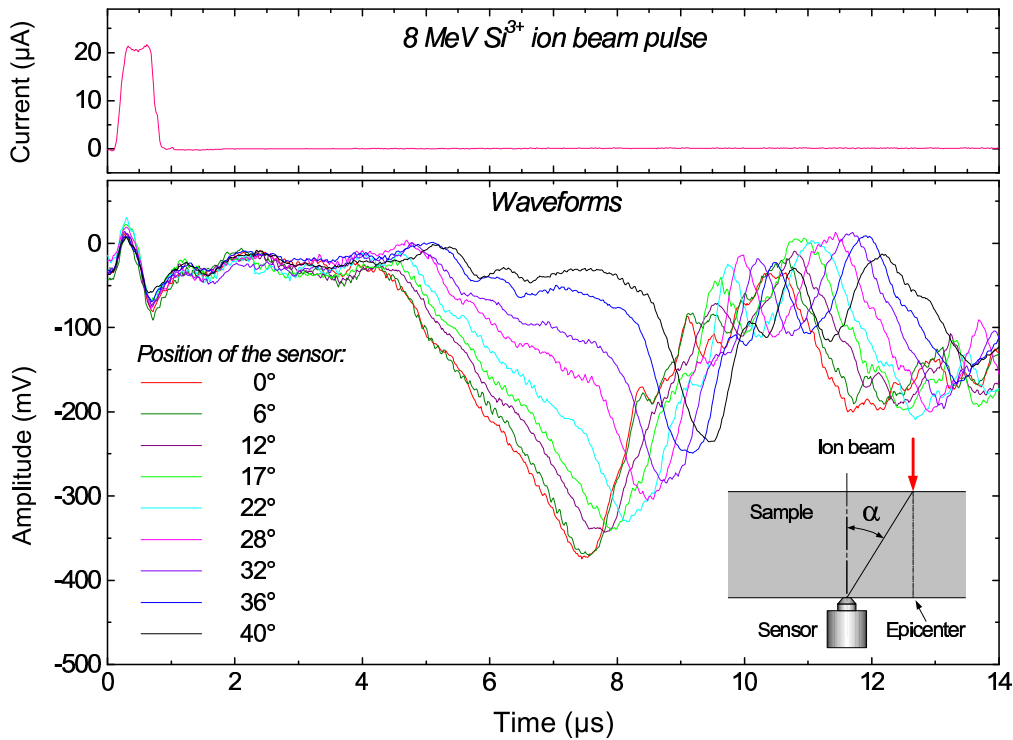
Fig. 4.24. Acoustic waveforms obtained on aluminum sample at different angles from the epicenter. 8 MeV Si^{3+} ion beam. The pulse length is about 500 ns.

case of moving the sensor on the back side of the sample. By moving the detection point away from the epicenter the waveform changes drastically. First of all due to increase of the distance between the acoustic source and the sensor the arrival time of the wave increases and the amplitude of the signal drops down. Also the wave vector in the point of measurement is not perpendicular to the surface of the sample and therefore a coupling between the longitudinal and the shear modes occurs. This leads to a change of the ratio between these components in the waveform as it can be seen in Fig. 4.24. For amorphous isotropic media the signal depends only on the polar angle between the source and the point of detection. In the case of crystalline material the signal behavior depends also on the axial orientation of the sample.

4.3.3.4   Different metallic samples

To investigate the influence of the material properties on the waveforms iron and copper samples were irradiated in addition to aluminum. The comparison is presented in Fig. 4.25. For different materials one gets different signal amplitudes and shapes. In the left graph the curves are shown in original scale normalized due to the ion flux. In the right graph the
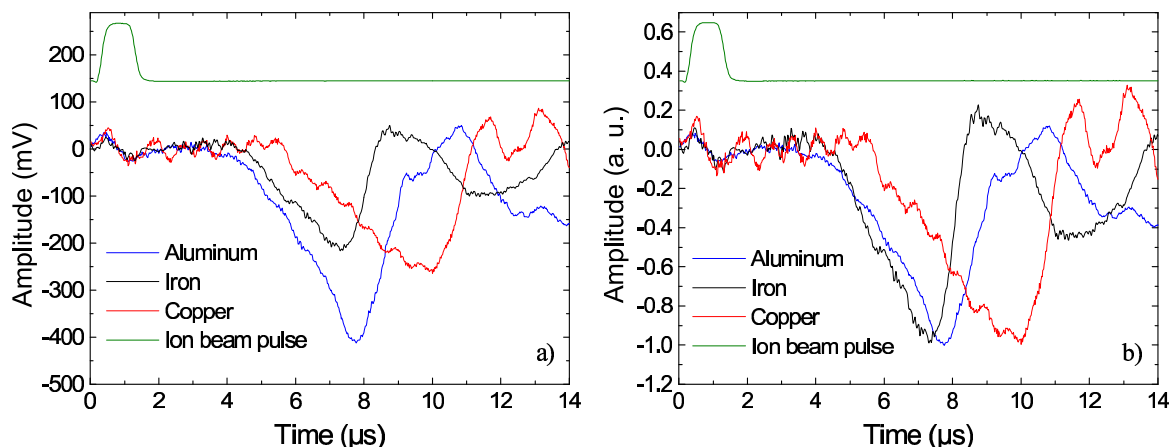
Fig. 4.25. Acoustic waveforms on different target materials, namely aluminum, iron, and copper samples. 6 MeV Si^{3+} ion beam with pulse duration of about 1 µs. The signal is normalized by ion current of 15 µA (a) and the signal amplitude (b).

waveforms are normalized to the peak amplitude. The different amplitudes and arrival times can be explained by the different elastic wave velocities and thermal properties.

The thermal elastic displacement u of the sample is proportional to the thermal expansion coefficient α and the temperature rise δT, which depends on the ion pulse power P and the duration τ and the material parameters, like the density ρ and the specific heat C_P:
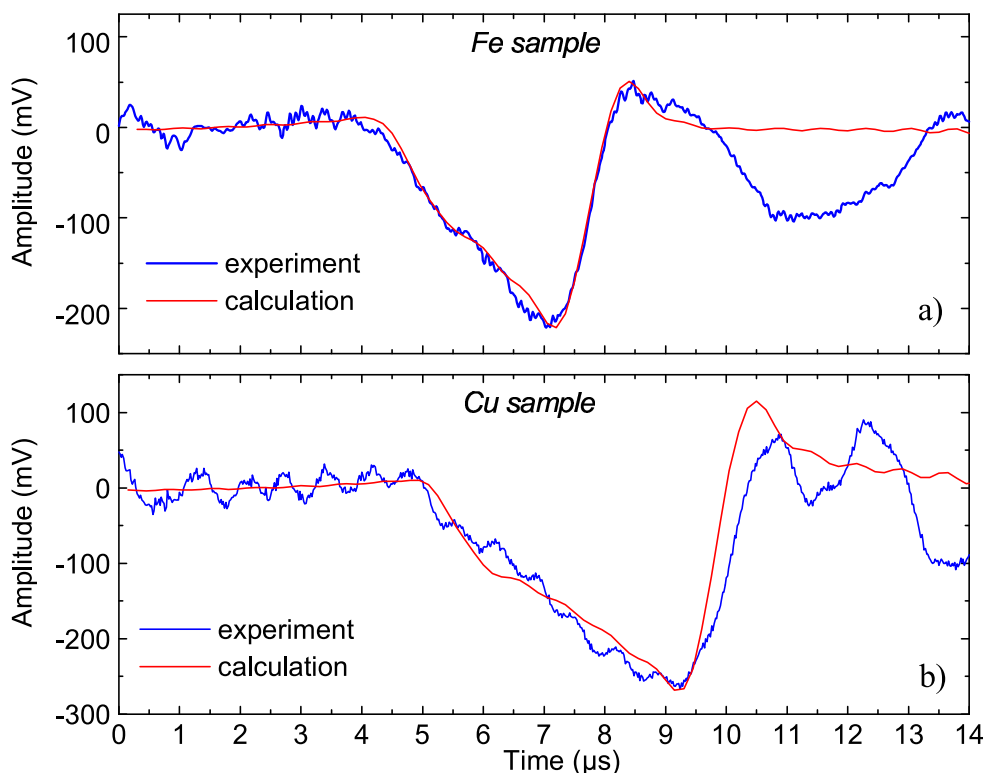

Fig. 4.26. The same experimental waveforms as in Fig. 4.25 and the calculated signal shape (qualitatively) for an iron (a) and a copper (b) samples.

$u \sim \alpha \cdot \delta T \sim \dfrac{\alpha}{\rho C_p} \cdot P\tau$. So the thermal-acoustic properties of every sample (material)

can be characterized by the coefficient $\dfrac{\alpha}{\rho C_p}$. For aluminum this coefficient is equal to

$3.6 \cdot 10^{-11}$ m³/J. For copper and iron the values are $1.84 \cdot 10^{-11}$ m³/J and $1.29 \cdot 10^{-11}$ m³/J,
respectively, corresponding to 51% and 35% of that for aluminum. The maximum acoustic
signal was registered on aluminum sample. The amplitudes of the signal obtained on
copper and iron samples are 64% and 53% of that for the aluminum sample. The ratio
between the initial surface displacement on the sample and the deformation of the sensing
PZT element is about 5.2 for aluminum and ~4.7 and ~2.7 for copper and iron,
respectively. Taking into account the difference of the sensitivity of the sensor attached on
different materials, the real displacements can be estimated as 0.11 pm (3.7 pm/mJ) for
aluminum, 0.065 pm (2.17 pm/mJ) for copper and 0.028 pm (0.93 pm/mJ) for iron. This
corresponds to 59% and 26% for copper and iron, respectively (signal value for aluminum
is taken as 100%). The waveforms for iron and copper samples obtained at different
energies of a Si^{3+} ion beam and energy dependence for these samples are shown in Fig.
4.27. Also for copper and iron samples the data points could be fitted by linear functions
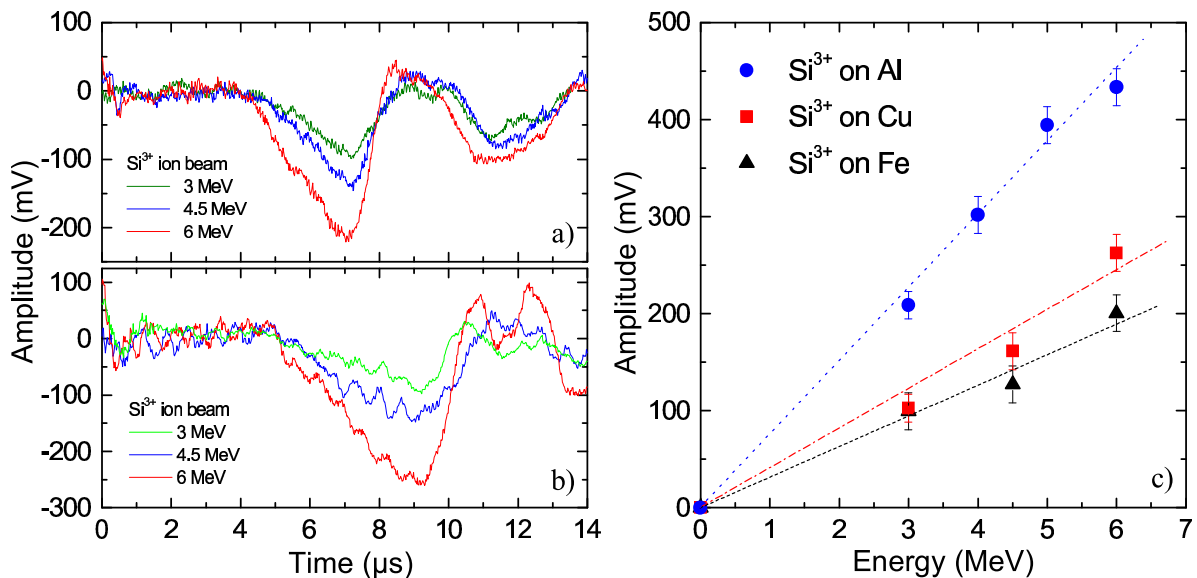(Fig. 4.27b).

Fig. 4.27. The waveforms measured on iron (a) and copper (b) samples at different ion
energies and corresponding dependence of the amplitude of the acoustic waveforms on the
energy of a Si^{3+} ion beam for different target materials: aluminum, iron, and copper (c).
The beam pulse duration is 1 µs. The signal is normalized with respect to an ion current of
15 µA.

4.3.3.5   Crystalline silicon sample

Specimen. For these experiments a crystalline 4 inch Si <111> disc with a thickness of 15 mm was taken. The sensor was installed in the same manner as in the case of the metallic samples. The sample was introduced in the vacuum chamber without a fine alignment of the beam axis to the normal of the crystal, due to the difficulty to combine the vibration insulation with a precise mechanical movement mechanism (goniometer). Therefore the following data were obtained not aligned in channeling direction of the silicon sample.

Experimental data. A set of measurements of several energies of incident ions and different position of the acoustic source were carried out. The Si^{3+} ion beam pulse duration was nearly 750 ns. The graphs obtained at different ion energies are shown in Fig. 4.28a. These waveforms have a completely different shape than for metallic samples. In these acoustic signals one also can define longitudinal and shear components, the signal polarity is also negative. Amplitude data points extracted from these waveforms are introduced in Fig. 4.28b and fitted by a linear function.

Variation of the polar angle gives a similar effect as in the isotropic case, the signal tends to change polarity from negative to positive on increasing the angle, shown in Fig.4.29. In order to demonstrate the anisotropy of the silicon sample an attempt to
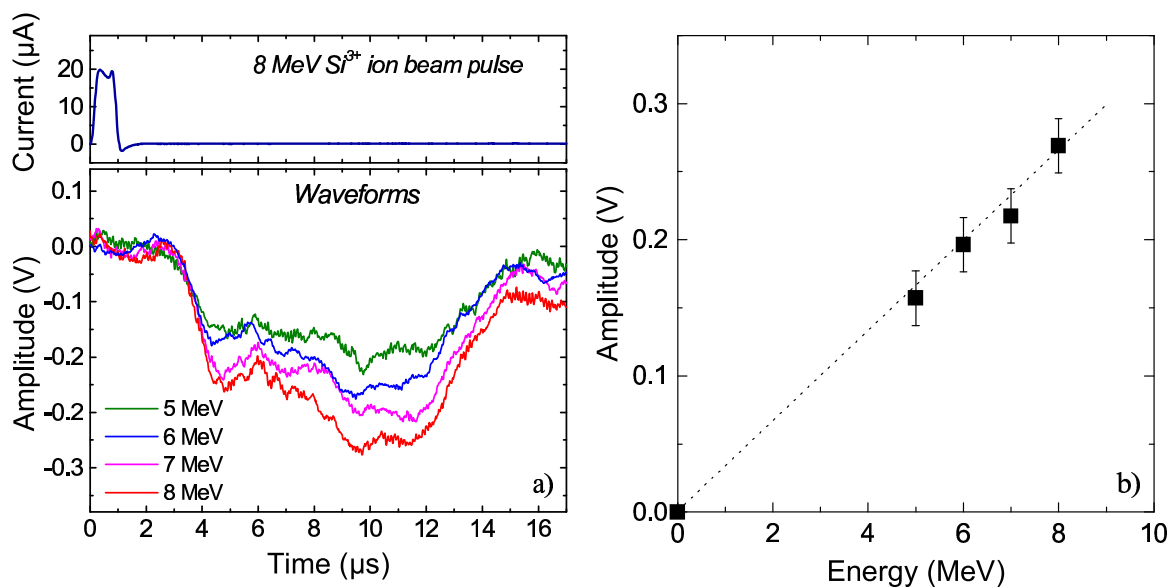

Fig. 4.28. Waveforms measured on Si <111> sample using Si^{3+} ions with energies 5, 6, 7 and 8 MeV (a). The signal is normalized by ion current of about 20 µA. Dependence of the maximum of amplitude of acoustic waveforms on energy of Si^{3+} ion beam measured using Si<111> sample (b).
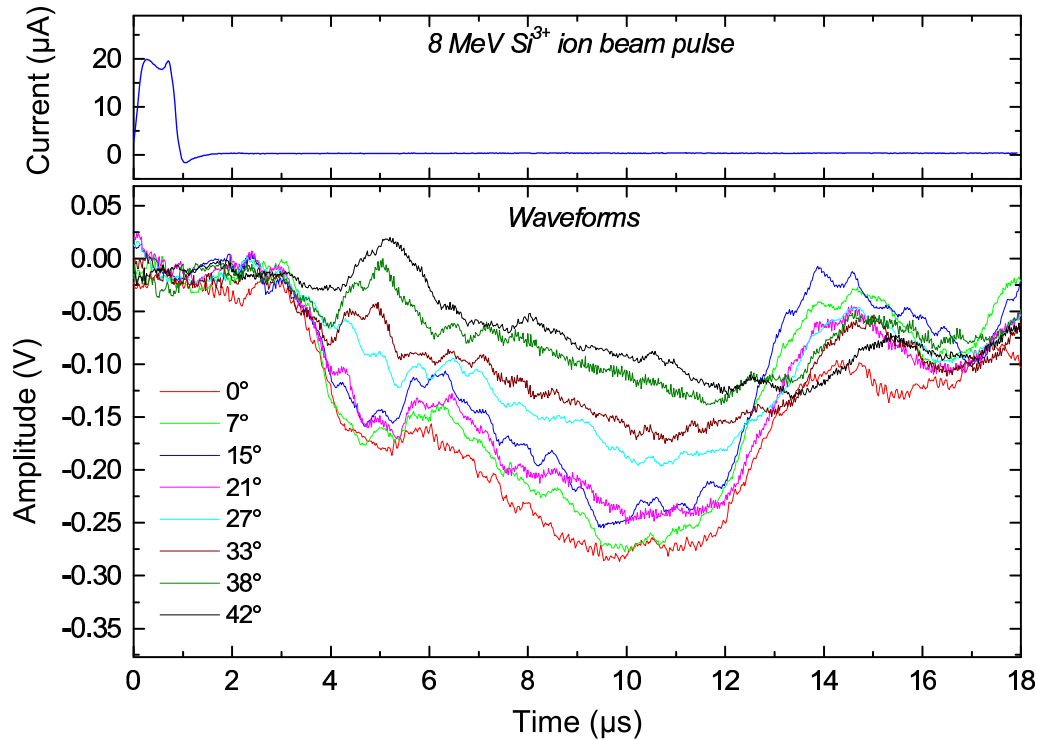
Fig. 4.29. Waveforms measured on Si <111> at different distance from the epicenter. 8 MeV Si^{3+} ion beam with pulse duration of 0.75 μs and current of about 20 μA was used.

visualize the arrival time and the signal amplitude as a function of the beam position was done. The scan step was 2.5 mm, i. e. nearly similar to the ion beam spot size. The scan field was a square with a side length of 20 mm and the image size was of 8×8 pixels. In Fig.4.30 the images (a) and (b) are plotted using the arrival time of the signal maximum for the longitudinal and the transversal components of the bulk acoustic wave, respectively.
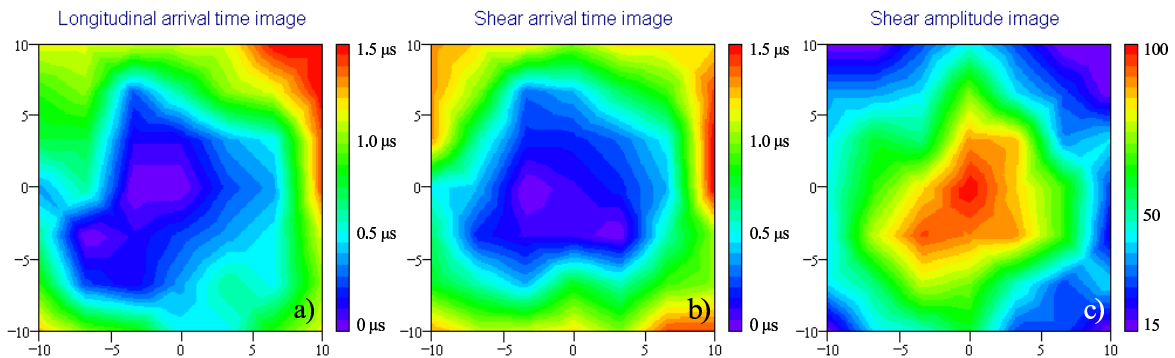
Fig. 4.30. Visualization of the signal arrival time (a, b) and amplitude (c) of the acoustic waves in a Si <111> sample. Every pixel in the images (a) and (b) represents arrival time of the signal relative to the one in the epicenter. The amplitude image shows the maximum of signal in every pixel (in arb. units). The images were obtained using an O^{2+} pulsed ion beam scanned over the target surface. The imaged field size is 20×20mm^2.

The pixel color represents the time difference between arrival of the wave in this pixel and arrival time in the epicenter. For isotropic media the propagation time of the wave depends only on the length of the path so the images should have a circular symmetry. The image in Fig. 4.30c is based on the maximum of the amplitude of the signal. All these three acoustic images on silicon are asymmetric. This is most likely result of anisotropic crystalline structure of the sample. The elastic properties of a crystal depend on orientation, so the wave velocities and arrival time also are functions of orientation. Moreover, in some directions the wave can be focused by the crystal as it was discovered by Taylor et al. [74]. Due to the small size of the images or in other words the big spot size of the ion beam the resolution is quite low and it is difficult to define a crystallic orientation. In some works for visualization of bulk elastic waves in crystals a pulsed laser beam was employed [42, 75]. A high power and small spot size are the big advantages of the laser beam allowing nanosecond pulses and providing high image resolution.

4.4 Summary

The ion induced bulk acoustic wave emission was experimentally investigated in aluminum, copper, and iron using high-energy oxygen, silicon and gold ions in several charge states. The shape of the observed waveforms agrees very well with expectation, assuming the dominance of the thermal mechanism of the elastic wave generation in the energy range of 1-10 MeV. This is also confirmed by the linear dependence of the bulk sound amplitude on the incident ion energy. The main mechanism of sound generation in a solid with clean surfaces, found for ion acoustics is the same as in the photo-acoustic effect [5, 7, 9, 12]. The sound emission occurs due to the transient heating of the solid in near surface region. The momentum transfer from the used ions has a relatively small influence on the waveforms which could not be resolved in the measurements. In order to avoid any contribution to the measured signal from evaporated impurities, the surfaces were cleaned before irradiation. A polishing before each set of measurements also prevents possible influences of surface modification during previous ion irradiation. No visible dependence on the ion mass was found for oxygen, silicon and gold. A contribution of the ion charge state to the acoustic effect is also negligible in the range of the charge number from 1+ to 4+. The process of propagation of sound in crystalline silicon <111> is different from that of isotropic media and depends on crystalline orientation, but also in silicon the behavior of energy dependence remains linear in the energy range up to 10 MeV.

5. Application of the Ion Acoustic Effect for Microscopy

In this chapter a possible application of the ion acoustic effect in microscopy is described. A modulated focused ion beam (FIB) is used for generation of the sound wave in a target. The experiments were carried out on IMSA-100 FIB system in Rossendorf.

5.1 Acoustic testing of materials

For a long time ultrasound has been used for nondestructive inspection of materials. The concept of ultrasonic metal flaw detection was first suggested by Sokolov in 1928 at the Electrotechnical Institute of Leningrad in USSR [76]. In 1931 Mülhäuser obtained the first patent for his ultrasonic device [77] in which he used a transmission technique for flaw detection in metals. Later on Sokolov demonstrated that sound waves could be used in a new type of microscope. In 1949 he recognized that a microscope using sound waves with a frequency of 3 GHz would have a resolution in water comparable to that of an optical microscope [78]. The principles of modern defectoscopes and echo-pulse methods were invented in 1939-1942 by Firestone [79] in the USA, Desch and Sproule [80] in the UK, and Kruse [81] in Germany. Firestone produced his patented "supersonic reflectoscope" in 1941, which for the first time employed the reflection-technique. He modified a radar instrument and developed a transmitter with short pulses and an amplifier with short dead-zone. An early commercial model of the original "reflectoscope" designed by Firestone in 1941 was manufactured by the Sperry Company at Danbury, Connecticut, in the United States. In the 30's the first attempts to construct devices for converting ultrasound to optical images were made. The first such device was designed by Pohlmann in 1937 [82]. In the early 70's the first acoustic microscopes were built by Lemons and Quate [83]. Starting from that time focused laser and electron beams have been employed for ultrasound generation in materials under examination [84-86]. In the 80's first attempts of

using an ion beam from an implanter modified for this purpose were reported [13]. Today ultrasound has found a wide field of applications in defect controlling for all kinds of nondestructive inspection of materials in industry, transport, medical research, science, etc.

5.2   Principles of Scanning Acoustic Microscopy

There are two concepts in acoustic microscopy. In scanning acoustic microscope an investigated sample is irradiated by an ultrasound which is generated outside of the sample by a transducer and focused on it by acoustic lenses [87-89]. Another possibility is to generate elastic waves directly in the sample by an intensity modulated laser beam [84,90], an electron [91-94] or ion beam focused on the sample surface [13]. Heating by the modulated beam leads to thermal waves in the sample. Temperature propagation in a solid is described by the thermal diffusion equation Eq.(3.20). For a sinusoidal temperature modulation with an angular frequency ω and an amplitude T_0 at the surface plane $z = 0$ the temperature distribution is a function of sample depth z and time t can be written as [95]:

$$T(z,t) = T_0 \cdot \exp\left(-\frac{z}{d_{th}}\right) \cdot \sin\left(\omega t - \frac{z}{d_{th}}\right). \qquad (5.1)$$

The thermal waves caused by the modulated beam are exponentially damped with the decay length equal to the thermal diffusion length d_{th}, depending on the materials properties and the beam modulation frequency Eq. (3.23).

   The thermal waves interact with discontinuities in the target and thus they can be applied for the nondestructive inspection of thermal structures in the solid [95, 96]. In 1962 White demonstrated the possibility of using transient heating to generate elastic waves by electron bombardment or RF-radiation absorption [1]. Acoustic emission occurs due to periodic thermal expansion as a result of transient heating of the target surface. This method is used in scanning photo-acoustic (SPAM) [84-86, 97, 98], scanning electron-acoustic (SEAM) [92-94], and scanning ion-acoustic microscopy (SIAM) [13].

   When ultrasound is generated by a laser beam or a beam of particles focused on the surface of a specimen, the acoustic source is located in the near sub-surface region. The source depth h_{source} is defined by the beam penetration depth d_P and the thermal diffusion length d_{th} in the sample:
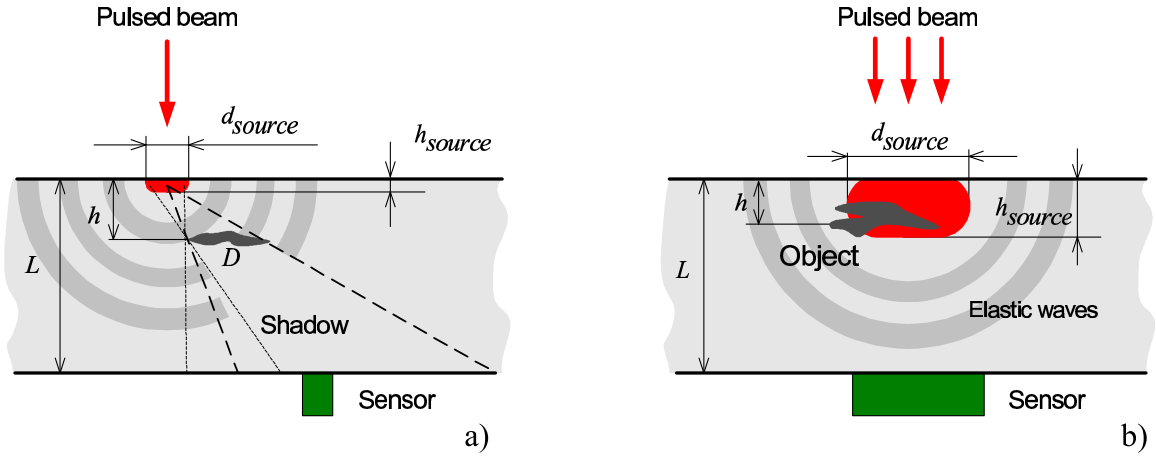
Fig. 5.1 Two modes of acoustic imaging: the inspected structure is in far field region (a) and the structure inside the acoustic source (b).

$$h_{source} = \sqrt{d_{th}^2 + d_P^2} \; . \tag{5.2}$$

Its lateral diameter d_{source} depends also on the beam spot size d_S and the lateral size of the energy dissipation volume d_V:

$$d_{source} = \sqrt{d_S^2 + d_V^2 + d_{th}^2} \; . \tag{5.3}$$

This represents the volume where the thermal wave is converted to an elastic wave and therefore determines the size of the acoustic source. With increasing frequency the thermal diffusion length d_{th} becomes shorter and the volume becomes smaller.

Different mechanisms of acoustic imaging are possible depending on the depth of the investigated place in the sample. If an investigated structure in the specimen is deep enough so that the depth h is much larger than the depth of the acoustic source h_{source}, $h \gg h_{source}$, and the acoustic wavelength Λ is much shorter than the depth, $h \gg \Lambda$, this structure is in the far-field region and can be imaged due to a shadowing effect, i. e. its acoustic shadow is geometrically projected on the sensor (Fig. 5.1a). Moving this shadow during scanning of the beam leads to a variation of the sound amplitude and phase which can be measured and visualized. In this case the lateral resolution is defined by the linear size of the detector, A, the acoustic source diameter d_{source}, the wavelength of the sound according to diffraction, the geometry of the sample and the depth of the structure. The resolution can be estimated as:

$$d \approx \frac{h}{L} \sqrt{d_{source}^2 \cdot \frac{(L-h)^2}{h^2} + A^2 + \frac{\Lambda^2}{D^2} \cdot (L-h)^2} \; . \tag{5.4}$$

Due to reflections of the image of the inspected object from the sample surfaces it is more useful to make time resolved measurements of the acoustic response induced by a

single short pulse of the beam instead of continuously modulated one. One sound detector can give information about the lateral size and the shape of the evaluated structure only. If many sensors are applied a 3-dimensional imaging becomes available [98] with a depth resolution in the same range as in the lateral case.

Another imaging mechanism is based on the sound emission process near the target surface and determined by local thermal and elastic properties of an inspected area in a specimen. By this mechanism the depth of the imaged object $h < h_{source}$ (the investigated structure is inside the acoustic source, shown in Fig. 5.1b) and only surface and near subsurface structures can be visualized. Amplitude and phase of the emitted ultrasound are changed if some inhomogeneities of the target material are located in the sound generation volume. The lateral resolution depends on the size of the acoustic source and is a function of the thermal and elastic parameters of the target and the beam modulation frequency f:

$$d = d_{source} = \sqrt{d_S^2 + d_V^2 + d_{th}(f)^2} \ . \tag{5.5}$$

At high frequencies the contribution of the thermal diffusion length becomes negligible relative to the other parameters according to the relation $d_{th} \sim 1/\sqrt{f}$, at low frequencies resolution of the image is derived from this value.

5.2.1 Application of a focused ultrasound beam for microscopy

In acoustic defectoscopes piezoelectric transducers are used mostly for emission and detection of ultrasound waves. To obtain a high resolution the sound has to be focused to a
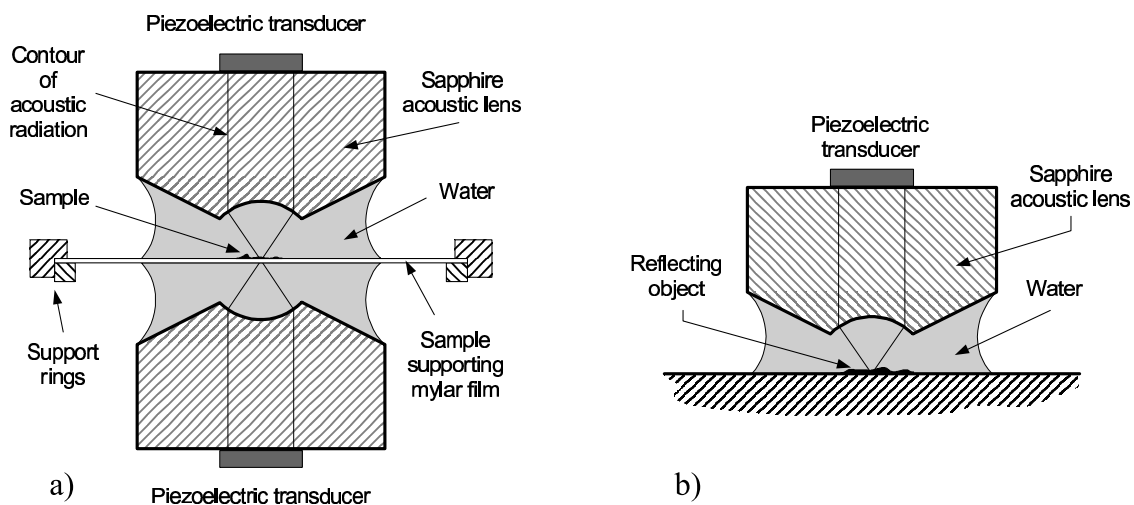

Fig. 5.2 Sketch of an ultrasound microscope operating in transmission (a) and reflection (b) modes.

small point on the investigated sample using spherical acoustic lenses or Fresnel acoustic lenses. The principle of such a microscope is comparable to that of optical systems. In the first acoustic microscope a specimen was introduced in a water cell between a pair of single surface sapphire acoustic lenses to focus the ultrasound as shown in Fig. 5.2a [87]. It was based on a transmission technique where two transducers were attached on the external flat surfaces of the lenses, one for emission and the second for detection of
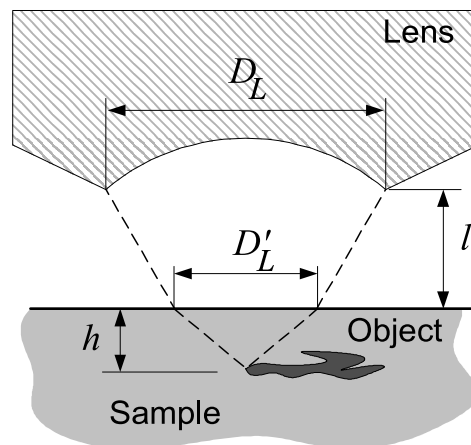

Fig. 5.3 Resolution of a microscope using ultrasound.

ultrasound transmitting through the sample. Applying the pulse reflection technique only one lens with the transducer is necessary for the emission as well as for the detection of the reflected sound (Fig. 5.2b) [87, 99]. The resolution of such an imaging system as in the case of optical systems depends on the ultrasound wavelength λ, the diameter D_L and the focusing length F of the lens as well as the distance between the lens and specimen surface l and the depth h of the inspected region (Fig. 5.3) and can be written as [99] :

$$d = 0.64 \cdot \lambda \cdot \frac{h}{D'_L}, \quad D'_L = D_L \cdot \frac{F - l}{F}. \tag{5.6}$$

At frequencies of some GHz the wavelength in liquids and solids becomes as short as some microns and at frequencies higher than 10 GHz the acoustic microscope can reach, in principle, a better resolution than optical devices.

5.2.2 Photo-acoustic microscopy using a focused laser beam

In the scanning photo-acoustic microscope an intensity modulated or pulsed laser beam focused on the surface of the investigated sample generates ultrasound in the material [84, 85, 89, 97, 100]. The acoustic source depth is defined by the light penetration in the target which can vary over a wide range depending on the material and the wavelength of the light. A laser beam in the visible light wavelength range can be focused to a spot of 0.5-1 μm. Therefore the lateral size of the sound source cannot be smaller than the spot size of the beam, and the lateral resolution of such a system under optimum conditions is nearly in the same range as for optical microscopes.

5.2.3 Scanning electron acoustic microscopy (SEAM)

The electron beam in a SEAM has a spot size of about ten nanometers. This parameter is negligible compared to the size of the electrons' energy dissipation volume. The low mass of electrons leads to long paths in the material followed by a broad scattering the so called proximity effect [2]. This volume depends mainly on the material density and the energy of electrons. Approximately, the diameter of a hemisphere of penetration and spreading of a focused electron beam is [101]:

$$d_{e-penetr} \approx 0.2\,\frac{E^{1.43}}{\rho}\,, \tag{5.7}$$

where $d_{e-penetr}$ is in μm, the energy E given in keV, and the material density ρ in g/cm^3. A typical value of this diameter for 30 keV electrons penetrating into silicon is about 11 μm, in aluminum about 10 μm, and about 3 μm in copper [94]. This parameter is the limiting factor of the acoustic source size and thus the lateral resolution in the case of SEAM.

5.2.4 Scanning ion acoustic microscopy (SIAM)

Using a modern FIB system one can reach a spot size of about 10 nm for gallium ions at a FIB current of some pA and about 100 nm at a current of more than 1 nA. The advantage of the FIB is the short ion ranges in solids from 20 to 100 nm in different materials for an ion energy of about 30 keV. This means the lateral resolution of a SIAM can reach the sub-micron range at a sufficiently high modulation frequency of the FIB. Another advantage is the possibility to use the FIB for analysis as well as a tool for specimen modification or cutting for further investigations simultaneously. Disadvantages are the low ion beam current leading to a very low acoustic signal and damaging of the inspected sample by the FIB due to sputtering.

5.3 SIAM based on the IMSA-100 FIB system. Experimental arrangement.

The aim of this part of the work is to use an intensity modulated FIB for acoustic excitation and to apply it as a Scanning Ion-Acoustic Microscope. A periodically modulated ion beam leads also to a thermal wave coupling which is the general mechanism of the acoustic

Fig. 5.4. IMSA-100 FIB system

emission by local periodical heating of the sample. The incident ions deposit their energy in the so called dissipation volume of the material through various processes. A part of the initial energy is lost in the sample by sputtered particles, secondary electrons and photon radiation. The first attempt to use the ion-acoustic effect for microscopy was done by Rose et al. in 1985 [13]. For this purpose they employed a 200 keV ion implanter and used a N_2^+ ion beam with an energy of 100 keV and a current of about 10 μA which could only be focused to a spot size of about 6 mm. The Rossendorf FIB system IMSA-100 provides ions with energy of 25-50 keV (for singly charged ions) and on ion current of some nA for a FIB with a spot size smaller than 1μm. A few years ago the evidence for the generation and detection of acoustic waves in an aluminum sample was provided by Teichert et al. using the IMSA-100 FIB system [14].

5.3.1 IMSA-100 FIB system

Focused ion beams are useful tools in micro- and nanoengineering. The FIB can provide sub-micrometer spot size, an energy range from some eV up to 200 keV and an extremely high current density. The IMSA-100 is a FIB system of own development which was built at the end of 80's in the Research Center Rossendorf [53] (Fig. 5.4). The basis of the
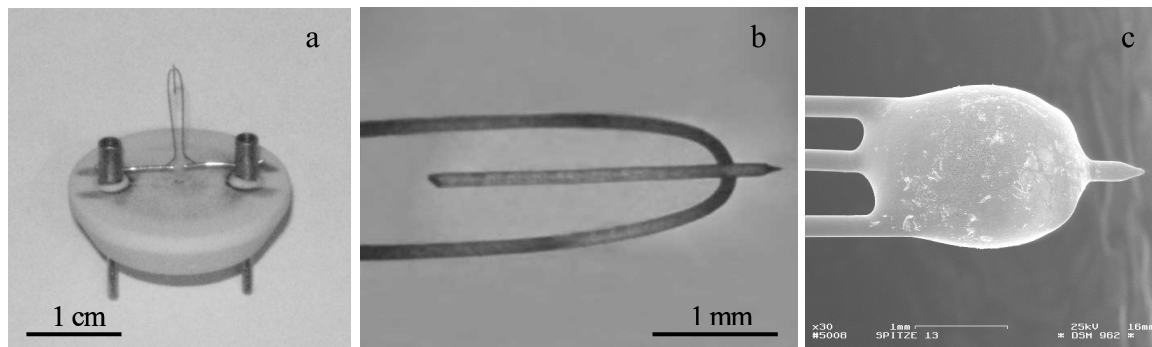
Fig. 5.5. Liquid metal/alloy ion source used on IMSA-100 FIB system. (a) LMIS socket with filament, (b) apex of the filament with needle, (c) the filament filled with droplet of a liquid metal.

system is the commercial electron microscope ZRM 20 ("Carl Zeiss Jena"). For acceleration of ions instead of electrons a new ion-optical column with an electrostatic accelerating and focusing system was developed. The first FIB in this system was obtained in 1990. The principal scheme of the IMSA-100 is shown in Fig. 5.6. The most important part of the system is the liquid metal/alloy ion source (LMIS) which consists of a filament made from a 0.2 mm tungsten wire on a special ceramic socket (see Fig. 5.5a). The filament can be directly heated by a DC current up to about 1200 °C. On top of the filament a short tungsten needle is attached by point welding (Fig. 5.5b). The needle tip is fabricated by electrochemical etching in NaOH or KOH solution [102]. The typical radius of the emitter needle tip is about 3-10 μm. A small droplet of metal or alloy acting as reservoir is introduced onto the filament by hot wetting in vacuum. After a heat treatment the alloy covers the emitter surface with thin film (wetting) (Fig. 5.5c). The source material should have a high surface tension and a low vapor pressure at its melting point. A broad variety of metals and metallic alloys can be used as a material for LMIS. For the IMSA-100 operation mostly AuGe, AuGeSi, ErFeCrNi, CoNd alloys or pure Ga are taken as a LMIS. Once filled, the source can be exploited many hundreds of hours at the emission current of some μA [102]. The source operates at the acceleration potential which is usually 30-35 kV. During operation above a critical value of the electric field between the source and an extractor electrode the molten droplet forms a cone on top of the tungsten needle, the so called Tailor cone with a half angle of 49.3° and a very sharp and small protrusion under the influence of the extracting electric field (Fig. 5.7). This protrusion has a radius of about 10 nm, which corresponds to the geometrical size of the ion source. A LMIS is characterized by its brightness (current density per unit of solid angle) [103]
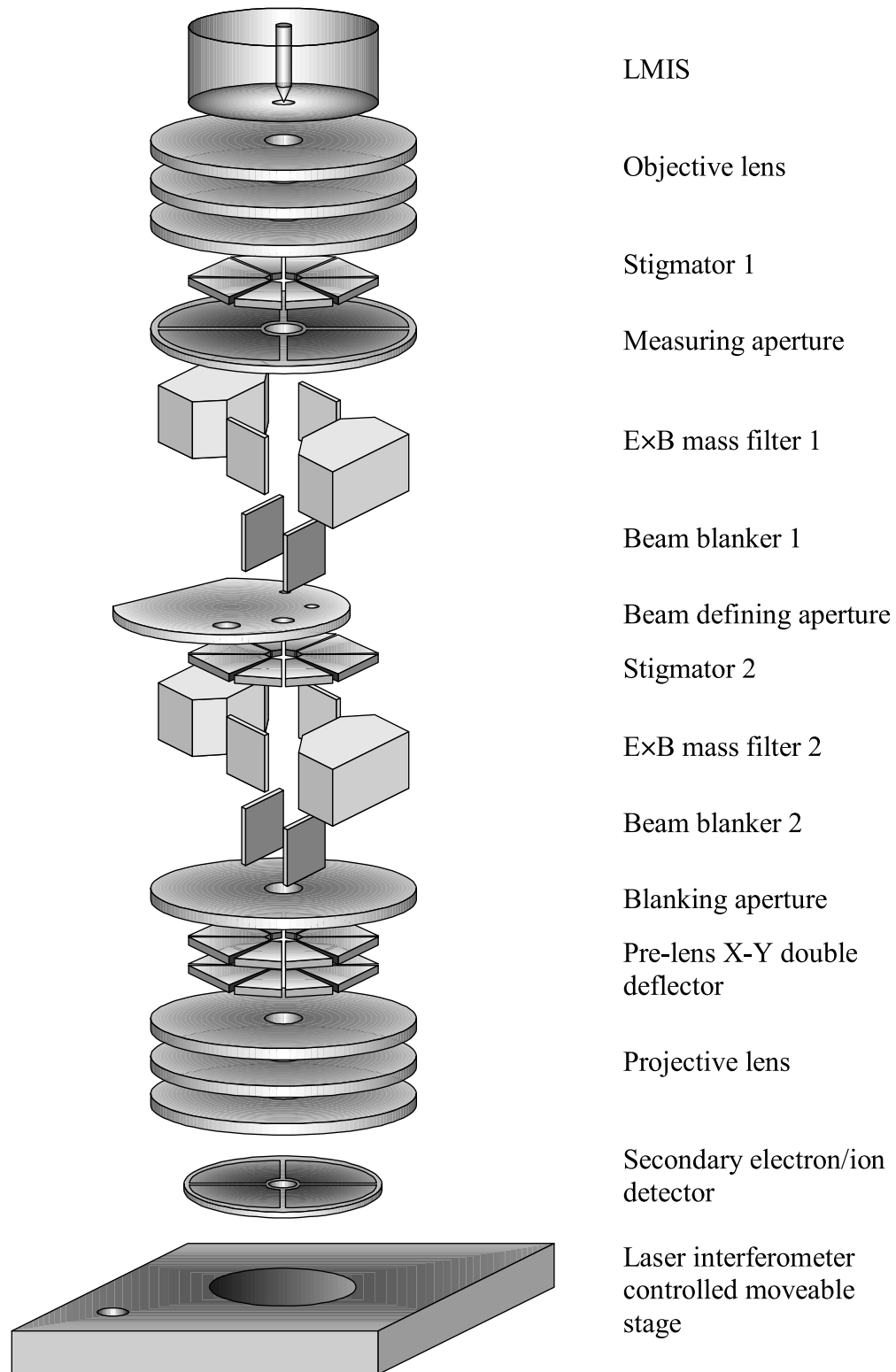
LMIS

Objective lens

Stigmator 1

Measuring aperture

E×B mass filter 1

Beam blanker 1

Beam defining aperture

Stigmator 2

E×B mass filter 2

Beam blanker 2

Blanking aperture

Pre-lens X-Y double deflector

Projective lens

Secondary electron/ion detector

Laser interferometer controlled moveable stage

Fig. 5.6. Principal scheme of IMSA-100 FIB column

$$B = \frac{I}{A \cdot \Omega},$$ where I is the ion current emitted by an area A of the source into a solid

angle Ω. A typical value for a LMIS is 10^6 A/cm^2·sr. The LMIS provides an initial jet of
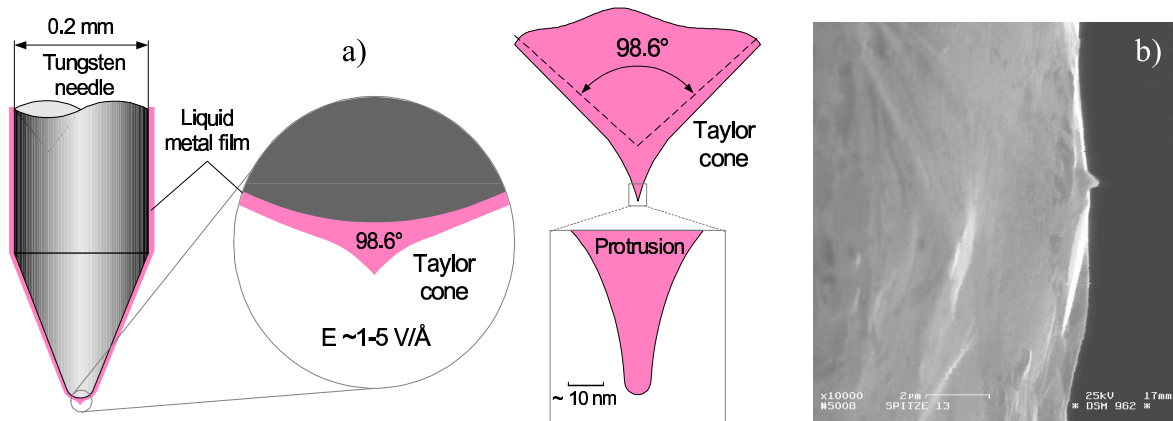
Fig. 5.7. Formation of the Taylor cone and a protrusion on a LMIS emitter tip (a) and a SEM image (b) of the protrusion [111].

ions and small particles of the liquid metal extracted from the source and accelerated up to the potential between the source and extracting electrode, which is usually in the range of 6-10 keV. The tip is located in the focal plane of the objective lens. The lens accelerates the ions up to the final energy equal to the source potential multiplied by the ion charge (in the case of singly charged ions the energy is 30-35 keV) and focuses the ions on the beam defining aperture locating below the first mass separator. There is a set of round apertures with diameters of 10 μm, 40 μm and 150 μm. The projective lens focuses the ions on a small spot on the surface of a target which is put in the focal plane of the lens. Between the objective and projective electrostatic lenses there are two E×B electromagnetic mass separating filters, two stigmators, electrodes of the blanking system, and X-Y scanning octupole double deflector. An important parameter of the LMIS is the energy spread of initial emitted ions. In Fig. 5.8 a typical energy distribution is shown. It is caused by ionization processes taking place near the tip of the ion source and amounts to 5..25 eV depending on the source material, temperature, charge state of the ions and emission current. Increasing this value leads to chromatic aberration of the FIB. The needed ions with mass M are filtered by the E×B mass separator with resolution $\dfrac{\Delta M}{M} = 70$. Fig. 5.9 shows a mass spectrum of $Au_{77}Ge_{14}Si_9$ LMIS which was used in this work. The spot diameter of the FIB is defined by the projection of the source tip on the focal plane, chromatic aberration due to energy spread of ions and spherical aberration of the electrostatic lenses [103,104]:

$$d_{FIB} = \sqrt{(K \cdot d_s)^2 + d_{ch}^2 + d_{sph}^2} \ ,$$
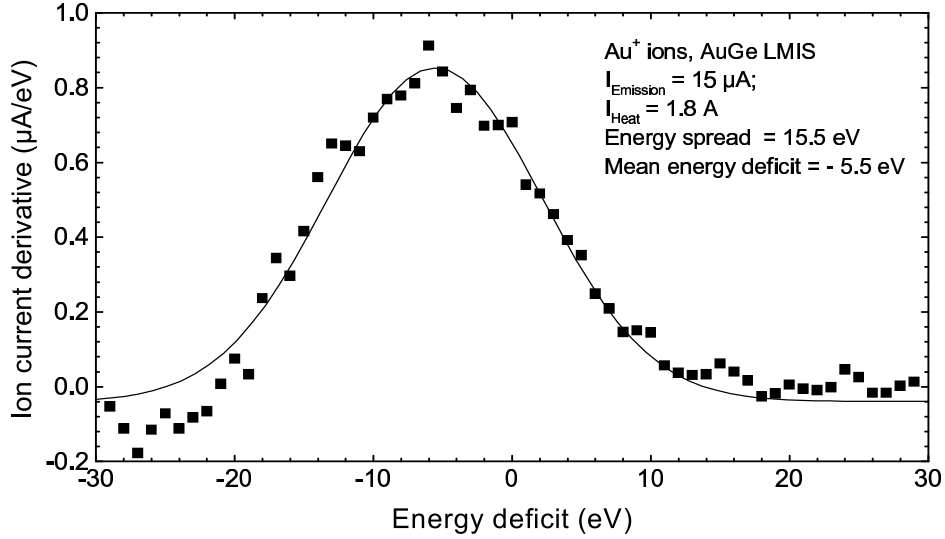(5.8)

Fig. 5.8. Energy distribution (proportional to current derivative, $\dfrac{dI}{dE}$) of Au^+ ions emitted by AuGe LMIS. The energy scale is relative to the acceleration energy.

where K is magnification of the ion optics defined by the parameters of the objective and projective lenses, d_s the virtual source size (usually about some nm), d_{ch} and d_{sph} are contributions of chromatic and spherical aberrations, respectively.

These values are defined as

$$d_{ch} = C_{ch}\left(\frac{\Delta E}{E}\right)\cdot\alpha \qquad d_{sph} = \frac{1}{2}C_{sph}\cdot\alpha^3 \qquad (5.9)$$

with chromatic C_{ch} and spherical C_{sph} coefficients of the ion optics of the column, α the acceptance half angle on the target plane, ΔE the energy spread and E the final energy of the ions on the target. In the IMSA-100 FIB system the presence of the E×B mass
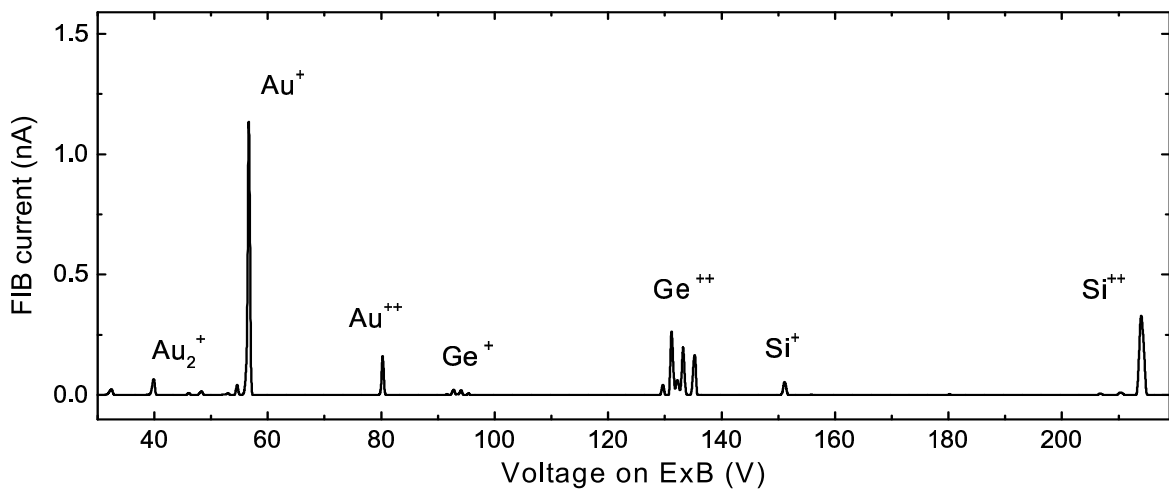

Fig. 5.9. Typical mass spectrum of the FIB emitted by the AuGeSi LMIS. The mass-to-charge ratio of the ions is a function of the E×B voltage V: $\dfrac{m}{q} = \dfrac{6.272 \cdot 10^5}{V^2}$
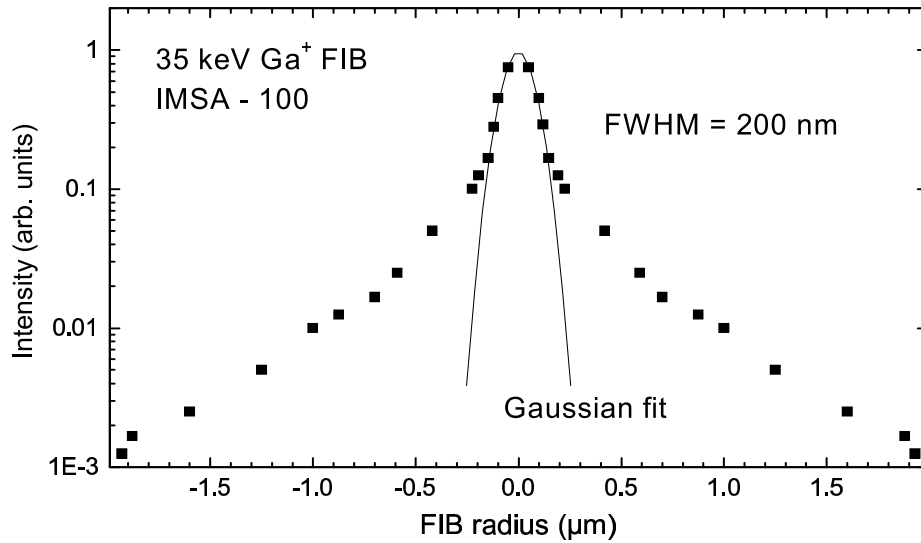
Fig. 5.10. Profile of 35 keV Ga$^+$ FIB measured on IMSA-100 [110]

separation filters additionally leads to astigmatism, i. e. the FIB cannot be focused to a round spot. Consequently, the spot has an asymmetric shape. This aberration can be corrected by an octupole stigmator. Under the best conditions a Au$^+$ FIB spot size of about 200 nm was obtained on the IMSA-100 (Fig. 5.10) at low beam current. By increasing the current the spot size increases drastically. At a maximum of the current of about 3-5 nA the value becomes more than 1 μm because of the large size of the beam defining aperture needed. In spite of relatively high emission current of the LMIS (1-100 μA) the final current of FIB is in the nA range. The electrostatic double-deflector scans the FIB over a 300×300 μm^2 area on the target surface. The ion beam column is evacuated down to 10^{-6} Pa by a turbo-molecular pump and two ion-getter pumps. The sample-holder is installed on the laser-interferometer controlled stage moving in the horizontal plane with accuracy of about 20 nm. The stage is introduced in a high-vacuum target chamber with a vacuum of about 10^{-5} Pa. The sample holder is introduced into the storage in the load-lock chamber and can be moved into the target chamber and put on the stage by a robotic hand.

5.3.2   The principal scheme of SIAM based on IMSA-100 FIB system

The scheme used for ion-acoustic imaging is illustrated in the Fig. 5.11. The main part of the SIAM is the IMSA-100 FIB system described above. Modulation of the FIB is provided by the blanker system which consists of two electrostatic plates of the beam blanker 2 (Fig. 5.6). A generator produces a periodical TTL signal for driving the voltage
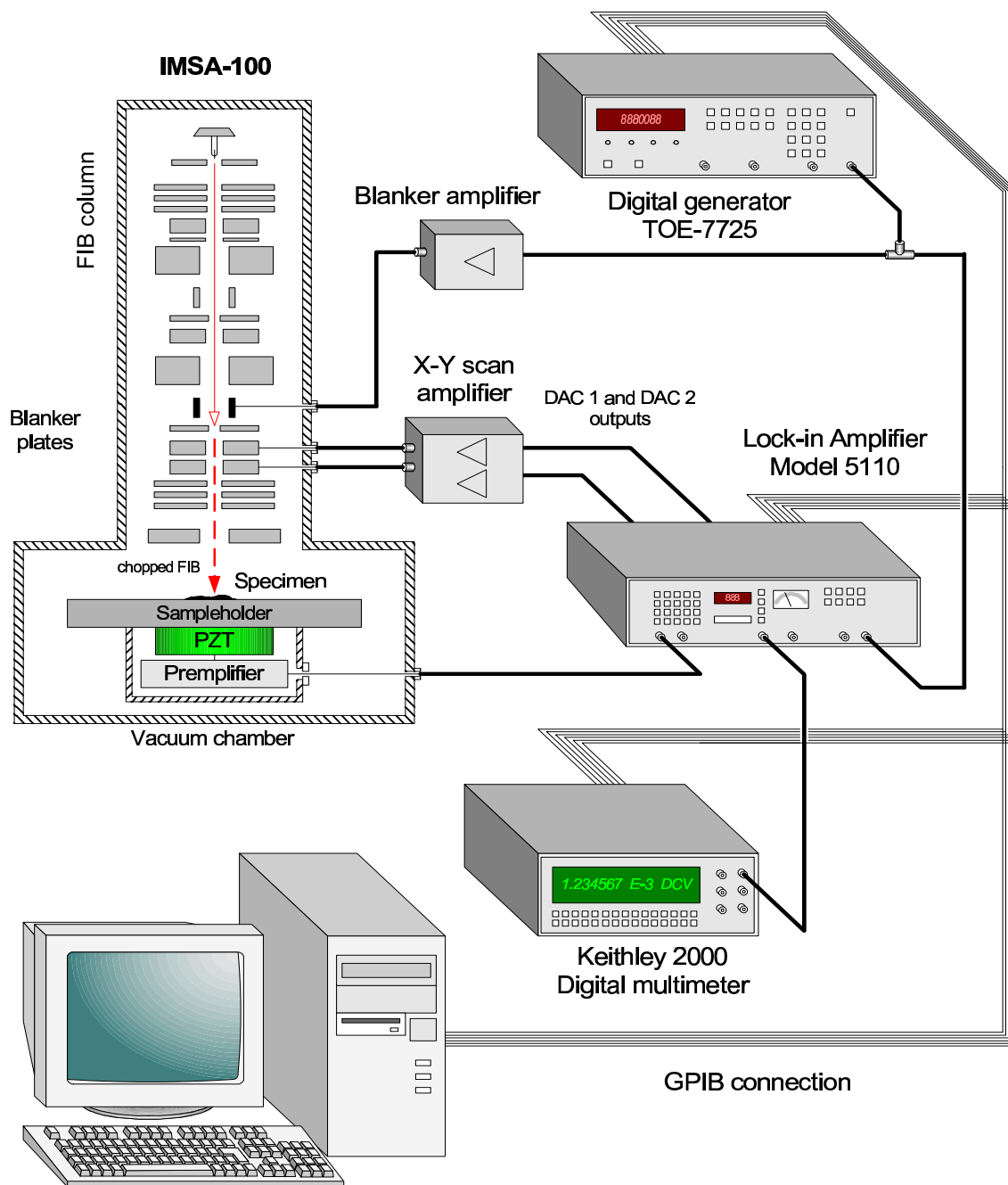
Fig. 5.11. SIAM based on IMA-100 FIB system. Experimental equipment

amplifier which forms the final voltage pulses of ±27 V on the plates. The maximum possible modulation frequency is defined by the length of the blanker plates of 40mm and the velocity of the used ions and can be estimated as:

$$f_{max} = \frac{1 - \dfrac{\tau_{FIB}}{T}}{\dfrac{L}{v} + \tau_{Blank}}, \qquad (5.10)$$
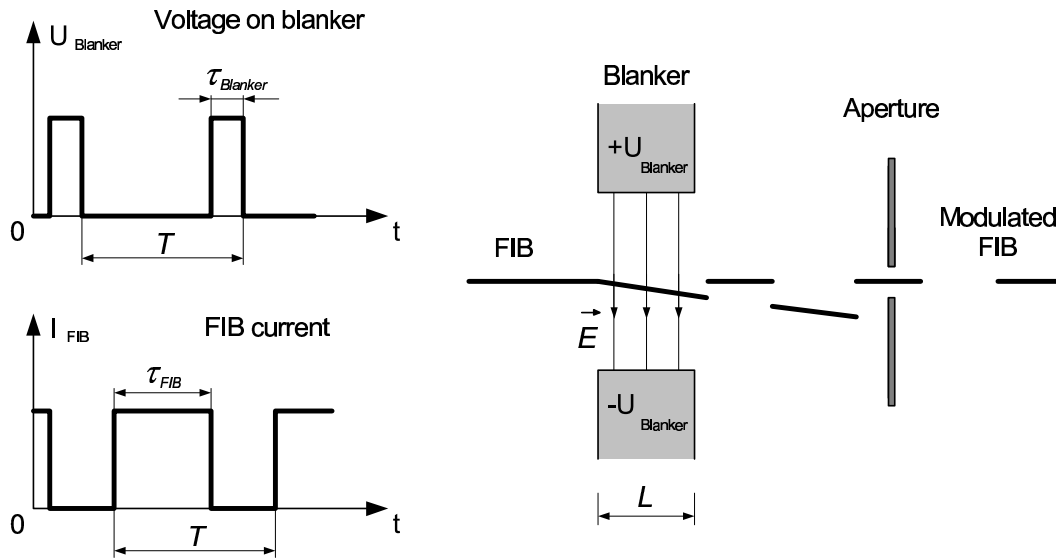
Fig. 5.12. Concept of the FIB blanking system.

where v is the axial velocity of the ions, L the blanker length, τ_{FIB} the duration of the FIB pulse, τ_{Blank} the duration of the voltage pulse on the blanker, and the term $\dfrac{\tau_{FIB}}{T}$ is determined by the FIB modulation duty factor (see Fig. 5.12). The maximum of the frequency is achieved for $\tau_{Blanker} \ll \dfrac{L}{v}$ and the frequency limit can be found as

$$f_{max} \approx \frac{v}{L}\left(1 - \frac{\tau_{FIB}}{T}\right).$$ Thus for a FIB modulated with a duty factor of 1:1 ($\dfrac{\tau_{FIB}}{T} = 0.5$,

$f_{max} = \dfrac{v}{2L}$) the 35 keV Au^+ beam ($v = 1.8 \cdot 10^5$ m/s) can be modulated with a maximum frequency of about 2 MHz. For a 35 keV Ga^+ beam ($v = 3.1 \cdot 10^5$ m/s) 4 MHz and for a 70 keV Si^{++} beam ($v = 6.9 \cdot 10^5$ m/s) nearly 8 MHz can be obtained. In the real case duration of the blanker voltage must be relatively long in order to move the FIB away from the blanking aperture. Also properties of the amplifier of the blanking signal gives some limitation due to the voltage switching time.

The periodically chopped ion beam focused on the target surface acts as a local probe and moves pixel by pixel over the sample area by means of an octupole double deflector system. The X-Y scanning signals with amplitude of ±12 V for the deflector are provided by two computer controlled digital-to-analog converters (DAC) with subsequent amplification by a scanning amplifier up to the final voltage of ±180 V. So the modulated FIB generates a thermal-acoustic wave in the sample emitted from the scanned area. The waves can be detected on the back side of the sample by a sensor. The signal from the

sensor is amplified by a low-noise integrated preamplifier. This signal is further processed by a lock-in amplifier for filtering at the resonance frequency of the piezoelectric sensor in order to reduce the noise component. The reference signal for the lock-in amplifier is the same as for the blanker. The filtered signal is digitized by a digital voltmeter connected with a computer via an IEEE488 GPIB. The measured signal-to-noise ratio before filtering was less than 1:50, the acoustic signal itself on the input of the preamplifier was in the range of 50-100 nV depending on the beam modulation frequency and examined specimen structure. The integrated noise was about 4 μVpp (peak-to-peak) and 9 μVpp for the two preamplifiers, respectively. The lock-in technique provides a suppression of the noise sufficient for further analysis and visualization of the signal on a personal computer. Scanning across a sample surface and measuring this changing of amplitude and phase of the acoustic signal can be used to obtain an image of the inspected area.

5.3.3 Sample holder

The investigated sample was installed on a sample holder which was introduced into the vacuum chamber via a load-lock system. The sample holder is a 10 mm thick plate of aluminum covered by a nickel film with length and width of 160 mm as shown in Fig. 5.13. From the bottom side four electric contacts are attached to enable electrical control and measurements. On this side there is also a set of grooves corresponding to three fixing points made from sapphire stones which are placed on the robotic hand and also on the stage to have stable and reproducible fixing of the sample-holder (Fig. 5.13b). Additionally, the holder contains two small holes for measurements of the beam current by a Faraday cup and for a nickel mesh used for adjustment of the ion optics of the column and calibration of the magnification. The sample was attached on the top of the sample
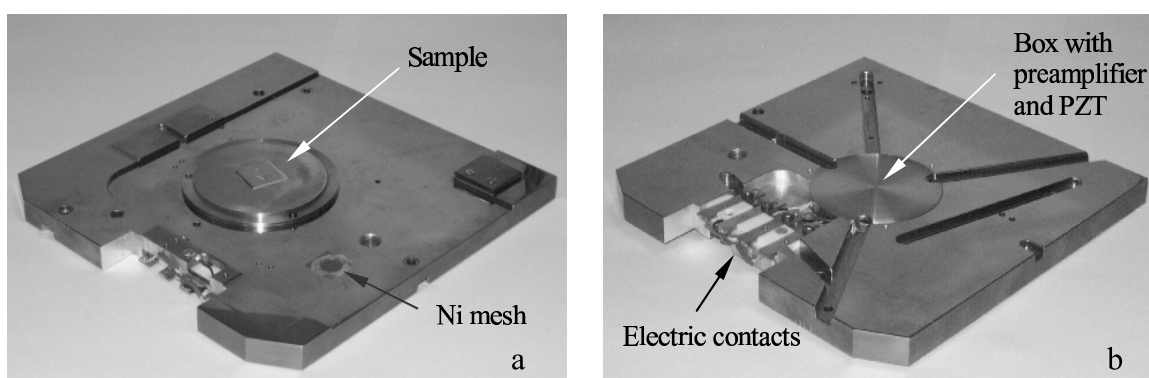

Fig. 5.13. Sample-holder top (a) and bottom (b) view.

holder on a small box containing the sensor
and the integrated preamplifier (Fig. 5.13a).
The cover has a round hole with a diameter
of 10 mm in the center which was closed by
a glued thin plate from brass, titanium,
copper or a silicon chip with thickness of 0.2
mm. The sensor was glued inside on the
cover (Fig. 5.14). The box provides a good
electrical screening of the detector and the
preamplifier to protect them from any
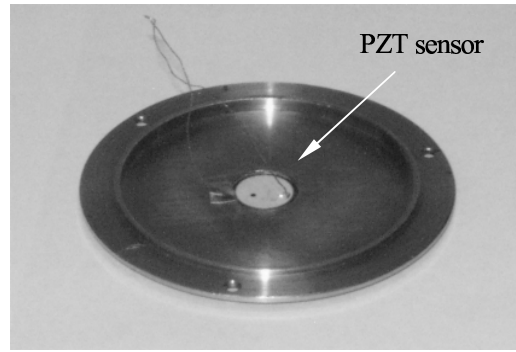influence of pulsed beam or electric fields in the vacuum chamber.

Fig. 5.14. Cover of the housing of the preamplifier with attached sensor. View from the bottom.

5.3.4 Acoustic sensor

Due to the low power of the FIB the elastic displacement of the surface of the samples is
extremely small. During bombardment by the modulated FIB with power of 100 μW at a
frequency of 100 kHz and a duty factor of 1:1 the energy per pulse is only 0.5 nJ and the
estimated surface motion of a 1 mm thick aluminum sample is in the range of 10^{-17}-10^{-16}m.
For the detection of such a tiny vibration a piezoceramic sensor was employed. The sensor
material is a PZT ceramic type APC-855 and APC-880 from American Piezo Ceramic
(Table 4.2). Different PZT discs with diameters of 5 mm, 10 mm and 20 mm and a
thickness of 0.5 mm, 1 mm and 6 mm were tested. The sensors have metallization on both
sides. The acoustic measurements were carried out at one of the resonance frequencies of a
sensor. Fig. 5.15. demonstrates a set of examples of frequency spectra obtained for a 10
mm disc of PZT APC-880 with a thickness of 0.5 mm (a, b) and for a 20 mm disc of the
same ceramic with a thickness of 6 mm (c, d). The transmission characteristics were
measured using a RC-filter scheme (see inset) with 100 kOhm resistor and the PZT instead
of the capacitance C. The obtained graphs show positive and negative peaks, so called
resonances and antiresonances. The mechanical resonance lies between them and can be
estimated as $\omega_0 = \dfrac{\omega_{antires} + \omega_{res}}{2}$. The quality factor of the PZT as oscillating system is
defined as $Q = \dfrac{\omega_0}{\omega_{antires} - \omega_{res}}$. The measured Q is between 500 and 800. The sensitivity of
detection at the eigenresonance of the PZT is Q times higher. The PZT detectors were
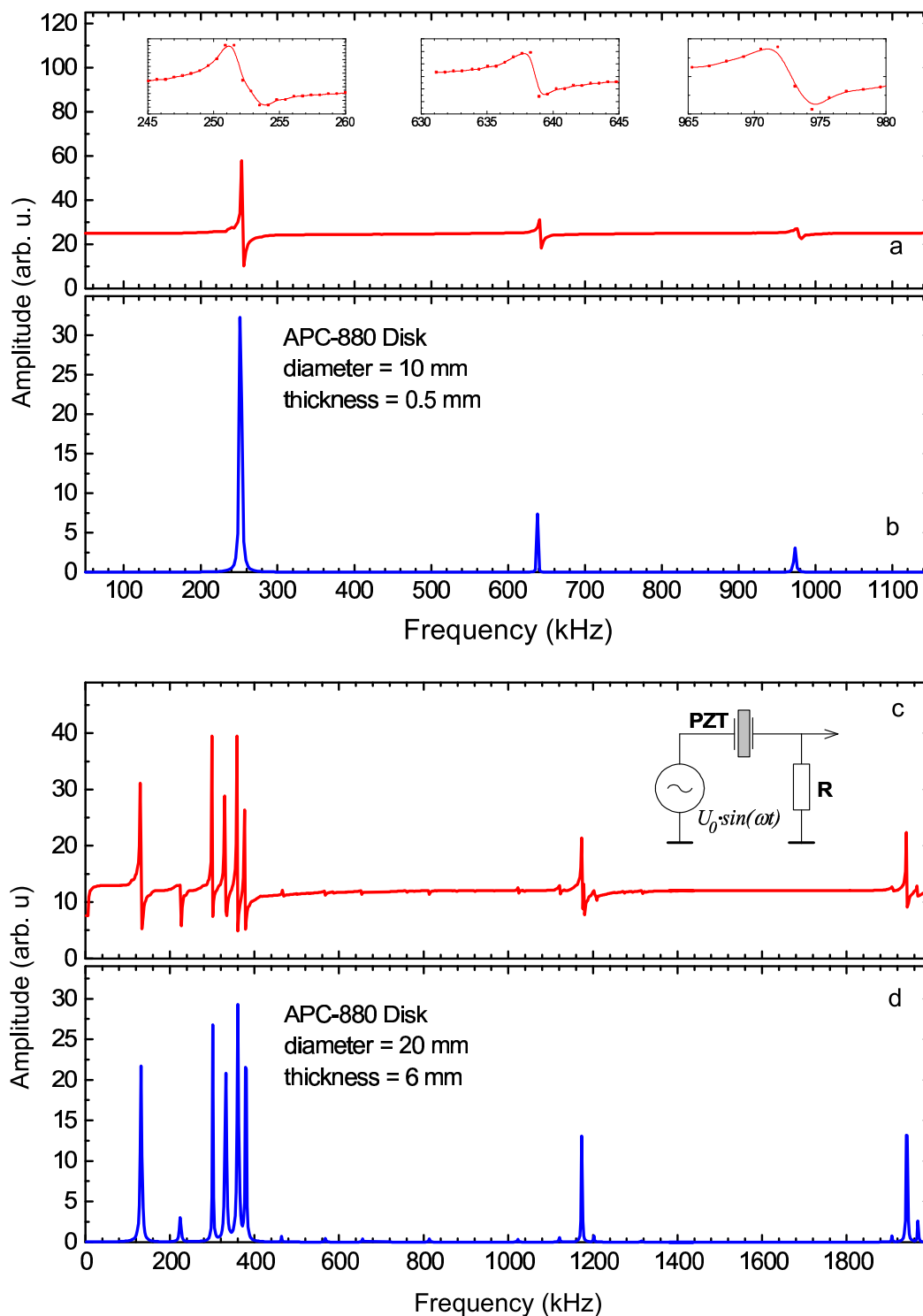
Fig. 5.15. Admittance as a function of frequency (a, c) and corresponding amplitude of mechanical oscillations (frequency spectra, b, d) of APC-880 PZT discs with a diameter of 10 mm and 20 mm and a thickness of 0.5 mm and 6 mm, respectively.

fixed on the back side of the box cover using two-component epoxy glue. After this they showed a lower quality factor due to damping, usually around 300, and a small shift of the resonance frequency. In Fig. 5.16 the measured transmission characteristic and amplitude

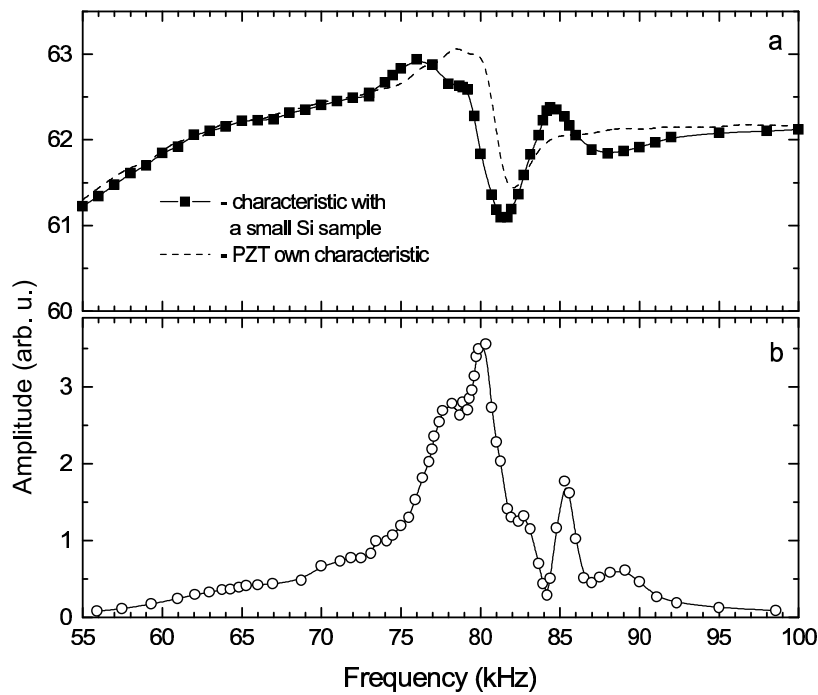**Fig. 5.16.** Admittance (a) and corresponding acoustic response (b) of 20 mm disc of PZT with thickness of 0.2 mm, obtained using a 35 keV Ga^+ FIB.

of the acoustic signal provided by a 20 mm disc of APC-855 PZT with a thickness of 0.2 mm is shown as a function of the FIB modulation frequency, varied around the resonance of 85 kHz.

5.3.5   Signal processing and visualization

5.3.5.1   Signal preamplifier

The electric signal from the sensor during operation of the modulated FIB is amplified by a preamplifier placed close to the PZT disc in the same metallic box in order to shorten the length of the wires, to reduce the parasitic capacitance and to screen electromagnetic influences. Two preamplifiers with different transmission characteristics and amplification factors were built and tested. Both were designed using the high-frequency low-noise operational amplifiers AD797AR from "Analog Devices". The first images were obtained at FIB modulation frequencies lower than 100 kHz. For this purpose a preamplifier with amplification of about 50,000 and a −3dB frequency band from 50 to 120 kHz was used. In order to work at higher frequencies the other preamplifier for frequencies from 100 kHz to
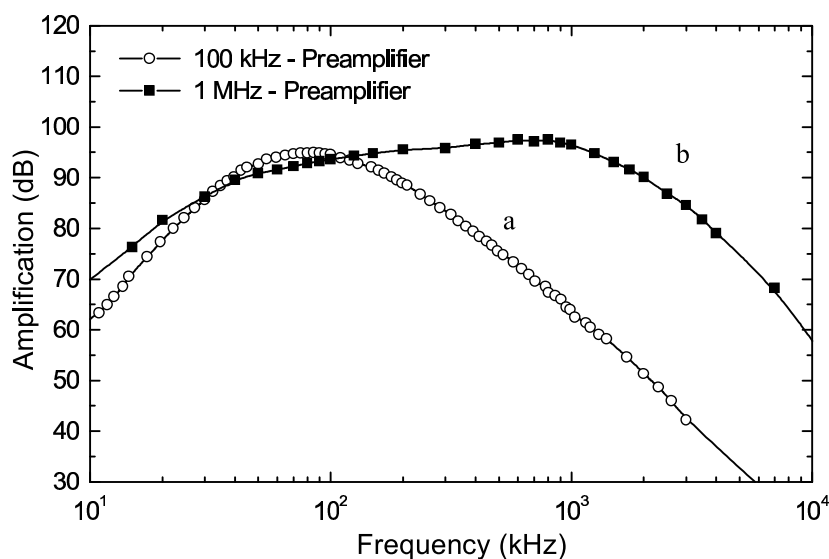
Fig. 5.17. Frequency characteristics of the preamplifiers used for amplification of acoustic signal in the frequency range: (a) 50-120 kHz, (b)100-1500 kHz.

1.5 MHz was applied. In Fig. 5.17 the amplification as a function of frequency is shown for both devices.

5.3.5.2 Filtering process

For further processing of the signal a lock-in technique was employed. At the beginning a device "Model 5110" ("*EG&G* Princeton Applied Research") was used. This lock-in amplifier can only operate up to a signal frequency of 100 kHz, but has amplitude and phase outputs. Supplementary it has two digital-to-analog converters (DAC) and a GPIB card for connection with a computer, which were further used for driving the scanning system and visualization. For frequencies higher than 100 kHz an in-house developed lock-in amplifier was used. It is able to filter the signal up to frequencies of 5 MHz but the output is a mixture of amplitude and phase signals. To improve the filtering by the lock-in technique it is necessary to set the bandwidth of the filter as narrow as possible. But this causes a limitation: the bandwidth must be wide enough to transmit the signal. The signal spectra can be compressed by decreasing of the FIB scanning velocity (Fig. 5.18.), so the filter bandwidth could be made much narrower. The spectral bandwidth of the signal is proportional to the scanning velocity or $1/T$ where T is the time per pixel: $\Delta f \sim \dfrac{1}{T}$.

Lowering of the velocity does not change the amplitude of the acoustic signal, $S_1 = S_2$ and
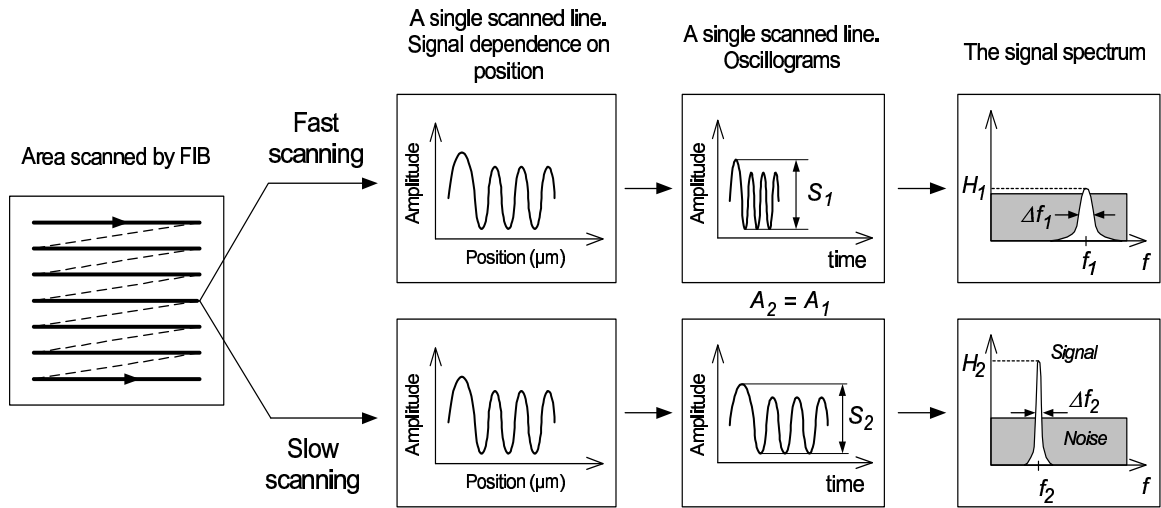
Fig. 5.18. Compression of the signal spectrum by decreasing of scan velocity of the FIB.

$H_1 \cdot \Delta f_1 \approx H_2 \cdot \Delta f_2$. But the noise N can be reduced with setting a narrower bandwidth Δf of the filter:

$$N = \sqrt{\int_{f_{min}}^{f_{max}} u^2_{\;noise} \cdot df} \approx \sqrt{u^2_{\;noise} \cdot \Delta f} \; . \tag{5.11}$$

The value u_{noise} is the spectral density of the voltage noise which is nearly constant at frequencies higher than 10 kHz for the AD797 type amplifier. In other words this means that signal-to-noise ratio $\dfrac{S}{N}$ can be improved by increasing the imaging time T_{Scan} as:

$$\frac{S}{N} \sim \sqrt{T_{Scan}} \tag{5.12}$$

With increasing the modulation frequency f the energy of a single FIB pulse E drops down proportional to the pulse duration. This leads to a decrease of the amplitude of the acoustic signal S which is proportional to the single pulse energy E:

$$S \sim E \sim P \cdot \tau \quad \text{otherwise} \quad S \sim \frac{1}{f} \quad \text{and} \quad \frac{S}{N} \sim \frac{1}{f}, \tag{5.13}$$

where P is the FIB power, τ is the beam pulse duration. In order to obtain the same quality of imaging at a higher frequency it is necessary to increase the scanning time as well as to make the filter bandwidth narrower. At modulation frequencies higher than 500 kHz the signal-to-noise ratio becomes very low and the imaging process needs a very long time, so the stability of the FIB current begins to play an important role. Usually the FIB can operate with sufficiently constant current during 4-5 hours. This time additionally limits the modulation frequency of the FIB which can be used for imaging.

The filtered signals from the lock-in-amplifier are digitized by a KEITHLEY 2000 digital multimeter and sent to a PC via a GBIP connection and converted to bitmap-graphic files.

5.3.6 Influence of noise

Because of the very weak acoustic signal it is important to decrease the noise level and suppress all possible noise sources. The noise limits the sensitivity of the sensor. There are four main types of noise sources here – the sensor itself, the electronics, the mechanical vibrations of the stage on which the sample-holder is mounted and fluctuations of the FIB power due to instability of the ion emission process.

5.3.6.1 PZT internal noise

The PZT sensor itself is also a source of noise. There are a lot of processes contributing to the noise, such as material dielectric loss noise, DC-leakage noise, Brownian motion noise, and thermal noise. The first is the most important. The spectral density of the dielectric loss noise is given as [105]:

$$u_{D-Loss} = \sqrt{4k_B T \frac{\tan \delta}{C \omega}}, \tag{5.14}$$

where $\tan \delta$ is the dielectric loss tangent, T is the temperature of PZT, k_B is the Boltzmann constant, ω is the angular frequency, and C is the electric capacitance of the sensor.

The DC-leakage noise is given by [106]:

$$u_{DC-Leak} = \sqrt{4k_B T \sigma \frac{L}{AC^2 \omega^2}}, \tag{5.15}$$

where A and L are the area and thickness of the sensor, respectively, and σ is the volume conductivity.

The Brownian thermal noise becomes significant near the resonance frequencies of the sensor. The Brownian motion of the solid atoms leads to an additional noise component arising due to the force with a spectral density of [107-109]:

$$F_B = \sqrt{4k_B TD}, \tag{5.16}$$

where D means the damping coefficient of the sensor. It can be expressed using the elastic modulus Y_E, the resonance frequency ω_0 and the quality factor Q of the sensor:

$$D = \frac{Y_E S}{L Q \omega_0} . \tag{5.17}$$

The spectral density of the Brownian thermal voltage noise on the electrodes of a PZT slab corresponding to n-th resonance frequency ω_n can be estimated as:

$$u_{nB} \approx \frac{4L}{\pi(2n+1)d_{33}} \cdot \sqrt{\frac{k_B T \omega_n \rho L k_P}{S Q_n \left[\left(1 - \frac{\omega^2}{\omega_n^2}\right)^2 + \frac{\omega^2}{\omega_n^2 Q_n^2} \right]}}, \tag{5.18}$$

here d_{33} is the piezoelectric charge constant and k_P is the electromechanical coupling factor for a disc which can be estimated at high frequencies as:

$$k_P = \sqrt{2.51 \cdot \frac{\omega_{antires} - \omega_{res}}{\omega_{antires}} - \left(\frac{\omega_{antires} - \omega_{res}}{\omega_{antires}}\right)^2} . \tag{5.19}$$

This factor indicates the effectiveness with which a piezoelectric material converts electrical energy into mechanical energy, or vice versa. The total noise integrated over the frequency bandwidth can be expressed by the following equation:

$$u_{total} = \sqrt{\int_{f\min}^{f\max} \left(u_{D-Loss}^2 + u_{DC-Leak}^2 + \sum_n u_{nB}^2\right) df} . \tag{5.20}$$

Fig. 5.19 illustrates the estimated noise spectral densities for a 10 mm APC-880 PZT disc. A comparison of the integrated noise for different PZT disks are shown in Table 5.1. The
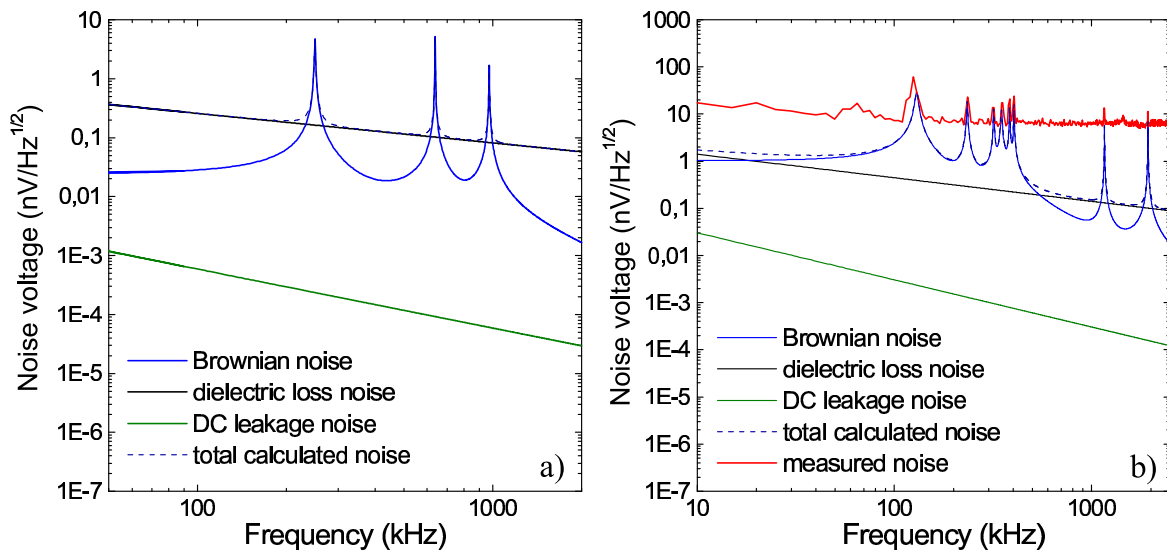

Fig. 5.19. The calculated spectral densities of noise for a 0.5 mm thick APC-880 PZT sensor with a diameter of 10 mm (a) and noise densities calculated and measured for a 6 mm thick APC-880 PZT disk with a diameter of 20 mm (b). This measurement was carried out using the preamplifier based on NE5539 operational amplifier with own noise of about 4 nVrms/Hz$^{1/2}$.

Table 5.1 ***Estimated noise contributions of the acoustic PZT sensors in the input of the preamplifiers***

Frequency band	50 − 120 kHz				100 − 1500 kHz			
Transducer type	APC-880 ⌀ 20mm t= 0.2mm	APC-880 ⌀ 20mm t= 6mm	APC-880 ⌀ 10mm t= 0.5mm	APC-880 ⌀ 5mm t= 1mm	APC-880 ⌀ 20mm t= 0.2mm	APC-880 ⌀ 20mm t= 6mm	APC-880 ⌀ 10mm t= 0.5mm	APC-880 ⌀ 5mm t= 1mm
Dielectric loss noise (nVrms)	320	130	77	215	220	230	130	380
Dielectric leakage noise (nVrms)	0.002	1	0.2	5	0.001	1	0.2	4
Brownian noise (nVrms)	26	3300	8	130	2	7400	280	580
Total noise (nVrms)	320	3300	80	250	220	7400	310	700

estimated total noise of the thin sensors is in the range of some hundreds of nanovolts, so they have a much lower contribution than that of the electronics, but near their resonance frequency PZT sensors show higher spectral density of noise caused by the Brownian noise component. Also the noise level of a PZT device depends on its shape and size and the mechanical properties. The signal-to-noise ratio at the resonance can be improved by increasing the sensor area and decreasing its thickness and operation temperature. Therefore only two thin PZT discs with a diameter of 10 and 20 mm and a thickness of 0.5 and 0.2 mm were found as good enough acoustic sensors. Knowing this, also an attempt to perform ultrasonic imaging using the 6 mm thick disc with a diameter of 20 mm was made but as expected it was unsuccessful because of very low signal-to-noise ratio.

5.3.6.2 Noise of electronics

The main noise contribution comes from the input cascade of the preamplifier which is added to the signal and also further amplified. It can be reduced by employing ultra low-noise operational amplifiers. The used operational amplifier AD797 has a typical input voltage noise of about 0.9 nVrms/Hz$^{1/2}$. This is one of the best available high frequency low-noise devices. This value corresponds to a thermal noise of a 50 Ohm resistor. The measured total integrated output noise of the first preamplifier module is about 23 mV(rms) corresponding to 0.4 µV(rms) of input noise. This output noise increases up to 35

mV(rms) after connecting with the 20 mm disk PZT sensor with a thickness of 0.2 mm. That means the output noise contribution of the sensor is in the range of 26 mV(rms) corresponding to a total noise of 500 nV(rms) which is a little bit more than the calculated value of 320 nV(rms). The high-frequency amplifier has the total noise of about 70 mV(rms) corresponding to the input noise of about 1.5 μV(rms). It increases up to 110 mV(rms) by connecting of the 10 mm disk of PZT sensor with the noise contribution of the sensor of about 84 mV(rms) on the output and 1.2 μV(rms) in input of the preamplifier. The calculated noise for this transducer is 310 nV(rms) at the chosen frequency window.

Integrated over the frequency bandwidth the total noise is not as important as the spectral density because the signal is finally filtered by a lock-in amplifier acting as a band pass filter with a frequency bandwidth in the range of 0.1 to 10 Hz at the signal frequency of some hundreds of kilohertz. But especially at the resonance frequency where the sensitivity of the detector is higher, the spectral density of the Brownian thermal noise also has a resonant behavior and becomes higher than outside of the resonance.

5.3.6.3 Mechanical noise

To protect the FIB system from mechanical vibrations the vacuum chamber with the movable stage and the load-lock chamber are hung on four sets of damping springs. It has a resonance frequency around 1 Hz. A transmission function of such a vibration isolation system exhibits a noise suppression of up to 200 dB (10^{10} times) at frequencies exceeding 100 kHz. The seismic vibrations have their maximum at low frequencies and rapidly drop down with increasing frequency as $\dfrac{a}{f^2}\dfrac{\text{m}}{\sqrt{\text{Hz}}}$ (rms), where $a{\sim}10^{-5}$-10^{-9}. The strongest high-frequency vibration may be emitted by the turbo-molecular vacuum pump working in the kilohertz range. This noise can be suppressed by additional vibration isolation of the pump and also during final filtering by the lock-in technique.

5.3.6.4 Fluctuation of the FIB current and energy

Fast fluctuations of the ion beam power lead to equivalent fluctuation of the acoustic emission. The origin of the current noise are high-frequency hydrodynamic oscillations of the liquid metal droplet on the hot filament of the ion source as well as fluctuations of the
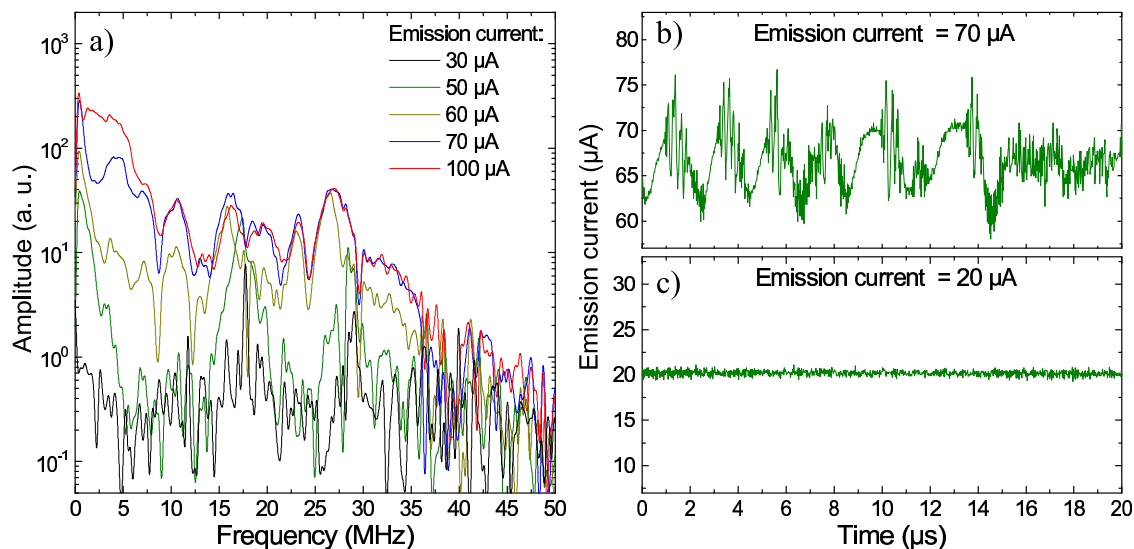
Fig. 5.20. Fluctuation of the ion emission process in AuGeSi LMIS at temperature of 730°C. Frequency spectra of the noise for different emission currents (a) and the noise oscillograms for 20 (b) and 100 µA (c).

extracting electric field near the emitter tip. Typical frequency spectra of such oscillations are shown in Fig. 5.20a. At a sufficiently high emission current not only ions but also droplets of liquid metal are ejected from the source. These primary droplets screen the source tip in the beginning of movement and therefore the effective electric field near the emission point is reduced for a short time. Then they can disintegrate into smaller ones, evaporate and ionize [54, 102]. The acoustic measurements were carried out at low emission currents of about 10-20 µA where the source operates very stable during a long time. At these currents the noise content was measured to be lower than 0.1 µA(rms), i. e. 0.7-1% (Fig. 5.20c). At higher emission currents the fluctuations becomes significant, for example at 100 µA the noise is about 5-6 µA(rms), i. e. 5-6% (Fig. 5.20b). The accelerated ions have also an energy distribution (Fig. 5.8). The reason for this energy spread is the emission process itself and the noise of the accelerating potential. Influence of the beam power fluctuation to the acoustic emission is negligibly small relative to the other noise sources. So the main contribution of noise comes from the preamplifier with additional small contents of noise of the PZT sensor and mechanical vibrations.

5.4 Measurements and imaging of microstructures using the SIAM

For measurements of the amplitude acoustic signal as a function of the FIB parameters the sensor with the lowest resonance frequency glued on a thin aluminum plate was taken.
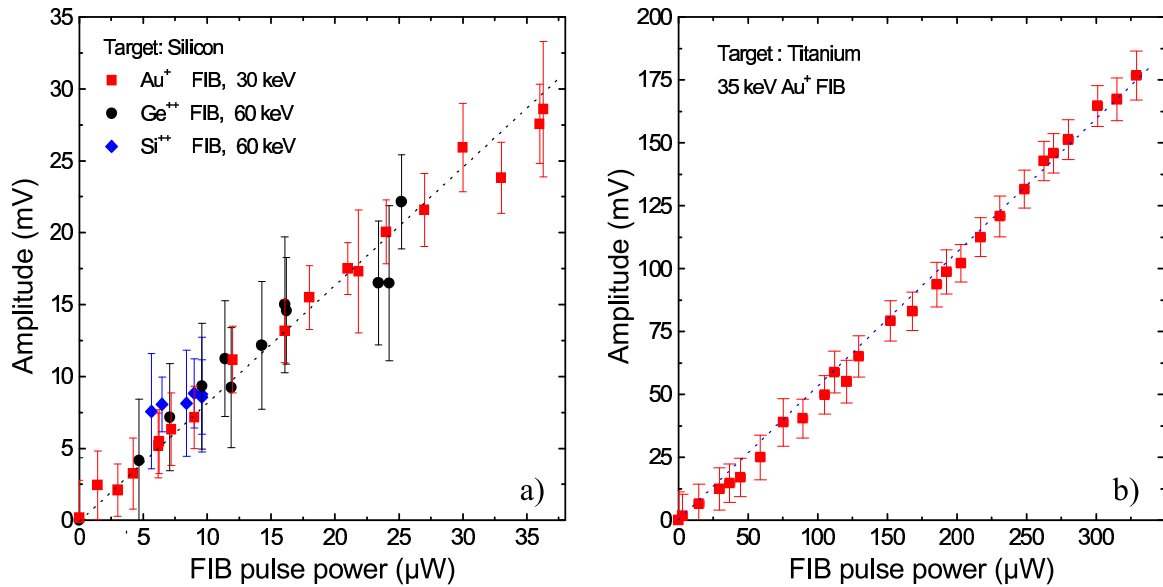
Fig. 5.21. Dependence of amplitude of the acoustic signal on power of the FIB pulse measured for a silicon (a) and titanium (b) targets using 30 keV Au^+ and 60 keV Si^{++} and Ge^{++} ions.

This frequency was about 85 kHz with the FIB pulse duration of about 5 µs. These measurements were carried out using an Au^+ FIB with the maximum available current up to 10 nA. Unfortunately the FIB spot size in this mode becomes at least 3-4 µm because of high ion emission current of the LMIS (~30-40 µA) and the use of the biggest beam defining aperture (150 µm). This fact is more important for imaging of microstructures but not for measuring of the signal dependence on the FIB parameters. The amplitude of the acoustic signal as a function of the FIB current is shown in Fig. 5.21 for silicon and
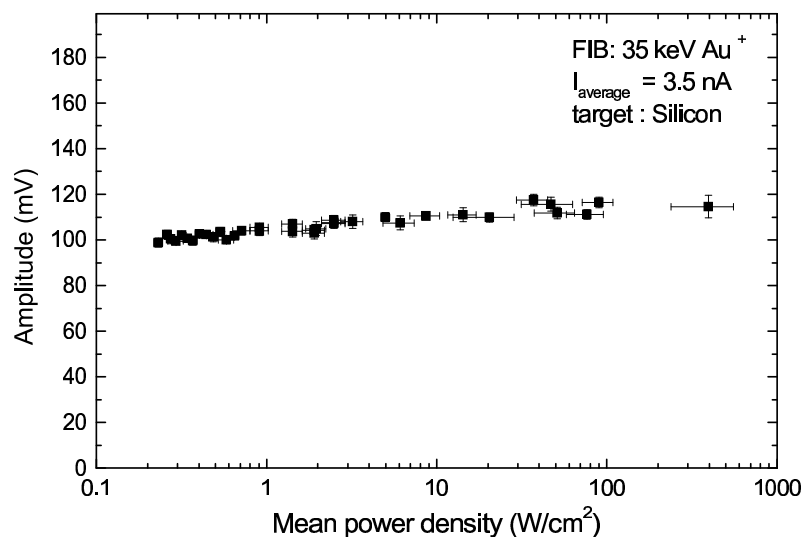

Fig. 5.22. Amplitude of the acoustic signal as a function of the FIB power density measured on a silicon target at constant total current of the 35 keV Au^+ FIB.
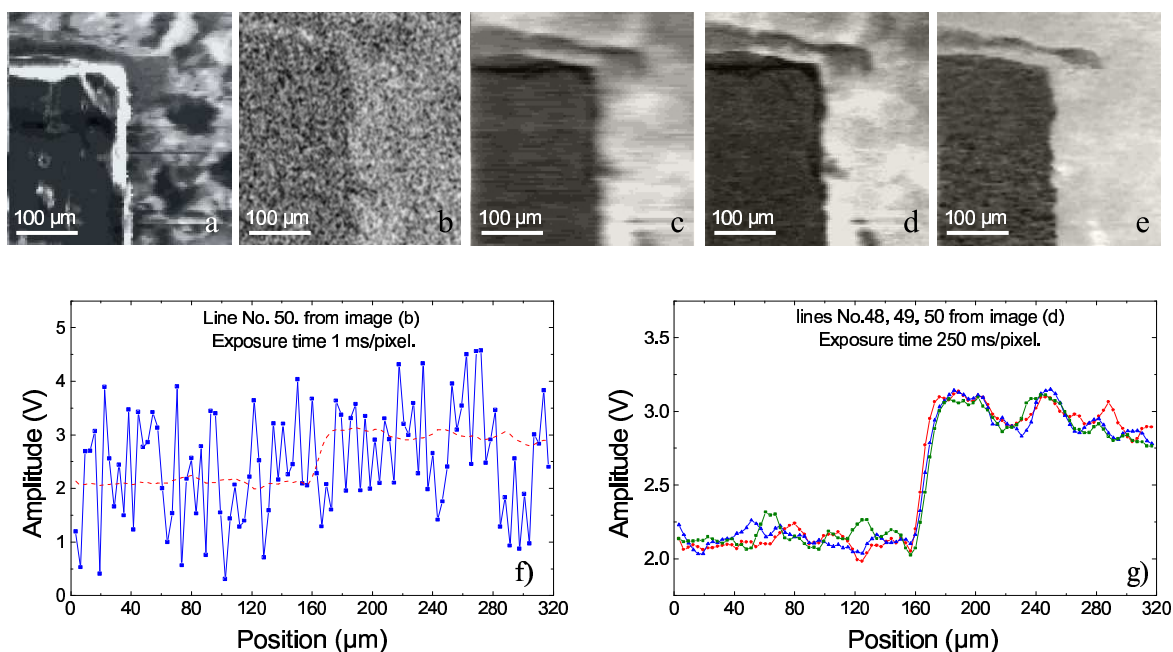
Fig. 5.23. A SE image (a) and acoustic amplitude images (b,c,d) and phase image (e) of a corner of a 200 μm thick silicon chip glued on a brass plate obtained using a 35 keV Au$^+$ FIB modulated at 85.5 kHz. At the bottom two sets of line scans extracted from the noisy image (b) (left) and the image (d) (right). The FIB pulse current is 2.6 nA. Acoustic imaging time is 1ms (b), 100ms (c) and 250 ms (d,e) per pixel. The image size is 300×300 pixels (b) and 100×100 pixels (c,d,e) corresponding to 320×320 μm^2. Dashed line in graph (f) is taken from (g) for comparison.

titanium samples. Some additional experimental points were obtained using 60 keV Ge^{++} and Si^{++} ions also emitted from the same AuGeSi LMIS. It is seen that the amplitude depends linearly on the FIB current. Also a weak dependence of the signal on the FIB spot size at a constant ion flux was found, i.e. the amplitude slightly increases upon increasing the FIB power density (shown in Fig. 5.22). This graph shows the dependence in the much broader range of the power density (0.1-1000 W/cm^2) than in Fig. 4.18, were there was no dependence of the amplitude on the power intensity found in the range of 100-1000 W/cm^2.

For the first imaging experiment a relatively rough structure, a 200 μm thick silicon chip glued on a brass plate was taken in order to get a high contrast. For gluing a special electrically conductive glue (RHC-140) containing silver powder was used. A 35 keV Ga$^+$ FIB with a current of about 3 nA was applied for imaging this structure. The beam spot size was nearly 1 μm. The imaging was performed by scanning the FIB over a corner of the chip. At first the internal scanning system of the IMSA-100 was used, but the longest available time was about 1 ms per pixel only. This was a limitation to the time constant of the low pass filter of the lock-in amplifier. The time constant cannot be longer than the

pixel time, otherwise the resolution in the scanning direction decreases due to the long relaxation time of the filter. In Fig. 5.23 a secondary electron (SE) image (a) and an acoustic amplitude image (b) of the structure are shown. The acoustic image size is 300×300 pixels corresponding to 320×320 μm^2 area. The time constant per pixel was 1 ms corresponding to 2 minutes for the whole imaging process. The FIB was modulated with a frequency of 85.5 kHz. Due to the short time constant of the filter the image (b) is very noisy. To reduce the noise the scanning must be slow enough in order to set the filter bandwidth narrower. For this purpose another scan system was built using two computer controlled digital-to-analog converters integrated in the lock-in amplifier, so the scanning time could be adjusted as long as needed. The same sample was imaged again with slower scanning velocity at the same FIB frequency. Fig. 5.23(c, d, e) presents the obtained acoustic images of the same structure based on the amplitude (c, d) and the phase (e) of the signal. In order to reduce the total time of the imaging the image size here was set to 100×100 pixels corresponding to the same area of 320×320 μm^2. The amplitude images were recorded with two scanning times of 100 ms per pixel (c) and 250 ms per pixel (d). That means that the total imaging time was about 15 and 40 minutes, respectively. The low pass filter of the lock-in amplifier had a time constant of 300 ms in both cases for a good filtering of the signal from noise. The lateral resolution of the fast scanned amplitude image (c) is lower than this of slow scanned amplitude image (d) because the pixel time is much shorter than relaxation time of the filter. The scanning time of the phase image was about 250 ms per pixel. The line scan graphs in this figure are extracted from the images (b) and (d) for comparison of the signal-to-noise ratio of the images. The left graph has the S/N ratio nearly 0.3 taken as the relation between the signal step value of about 1 V and the noise peak-to-peak value of about 3.5 V. The horizontal line scan of the same structure with exposition time of 250 ms has the ratio of about $1/0.15 \approx 6$. This means the ratio was improved nearly 20 times by increasing the imaging time. This is in reasonable agreement

with the calculated value of the S/N ratio Eq.(5.12) of $\dfrac{(S/N)_{Slow}}{(S/N)_{Fast}} = \dfrac{\sqrt{250 \text{ ms}}}{\sqrt{1 \text{ ms}}} \approx 16$. In the

images the corner of the silicon chip (left part of Fig. 5.23c-e), the elevation from the glue on the top of the picture and a part of the brass plate with a polycrystalline structure (of right side of the image) are visible. In the SE image the electrons give a very bright signal from the border of the silicon chip because of the high secondary electron emission at the edges, but the brightness of the flat surface is nearly the same as that of the brass substrate.
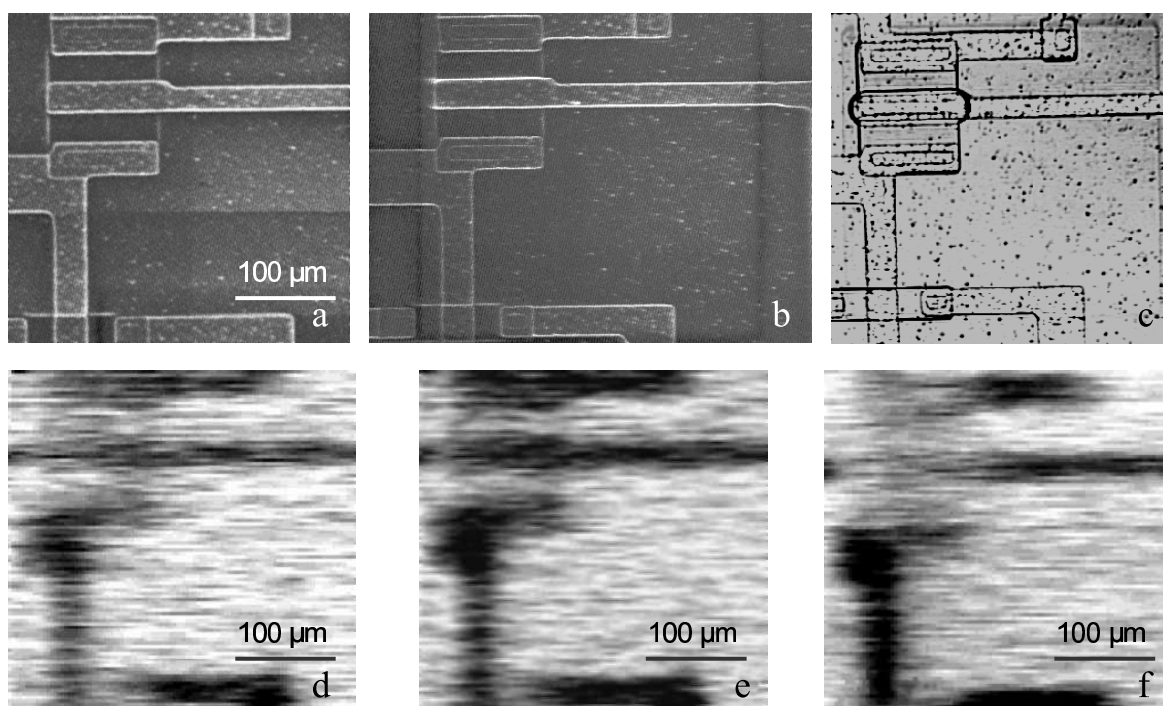
Fig. 5.24. Images of a microstructure containing a transistor: SE images before (a) and after (b) acoustic imaging, optical image (c) and acoustic amplitude (d, c) and phase (f) images of the transistor. The picture size is about 320×320 μm^2. 35keV Au$^+$ FIB modulation frequency is 79.5 kHz and pulse current is 2.7 nA. Imaging time: 250 ms and 400 ms per pixel for the amplitude images (d) and (e), respectively, and 900 ms per pixel for the phase image (f).

In the case of the acoustic signal its amplitude and phase show strong differences on silicon (dark gray area) and brass (bright) and the picture has a high contrast. High brightness of a pixel in an image corresponds to a higher amplitude of the signal at this place. The low signal from the silicon sample is the result of the acoustic dissipation and a phase shift due to the propagation of waves taking place in the material and at the interface between the chip and sample-holder filled by the glue. It is found that the amplitude gets nearly one order of magnitude lower when the wave propagates through the glue interface
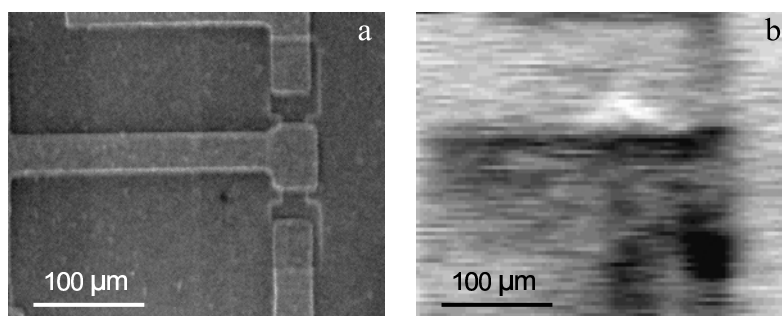

Fig. 5.25. SE (a) and acoustic amplitude (b) images of a transistor on a silicon chip. 35 keV Au$^+$ FIB modulated at 79.5 kHz with pulse current of about 2.6 nA. The picture size is 100×80 pixels. Imaging time is 400 ms per pixel.

because of dissipation and reflection.

The next set of images in Fig. 5.24 shows the SE images before (a) and after (b) acoustic imaging using FIB to study the surface erosion by the ion beam as well as optical (c), and acoustic amplitude (d - 250 ms/pixel, e – 400 ms/pixel) and phase (f) images of a transistor structure on a silicon chip. Also here in the SE image the brightness of the conductive paths is nearly similar to that of the silicon substrate, only the contours of the metallic wiring which have a high SE emission are white. The acoustic images give another view, metallic paths here are dark and the silicon substrate is bright. This implies more effective acoustic emission taking place in the silicon. In Fig. 5.25 another region of the same microstructure containing a transistor is demonstrated. In spite of the lower resolution, the acoustic images give more information and show some structure not observed in the SE image. The white spot near in the middle and the dark region in the bottom of Fig. 5.25b are not visible in the structure of Fig. 5.25a. An interpretation may be a long staying of the FIB near the center of the picture before starting the acoustic imaging. A signature from the standing FIB is visible near the center of the SE image as a small dark spot. These pictures were obtained by 35 keV Au^+ FIB modulated at a frequency of 79–80 kHz. In all the pictures of the silicon structures obtained at 80-85 kHz the lateral resolution was in the range of 15-20 μm.

In the beginning of the work a 0.2 mm thick PZT disk with diameter 20 mm was used for the sound detection. It has significant resonances at 2.6kHz, 43.5kHz, 79.5 kHz and 169 kHz but the lock-in amplifier model 5110 operates up to 100 kHz only. In order to go up in frequency a high-frequency lock-in amplifier was necessary. A self designed device as mentioned above and an additional commercial one (DYNATRAC 503) with a frequency limit of 10 MHz were used for further investigation. Fig. 5.26 presents a set of acoustic images of a silicon chip corner recorded using the x-y output of the device 5110
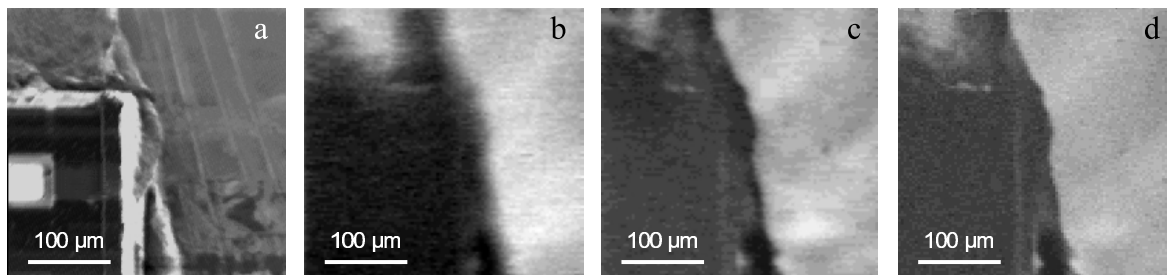

Fig. 5.26. Comparison of acoustic images of a silicon chip corner obtained at different modulation frequencies of 35 keV Au^+ FIB: SE image - (a), acoustic images at 43.5 kHz (b), 79.5 kHz (c) and 169 kHz (d).
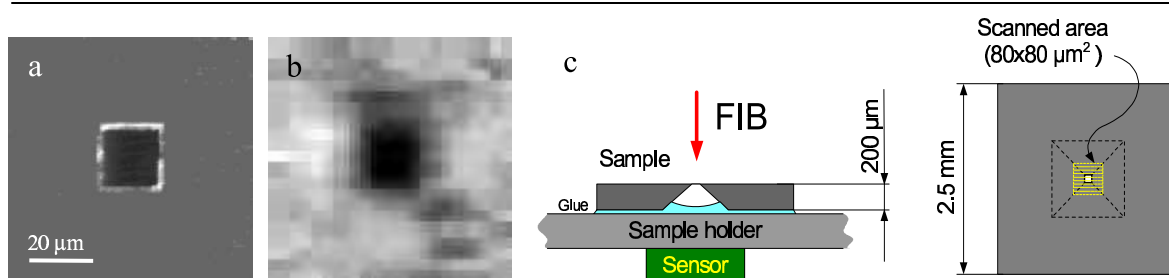
Fig. 5.27. SE (a) and acoustic (b) images of a pyramidal microstructure fabricated in a small silicon chip by anisotropic etching (c). The picture size is 80×80 μm^2, the central square hole has a size of 20 μm. 30 keV Au^+ FIB modulated at 254 kHz was used. The exposure time is 3 s per pixel.

and the self designed lock-in amplifier at frequencies 43.5 kHz, 79.5 kHz and 169 kHz for comparison of the lateral resolution. With increasing modulation frequency the resolution becomes better. The lowest resonance of this sensor at 2.6 kHz was not used because the very high thermal diffusion length in silicon leads to a low resolution in this case of about 100 μm by the maximum imaged area of about 400×400 μm^2 only.

In order to check the possibility of visualizing buried structures a small silicon chip with a pyramidal hollow in the center was chosen (Fig. 5.27). This microstructure was fabricated by anisotropic wet chemical etching of silicon [110]. In order to get a high signal the exposure time and the time constant of the filter were chosen to be 3 seconds and therefore, for the reduction of the total imaging time, the picture size was reduced to 20×20 pixels corresponding to 80×80 μm^2. The imaging took around 20 minutes. In this image (Fig. 5.27b) a cross-like structure with a highlighted center is visible. The signal from the central hollow shows the lowest amplitude (dark) because possibly in the pyramidal hollow was a thicker layer of glue which reduces the acoustic emission efficiency and has bad sound propagation properties. The maximal depth of the structure in this figure is about 30 μm, so a part around the central hole lies in the near-field region, which is about 10-12 μm deep for 254 kHz thermal acoustic waves in silicon. In the area where the material is thinner, the signal is higher as a result of higher temperature rise (the bright regions on all four sides the central square hole). The estimated resolution of this image is about 10-12 μm.

5.5   Lateral resolution of the SIAM based on IMSA-100 FIB system

The lateral resolution at different modulation frequencies was roughly estimated by measuring the width of the slope of the acoustic amplitude signal obtained during a single
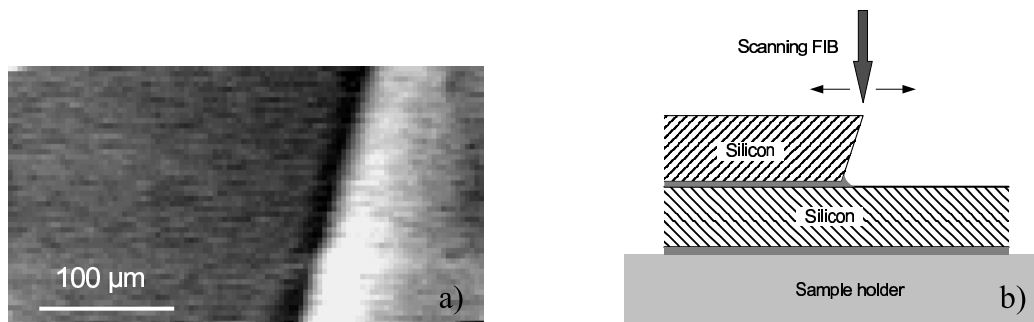
Fig. 5.28. An acoustic image (a) and a principle scheme (b) of the silicon sample used for measurements of the resolution. The image was taken at 270 kHz using Au^+ FIB.

line scan of the FIB across a border of a piece of a silicon wafer or glass plate glued on an identical base as well as from the images of the microstructures. To get a sharp border of the samples they were structured by cutting and checked under an optical microscope. The line-scan acoustic signals obtained at different modulation frequencies using a silicon sample are shown in Fig. 5.30. A set of scans containing about 20-30 lines was performed and analyzed for each frequency. Fig. 5.28 illustrates the scheme of the measurements on a silicon sample used for the determination of the resolution. As a value of the lateral resolution the mean value of the step width was taken. For this purpose the data points were fitted by an integral of Gaussian function (*erf*). The so estimated resolutions for silicon and glass samples are shown in Fig. 5.29. The lateral resolution significantly increases with frequency. This is also clearly illustrated by the images in Fig. 5.26. For
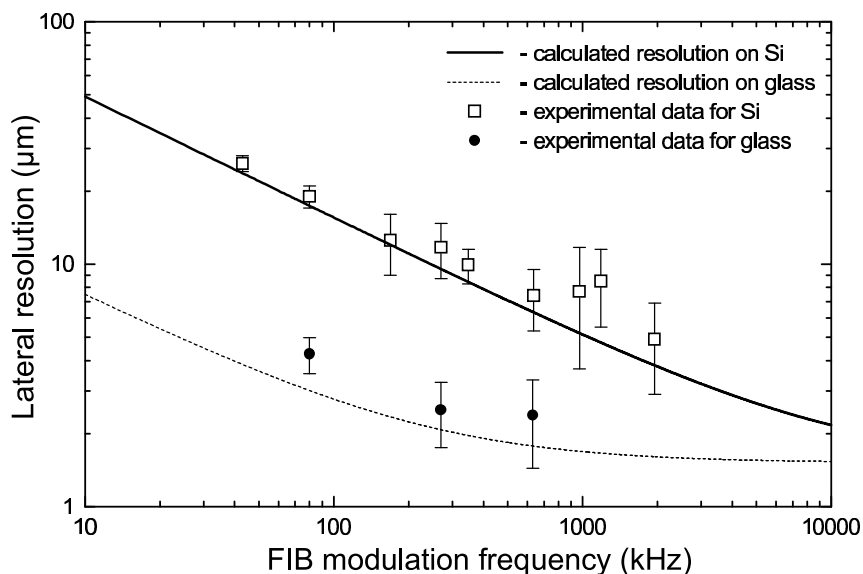
Fig. 5.29. Lateral resolution of the SIAM based on IMSA-100 FIB system measured on silicon and glass samples.
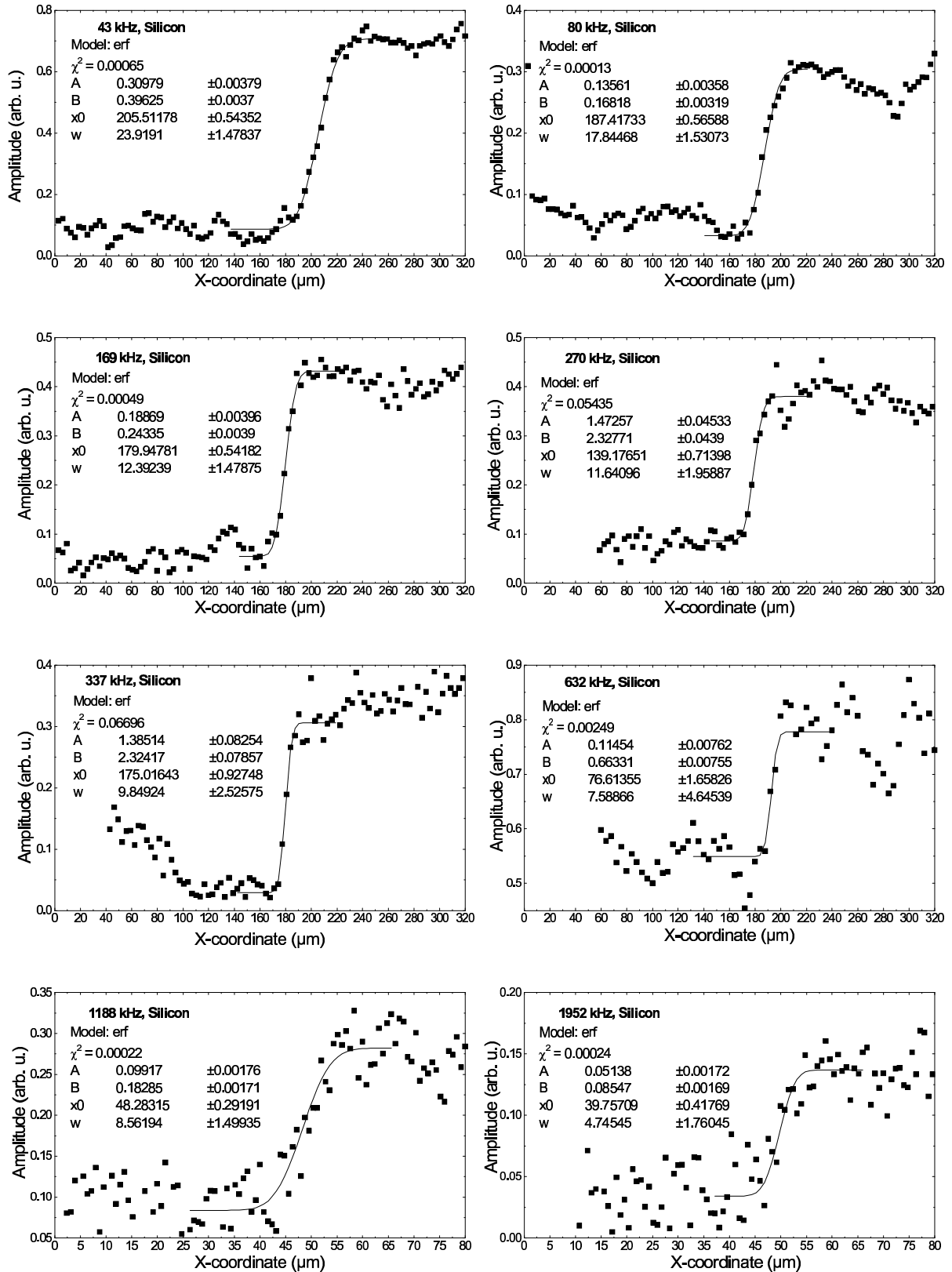
Fig. 5.30. A set acoustic amplitude signals obtained with 30 keV Au$^+$ FIB modulated at difference frequencies by scanning in horizontal direction across a silicon sample. The measured points are fitted by error an function (*erf*), i.e. integral of Gaussian:

$$F(s) = A \cdot erf\left(\frac{x-x0}{w}\sqrt{2}\right) + B = A\frac{2}{\sqrt{\pi}}\int_0^s e^{-\frac{2(x-x0)^2}{w^2}}\,dx + B\,.$$

comparison the dependence calculated using Eq. (3.24) and (5.5) with a FIB spot size of 1 μm are also shown. The resolution varies from 30 to 7 micrometers on silicon and from 10 to 3 μm on glass in the FIB frequency range from 40 kHz to 1 MHz. The chopping frequency itself has a limit of about 4-6 MHz. The main reason for this is the length of blanker electrodes in the ion-optical column of about 4 cm and the low velocities of the used heavy ions. The acoustic signal amplitude drops down drastically with increasing frequency which yields a lower beam energy per pulse and smaller signal-to-noise ratio. At a frequency above 350-400 kHz the signal is so small that the imaging process becomes impossible. Only several lines containing 40-50 pixels take some hours of beam operation time. In order to get a maximal signal output the FIB current may be varied from 3nA up to 10nA but this leads to enlargement of the spot size from 1 μm to about 5 μm and strong sputtering of a sample. Therefore the resolution of the SIAM cannot be further increased using the IMSA-100 FIB system.

5.6 Summary

In this part of the work the principal possibility of application of a periodically modulated FIB for scanning ion acoustic microscopy was demonstrated. The SIAM based on the IMSA-100 FIB system is able to provide acoustic imaging of microstructures with a resolution in the μm-range. Such a microscope has its own advantages and disadvantages. The SIAM is one of the modes of a FIB system which allows to provide nondestructive examination of investigated or produced samples. The FIB itself can be simultaneously used as a tool for cutting of the sample for further investigation and analyzing of a defect region. By increasing the modulation frequency a lateral resolution in the sub-micron range can be reached because the only limit are the spot size of about 100 nm and the energy dissipation volume diameter of about 30-40 nm for heavy ions in silicon which are smaller than in the case of SEAM. Unfortunately this is not a real nondestructive method. Because of the high current needed for imaging, the sample is strongly damaged as it is seen in Fig. 5.24(b, c). The FIB pulse energy is some orders of magnitude lower than that for a focused electron beam and therefore the image quality is lower. Due to the mass of ions they move much more slowly than electrons in SEAM, thus allowing only lower modulation frequencies. As a result high resolution cannot be reached with the present blanking system on IMSA-100. On the other hand the registration of the acoustic signal becomes more

difficult at a high modulation frequency due to reduction of energy per pulse followed by a decreasing of the amplitude of the acoustic wave. Therefore the present PZT sensor would have to be modified and also the noise must be reduced for better quality. For data acquisition a very low-noise high-frequency electronics is necessary.

6. Conclusion

The bulk ultrasound emission in a solid was investigated using a pulsed high energy ion beam focused on aluminum, copper, iron and silicon samples. Oxygen, silicon and gold ion beams were applied with the pulse duration of 0.5 - 4 μs and an energy of 1.5 - 10 MeV. Intensity of the detected acoustic waves shows a linear dependence on the energy of the incident ions, on the ion flux as well as on the pulse duration. No influence of the ion charge, ion mass and other possible mechanisms to the emission of acoustic waves was observed. Therefore as the main reason of this process in the used samples with a clean surface a local transient heating of the target during the irradiation was defined. The shape of the obtained acoustic signal is in a good qualitative agreement with the response calculated for an expected surface movement and a layered model of the piezoelectric sensor.

The ion acoustic effect was applied for a nondestructive material inspection using intensity modulated focused ion beam providing by the IMSA-100 FIB system with an accelerating potential of 30-35 kV. The achieved lateral resolution of this scanning ion acoustic microscope is in the micrometer range depending on the sample material and the beam modulation frequency. The resolution can be improved by increasing the frequency. The maximal modulation frequency which was obtained at IMSA-100 is about 2 MHz corresponding to lateral resolution of 4-5 μm on silicon. Further increasing the resolution needs higher modulation frequency which was not achievable on this equipment due to the geometry of the blanking system. On the other hand the intensity of the generated ultrasound becomes lower with increasing frequency, so the signal detection becomes more difficult under these conditions. Using this microscope, some images of integrated microstructures on a silicon chip were obtained using the lock-in technique for filtering of the signal from the noise and increasing of the total imaging time. The possibility to visualize near sub-surface structure was demonstrated. Due to the strong sputtering effect and the long time of irradiation the imaged structures were significantly damaged. Si^{2+}, Ge^{2+}, Ga^+ and Au^+ ions were used. All these ions are quite heavy and have high sputtering

coefficients. FIB of light elements like Li, B, or Be emitted from a LMIS can reduce the damaging process can make possible to increase the imaging time. Long-time imaging improves the quality of acoustic images, i. e. the signal-to-noise ratio is reduced with the square root from the pixel time, but leads to significant erosion of the imaged structure.

Appendix

A.   Elastic properties of a solid

The relative elongation of a fiber with initial length x_0 is described by the

$$\varepsilon = \frac{x - x_0}{x_0} \tag{A.1}$$

and is also called the Cauchy strain measure. Using a Taylor expansion the displacements of the fiber ends u_A and u_B are related as

$$u_B = u_A + \frac{\partial u_A}{\partial x} \cdot \Delta x \tag{A.2}$$

and the relative elongation

$$\varepsilon = \frac{u_A - u_B}{\Delta x} \; . \tag{A.3}$$

The process can be considered as time dependent and one has $\varepsilon = \varepsilon(x,t)$.

Considering the general treatment and taking into account all three spatial dimensions one can write the length of a small fiber as

$$dl = \sqrt{dx_i dx_i} \tag{A.4}$$

After deformation the length becomes

$$dl' = \sqrt{dx_i' dx_i'} \tag{A.5}$$

The displacement along the axis x_i is equal du_i and therefore

$$dx_i' = dx_i + du_i = dx_i + \frac{\partial u_i}{\partial x_k} dx_k \tag{A.6}$$

and for the length after deformation one has

$$dl' = \sqrt{dx_i dx_i + 2\frac{\partial u_i}{\partial x_k} dx_i dx_k + \frac{\partial u_i}{\partial x_k}\frac{\partial u_i}{\partial x_m} dx_m dx_k} \tag{A.7}$$

The increment in the square of the length is given by

$$dl'^2 - dl^2 = 2\frac{\partial u_i}{\partial x_k} dx_i dx_k + \frac{\partial u_i}{\partial x_k}\frac{\partial u_i}{\partial x_m} dx_m dx_k \tag{A.8}$$

The symmetry of the dummy indices in the first term of the right hand side of the equation suggests that

$$2 \frac{\partial u_i}{\partial x_k} dx_i dx_k = \frac{\partial u_i}{\partial x_k} dx_i dx_k + \frac{\partial u_k}{\partial x_i} dx_k dx_i \ . \tag{A.9}$$

So the increment can be expressed as

$$dl'^2 - dl^2 = \frac{\partial u_i}{\partial x_k} dx_i dx_k + \frac{\partial u_k}{\partial x_i} dx_k dx_i + \frac{\partial u_m}{\partial x_k} \frac{\partial u_m}{\partial x_i} dx_i dx_k = 2u_{ik} dx_i dx_k \tag{A.10}$$

where the value of u_{ik} are known as the deformation tensor and given by

$$u_{ik} = \frac{1}{2} \left(\frac{\partial u_i}{\partial x_k} + \frac{\partial u_k}{\partial x_i} + \frac{\partial u_m}{\partial x_k} \frac{\partial u_m}{\partial x_i} \right), \quad i, k, m = 1, 2, 3 . \tag{A.11}$$

The symmetry of indices i and k means that $e_{ik} = e_{ki}$ and gives a possibility of diagonalizing of the tensor. The six independent components of the tensor enable one to determine the relative elongation along any direction and change of angles during the deformation. The square term in this expression can be neglected for small deformations. In this case one has a linear tensor of deformations, given by

$$u_{ik} = u_{ki} = \frac{1}{2} \left(\frac{\partial u_i}{\partial x_k} + \frac{\partial u_k}{\partial x_i} \right). \tag{A.12}$$

Motions of a body under applied forces are described using a concept of stresses. If a small surface area, ΔA, with a unit normal vector $\vec{n}$ is subjected to the resultant vector of forces $\Delta \vec{F}$ a stress vector is defined as:

$$\vec{\sigma} = \lim_{\Delta S \to 0} \frac{\Delta F}{\Delta A} = \frac{d\vec{F}}{dA} , \tag{A.13}$$

with the same direction as the vector of force. This stress depends on orientation $\vec{n}$:

$$\sigma_m = \sigma_{mk} n_k \tag{A.14}$$

where n_k and σ_m are projections of the stress vector and normal vector, respectively. The values σ_{mk} are known as components of the stress tensor. This tensor is symmetric like the tensor of deformations, u_{ij} , and thus the tensor σ_{mk} has only six independent components. The internal stress within a solid can be defined in a similar manner.

According to Hooke's law the stress linearly depends on strain:

$$\sigma_{ij} = c_{ijkl} u_{kl} \tag{A.15}$$

where c_{ijkl} is the tensor of elastic constants. Due to symmetry of the tensors ε_{ij} and σ_{ij} a permutation of indices, i and j, k and l, would have no effect, and, so
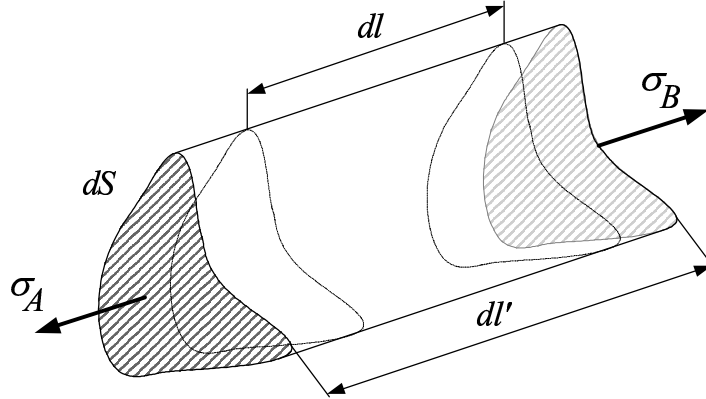
Fig. A.1. Deformation of a fiber.

$$c_{ijkl} = c_{jikl} = c_{jilk} = c_{ijlk} = c_{klij} \tag{A.16}$$

In result the number of independent components of the tensor of elastic constants is reduced from 81 to 21. There is another, frequently used more convenient system of labeling, replacing two indices by one and four indices by two

$$
\begin{aligned}
\sigma_{11} &\rightarrow \sigma_1, & \sigma_{22} &\rightarrow \sigma_2, & \sigma_{33} &\rightarrow \sigma_3, \\
\sigma_{23} = \sigma_{32} &\rightarrow \sigma_4, & \sigma_{13} = \sigma_{31} &\rightarrow \sigma_5, & \sigma_{21} = \sigma_{12} &\rightarrow \sigma_6
\end{aligned} \tag{A.17}
$$

Using the same principle of labeling for the tensor of deformations u_{mn} Hooke's law may be rewritten as

$$\sigma_M = c_{MN} u_N, \qquad M, N = 1,2,3,4,5,6. \tag{A.18}$$

where c_{mn} is a symmetric matrix of 21 elastic constants.

Considering a small slab of a cross section dA (Fig.A.1) and length dl with stresses σ_A and σ_B on its surfaces along the slab a net force acting on the slab is given by

$$dF_i = \left(\vec{\sigma}_A - \vec{\sigma}_B \right)_i dA = \frac{\partial \sigma_{ik}}{\partial x_k} dl dA = \frac{\partial \sigma_{ik}}{\partial x_k} dV \tag{A.19}$$

Taking into account a body forces Newton's law for an element dV of a solid gives

$$dm \frac{\partial^2 u_i}{\partial t^2} = \rho dV \frac{\partial^2 u_i}{\partial t^2} = dV \frac{\partial}{\partial x_k} \sigma_{ik} + f_i dV = dF_i \tag{A.20}$$

and the motions of the solid describes by the following equation

$$\rho \frac{\partial^2 u_i}{\partial t^2} = \frac{\partial}{\partial x_k} \sigma_{ik} + f_i \tag{A.21}$$

where ρ is the mass density and f_i is the resultant of body forces per unit of volume.

There is a dependence between the elastic constants and the deformation's energy W per unit of volume of the solid:

$$W = \frac{1}{2}\sum_{ijkl} c_{ijkl} u_{ij} u_{kl} \tag{A.22}$$

The symmetry of a solid can provide some simplification and reduce the number of elastic constants c_{mn}.

In the case of hexagonal symmetry this number is reduced down to five:

$$c_{mn} = \begin{bmatrix} c_{11} & c_{12} & c_{13} & 0 & 0 & 0 \\ c_{12} & c_{11} & c_{13} & 0 & 0 & 0 \\ c_{13} & c_{13} & c_{33} & 0 & 0 & 0 \\ 0 & 0 & 0 & c_{44} & 0 & 0 \\ 0 & 0 & 0 & 0 & c_{44} & 0 \\ 0 & 0 & 0 & 0 & 0 & \frac{1}{2}(c_{11} - c_{12}) \end{bmatrix} \tag{A.23}$$

For the case of cubic symmetry the tensor is invariant with respect to a cyclic permutation of the axes and only three independent elastic constants remain if the reference frame coincides with the symmetry axes of the material (c_{11}, c_{12} and c_{44}):

$$c_{mn} = \begin{bmatrix} c_{11} & c_{12} & c_{12} & 0 & 0 & 0 \\ c_{12} & c_{11} & c_{12} & 0 & 0 & 0 \\ c_{12} & c_{12} & c_{11} & 0 & 0 & 0 \\ 0 & 0 & 0 & c_{44} & 0 & 0 \\ 0 & 0 & 0 & 0 & c_{44} & 0 \\ 0 & 0 & 0 & 0 & 0 & c_{44} \end{bmatrix} \tag{A.24}$$

For isotropic media the elastic properties are invariant in respect to any rotations of a reference frame and there is an additional dependence for these components of the tensor of elastic constants:

$$c_{44} = \frac{c_{11} - c_{12}}{2} . \tag{A.25}$$

Therefore the necessary number of constants is reduced to two. The components c_{12} and c_{44} are known as the Lamè constants λ and μ, respectively. The third component c_{11} is expressed as a sum of the previous two:

$$c_{12} = \lambda, \quad c_{44} = \mu, \quad c_{11} = \lambda + 2\mu . \tag{A.26}$$

They are closely related to other elastic constants, Young's modulus Y, shear modulus G and Poisson ratio ν:

$$\lambda = \frac{Y \cdot v}{(1 + v)(1 - 2v)} \qquad\qquad \mu = G = \frac{Y}{2(1 + v)}$$

$$Y = \frac{\mu(3\lambda + 2\mu)}{\lambda + \mu} \qquad\qquad v = \frac{\lambda}{2(\lambda + \mu)} \tag{A.27}$$

The Hook's law for an isotropic solid can be expressed via the Lamè constants as:

$$\sigma_{ik} = \lambda \sum_{n} u_{nn} \delta_{ik} + 2\mu u_{ik} \tag{A.28}$$

B. Calculation of the temperature rise in a sample and the normal surface displacement during ion irradiation

For calculation of the temperature rise in a solid a finite element method or finite difference method can be employed. As the geometry has an axial symmetry this problem can be simplified to two dimensions using cylindrical coordinates (r, φ, z), where the temperature is a function of two space coordinates r, z and time t, $T = T(r,z,t)$. A disc like sample with radius R and thickness L was taken. The thermal diffusion equation (3.16) in the cylindrical coordinates is

$$\frac{\partial}{\partial t}T(r,z,t) = \frac{1}{\rho C_p}\left[Q(r,z,t) + \kappa\left(\frac{\partial^2 T}{\partial r^2} + \frac{\partial T}{r\partial r} + \frac{\partial^2 T}{\partial z^2}\right)\right] \tag{B.1}$$

$$0 \le r \le R, \quad 0 \le z \le L, \quad 0 \le t \le t_{\max}, \quad T(r,z,0) = T_0$$

with the following boundary conditions

$$\frac{\partial}{\partial r}T(R,z,t) = 0, \quad \frac{\partial}{\partial r}T(0,z,t) = 0, \quad \frac{\partial}{\partial z}T(r,0,t) = 0, \quad \frac{\partial}{\partial z}T(r,L,t) = 0, \tag{B.2}$$

which express absence of any heat diffusion from the sample surface. In the case of strong heating with high temperature rise it is necessary to take into account thermal radiation from the surfaces according to Stefan-Boltzmann law.

Using an explicit finite difference scheme the thermal diffusion equation can be written as

$$T_{m,n}^{k+1} - T_{m,n}^{k} \approx \frac{\delta t}{\rho C_p}\left[Q_{m,n}^{k} + \kappa\left(\frac{T_{m+1,n}^{k} - 2T_{m,n}^{k} + T_{m-1,n}^{k}}{\delta r^2} + \frac{T_{m+1,n}^{k} - T_{m-1,n}^{k}}{2r_m \delta r} + \frac{T_{m,n+1}^{k} - 2T_{m,n}^{k} + T_{m,n-1}^{k}}{\delta z^2}\right)\right] \tag{B.3}$$

The grid parameters for this scheme are taken

$$r_m = m \cdot \delta r, \qquad z_n = n \cdot \delta z, \qquad t_k = k \cdot \delta t,$$

$$k = 0, 1, 2, ..., \mathrm{K} \quad m = 1, 2, ..., \mathrm{M} \quad n = 1, 2, ..., \mathrm{N} \tag{B.4}$$

The scheme has a stable solution if $\delta t < \left(\dfrac{2}{\delta r^2} + \dfrac{2}{\delta z^2} \right)^{-1} \cdot \dfrac{\rho C}{\kappa}$.

In the finite element method is employed the sample can be decomposed to ring-shaped elements with radial and axial thickness δr and δz, respectively, where the temperature change δT during the time step δt is caused by the heat power density $Q(r,z,t)$ and by the heat diffusion from this element to the adjacent ones

$$\delta T(r,z,t) = \frac{1}{\rho C_p \cdot \delta V} \left(Q(r,z,t) \cdot \delta V - \kappa \sum_i S_i \frac{T(r,z,t) - T_i}{l_i} \right) \delta t \qquad \text{(B.5)}$$

$$T(r,z,t_{n+1}) = T(r,z,t_n) + \delta T(r,z,t_n), \quad t_n = n \cdot \delta t$$

where $\delta V = 2\pi r \delta r \delta z$ is the volume of the element, T_i is the temperature of the i-th adjacent element, S_i the area between the element and the adjacent one, l_i is the distance between them. The volume where the temperature changes during some microseconds is much smaller than the sample, so only a small volume around the heated point in the sample may be used in order to reduce the number of the finite elements and to shorten the calculation time.

Calculation of the elastic deformation can be also done using finite difference method [49]. As the temperature field has cylindrical symmetry the displacement field is expected to be also symmetric. The displacement occurs in two directions only, r and z, i. e. the vector of displacements has only two components, $\vec{u} = (u_r, 0, u_z)$. Moreover, the components are functions of r, z and t and do not depend on the polar angle φ. In this case the components of the strain tensor are:

$$u_{rr} = \frac{\partial}{\partial r} u_r, \qquad u_{\varphi\varphi} = \frac{1}{r} u_r, \qquad u_{zz} = \frac{\partial}{\partial z} u_z,$$

$$u_{r\varphi} = 0, \qquad u_{\varphi z} = 0, \qquad u_{rz} = \frac{1}{2} \left(\frac{\partial}{\partial r} u_z + \frac{\partial}{\partial z} u_r \right) \qquad \text{(B.6)}$$

and the components of the stress tensor:

$$\sigma_{rr} = \lambda \left(u_{rr} + u_{\varphi\varphi} + u_{zz} \right) + 2\mu u_{rr}$$

$$\sigma_{\varphi\varphi} = \lambda \left(u_{rr} + u_{\varphi\varphi} + u_{zz} \right) + 2\mu u_{\varphi\varphi}$$

$$\sigma_{zz} = \lambda \left(u_{rr} + u_{\varphi\varphi} + u_{zz} \right) + 2\mu u_{zz} \qquad \text{(B.7)}$$

$$\sigma_{r\varphi} = 0, \quad \sigma_{\varphi z} = 0, \quad \sigma_{rz} = 2\mu u_{rz}$$

Substituting the Eq.(B.7) in the equation of motion (A.21) and assuming the Lamè coefficient to be constant one can obtain the following equations for two components of the vector of displacements:

$$2\mu\frac{\partial^2}{\partial r^2}u_r + \mu\frac{\partial^2}{\partial z^2}u_r + \mu\frac{\partial^2}{\partial z\partial r}u_z + \lambda\frac{\partial}{\partial r}u_{kk} + 2\mu\frac{1}{r}\left(\frac{\partial}{\partial r}u_r - \frac{u_r}{r}\right) + f_r = \rho\frac{\partial^2}{\partial t^2}u_r$$

$$2\mu\frac{\partial^2}{\partial z^2}u_z + \mu\frac{\partial^2}{\partial r^2}u_z + \mu\frac{\partial^2}{\partial z\partial r}u_r + \lambda\frac{\partial}{\partial z}u_{kk} + \mu\frac{1}{r}\left(\frac{\partial}{\partial z}u_r + \frac{\partial}{\partial r}u_z\right) + f_z = \rho\frac{\partial^2}{\partial t^2}u_z$$

(B.8)

where u_{kk} means a sum of all diagonal components of the strain tensor. The boundary conditions are:

$$u_r(0,z,t) = 0, \quad \frac{\partial}{\partial r}u_z(0,z,t) = 0,$$

$$\sigma_{zz}(r,0,t) = 0, \quad \sigma_{rz}(r,0,t) = 0, \quad \sigma_{zz}(r,L,t) = 0, \quad \sigma_{rz}(r,L,t) = 0,$$

$$\sigma_{rr}(R,z,t) = 0, \quad \sigma_{rz}(R,z,t) = 0.$$

(B.9)

The vector of force density, which has also only two components due to symmetry, f_r and f_z is proportional to the gradient of temperature:

$$f_r = -\alpha(3\lambda + 2\mu)\frac{\partial}{\partial r}T(r,z,t)$$

$$f_z = -\alpha(3\lambda + 2\mu)\frac{\partial}{\partial z}T(r,z,t)$$

(B.10)

The derivatives of the components of the vector of displacement and temperature are approximated by the following expressions:

$$\frac{\partial}{\partial r}y(r_m,z_n,t_k) \approx \frac{y_{m+1,n}^k - y_{m-1,n}^k}{2\delta r}, \qquad \frac{\partial}{\partial z}y(r_m,z_n,t_k) \approx \frac{y_{m,n+1}^k - y_{m,n-1}^k}{2\delta z},$$

$$\frac{\partial^2}{\partial r^2}y(r_m,z_n,t_k) \approx \frac{y_{m+1,n}^k - 2y_{m,n}^k + y_{m-1,n}^k}{\delta r^2}, \quad \frac{\partial^2}{\partial z^2}y(r_m,z_n,t_k) \approx \frac{y_{m,n+1}^k - 2y_{m,n}^k + y_{m,n-1}^k}{\delta z^2}, \quad (B.11)$$

$$\frac{\partial^2}{\partial z\partial r}y(r_m,z_n,t_k) \approx \frac{y_{m+1,n+1}^k - y_{m+1,n-1}^k - y_{m-1,n+1}^k + y_{m-1,n-1}^k}{4\delta z\delta r}.$$

where y represents u_r, u_z, or T. This scheme of calculation is stable if $\delta r = \delta z$ and:

$$\frac{\delta t^2\mu}{\rho}\left[\frac{1}{\delta z^2} + \frac{1}{\delta r^2} + \left(1 + \frac{\lambda}{\mu}\right)\frac{1}{\delta r^2}\right] < 1, \quad \frac{\delta t^2\mu}{\rho}\left[\frac{1}{\delta z^2} + \frac{1}{\delta r^2} + \left(1 + \frac{\lambda}{\mu}\right)\frac{1}{\delta z^2}\right] < 1. \quad (B.12)$$

The temperature rise and surface displacement were calculated using C++ code.

C.   Signal preamplifier

For carrying out waveform measurements of an acoustic signal generated by a pulsed ion beam it was necessary to construct a preamplifier which combines a high amplification factor and a wide frequency bandwidth. This device should operate at frequencies up to 10 MHz in order to provide the time resolution of about 100-200 ns.
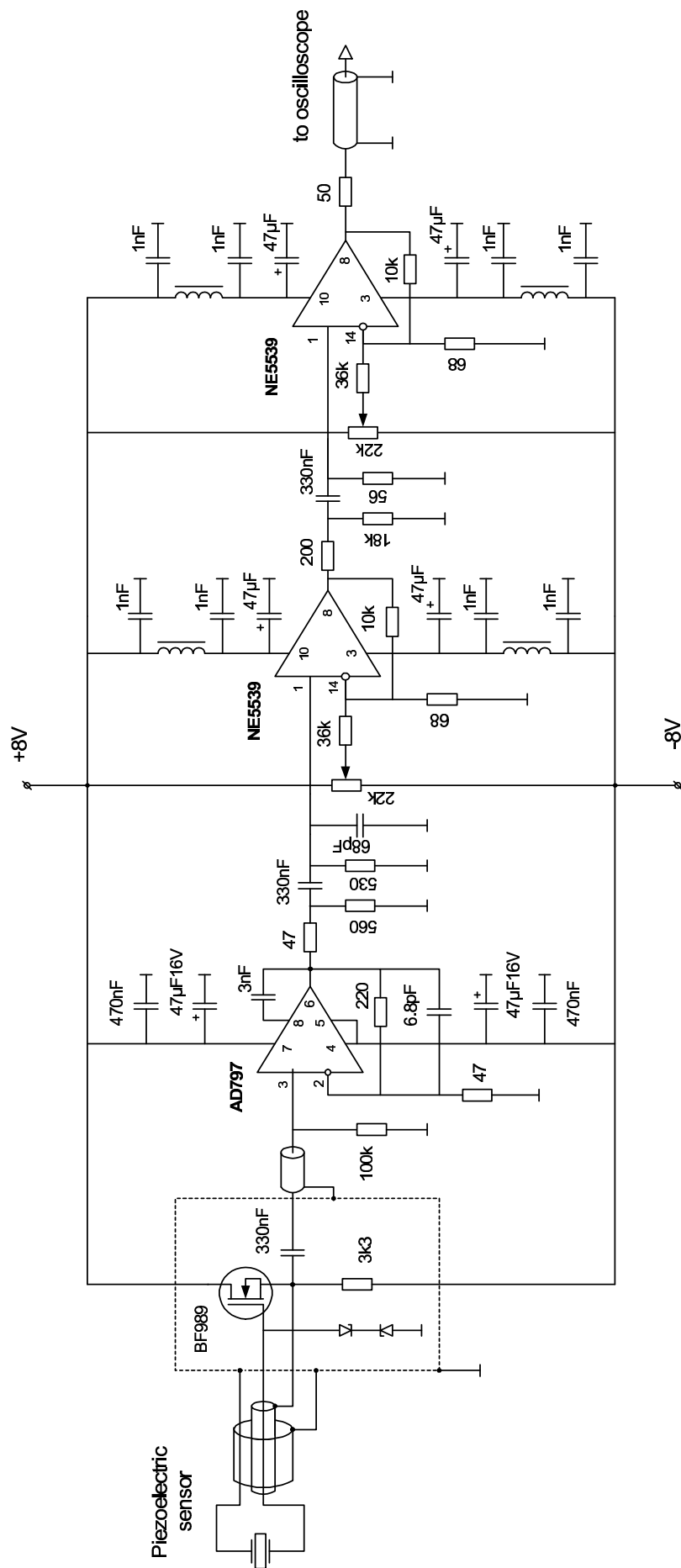
Fig. C.1. The signal preamplifier schematic.

The preamplifier is based on high frequency operational amplifiers (OA) and a FET transistor (Fig.C.1). The input cascade is based on BF989 low-nose N-channel MOS-FET transistor. The transistor is installed in common drain mode. For connecting of the sensor with the preamplifier a double screened cable is used. The outer shield of the cable is grounded, but the internal screening shield is connected with the source of the FET transistor. In this manner the potentials on the central wire and the internal shield are equal due to unity voltage amplification of the input cascade and the voltage between them is equal to zero, therefore the capacitance between the internal shield and central wire is deactivated, and there is enough current coming from the source of the transistor for driving of the capacitance between the inner and outer shields. This provides a high input resistance of the device and simultaneously reduces a parasitic influence of the cable capacitance. The next cascade of the preamplifier is based on a low noise operational amplifier AD797 with a typical spectral density of the input noise voltage of about $0.9\,\mathrm{nVrms}/\sqrt{\mathrm{Hz}}$. This value is equivalent to the thermal noise of 50 Ω resistor. The unity frequency of this OA is about 80 MHz. In order to have the output nose of the second cascade lower than that of the next cascade the amplification factor was taken of $4-5$, corresponding to the noise spectral density on the output of AD797 of about 4 nV/Hz$^{1/2}$ and the -3 dB frequency limit of 16 MHz. The last two cascades are based on high frequency OA NE5539. This OA has a higher input noise than AD797, about $5\,\mathrm{nVrms}/\sqrt{\mathrm{Hz}}$, but a broad frequency bandwidth of 1.2 GHz, which can permit an amplification up to 150 for a signal with frequency of 8-10 MHz. For improving stability of the scheme and removing of the parasitic positive feedback separating filters are introduced between the operational amplifiers. The final amplification was measured to be about 20000 ($\approx$86 dB) in a frequency band from 500 Hz up to 8 MHz (Fig. 4.13a).

D. A model of the piezoelectric sensor

For calculations the sensor was assumed to consist of three layers, a front electrode, a piezoelement and a damping back electrode (Fig. D.1). This layered structure is pressed onto the sample surface from backside by a force *F*. The motion of the surface of the investigated sample is assumed to be homogeneous along the sensor, i. e. the acoustic wave in the sample near the sensor represents a plane wave. The wave is transmitted
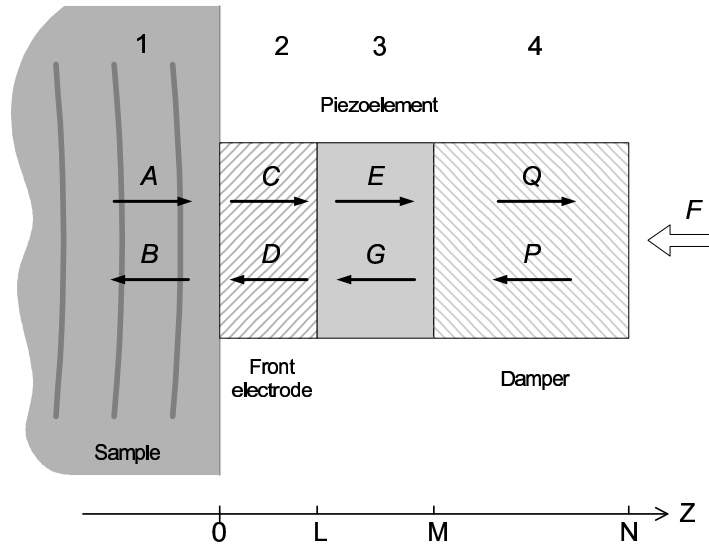
Fig. D.1. A simplified model of the piezoelectric sensor.

through and reflected from the interfaces between these layers which leads to a change of their thickness. For a piezoelectric material the governing equations are:

$$\sigma_{ij} = c_{ijkl}^E u_{kl} - e_{kij} E_k$$
$$D_i = e_{ikl} u_{kl} + \varepsilon_{ik}^S E_k \tag{D.1}$$

where e_{ikl}, ε_{ik} are the piezo electric and the dielectric constants, E_k and D_i are the electric field and the displacement, respectively. The superscripts S and E denote that the elestic constants and the permittivity must be measured at a constant strain and electric field. In the case of the simplified one dimensional model of the piezoelectric sensor which was used for the estimation of the expected electric response the equations have the following expression:

$$\sigma_{zz} = c_{3333}^E \frac{\partial u_z}{\partial z} - e_{333} \cdot E_z$$
$$D_z = \varepsilon_{33}^S E_z + e_{333} \cdot \frac{\partial u_z}{\partial z} \tag{D.2}$$

To find the voltage signal coming from the sensor, the electric field E_z has to be integrated:

$$E_z = \frac{D_z}{\varepsilon_{33}^S} - \frac{e_{333}}{\varepsilon_{33}^S} \cdot \frac{\partial u_z}{\partial z}$$
$$U = -\int_{z_1}^{z_2} E_z dz \tag{D.3}$$

In the dynamic case the electric displacement vector $\vec{D}$, not $\vec{E}$, is constant in a piezoelement because inside of the piezolayer:

$$div\vec{D} = \rho_e = 0 \tag{D.4}$$

is valid, where ρ_e is the free electric charge density. For the one-dimensional case this means that D is constant in z.

After substituting Eq.(D.3) in Eq.(D.2) the stress is given by:

$$\sigma_{zz} = \left(c_{3333}^E + \frac{e_{333}^2}{\varepsilon_{33}^S} \right) \frac{\partial u_z}{\partial z} - \frac{e_{333}}{\varepsilon_{33}^S} \cdot D_z = c_{3333}^D \frac{\partial u_z}{\partial z} - \frac{e_{333}}{\varepsilon_{33}^S} \cdot D_z \tag{D.5}$$

where the elastic constant c_{3333}^D is measured at constant D.

So the integral of the electric field Eq.(D.3) yields:

$$U = -\frac{D_z}{\varepsilon_{33}^S} \cdot (z_2 - z_1) + \frac{e_{333}}{\varepsilon_{33}^S} \left[u_z(z_2) - u_z(z_1) \right] \tag{D.6}$$

The first term in this expression is an external applied electric field which is equal to 0 for the sensor, therefore the voltage is proportional to the thickness change δu of the piezoelement:

$$U(t) = \frac{e_{333}}{\varepsilon_{33}^S} \delta u(t) = g_{33} \cdot Y_{33} \cdot \delta u(t) \tag{D.7}$$

where Y_{33} is the Young's modulus of the piezoelement, g_{33} is the piezoelectric voltage constant.

The propagating plane wave can be split into transmitted components with amplitudes A, C, E, and Q and the reflected ones, B, D, G, and P (Fig. D.1). The displacement in the piezoelement is defined as a sum of the waves E and G:

$$u_3(x,t,\omega) = (E(\omega) \cdot e^{ik_3z} + G(\omega) \cdot e^{-ik_3z}) \cdot e^{-i\omega t} \tag{D.8}$$

where k_3 is the wave number in the piezoelement. The displacements in the sample (1) and in the other layers (2, 4) can be written in the same manner. The change of the thickness of the piezoelement is:

$$\delta u_3(t,\omega) = u_3(M,t,\omega) - u_3(L,t,\omega) \tag{D.9}$$

The amplitudes satisfy the following conditions:

$$
\begin{aligned}
u_1(0,t,\omega) &= u_2(0,t,\omega), & Y_1 \frac{d}{dx} u_1(0,t,\omega) &= Y_2 \frac{d}{dx} u_2(0,t,\omega) \\
u_2(L,t,\omega) &= u_3(L,t,\omega), & Y_2 \frac{d}{dx} u_2(L,t,\omega) &= Y_3 \frac{d}{dx} u_3(L,t,\omega) \\
u_3(M,t,\omega) &= u_4(M,t,\omega), & Y_3 \frac{d}{dx} u_3(M,t,\omega) &= Y_4 \frac{d}{dx} u_4(M,t,\omega) \\
Y_4 \frac{d}{dx} u_4(N,t,\omega) &= \frac{F}{S} &&
\end{aligned}
\tag{D.10}
$$

where Y_i is Young's modulus of elasticity for each layer, S is the surface area of the damper at $x=N$. The acoustic wave number is defined by the sound velocity c, angular frequency ω and the damping length γ:

$$k = \frac{\omega}{c} + i \cdot \frac{1}{\gamma} \qquad\qquad (D.11)$$

The displacement in the sample is:

$$u_1(x,t,\omega) = (A(\omega) \cdot e^{ik_1 x} + B(\omega) \cdot e^{-ik_1 x}) \cdot e^{-i\omega t} \qquad\qquad (D.12)$$

The surface motion $h(t)$ of the sample is a Fourier integral of the plane waves:

$$h(t) = \int u_1(0,t,\omega)d\omega = \int (A(\omega) + B(\omega)) \cdot e^{-i\omega t} d\omega \qquad\qquad (D.13)$$

Using Eq.(D.10) and an inverse Fourier transformation from Eq.(D.9) one can obtain all amplitudes as functions of the frequency and find the deformation of the piezoelement as a function of time:

$$\delta u(t) = \int \delta u_3(t,\omega)d\omega = \int (E(\omega) \cdot (e^{ik_3 M} - e^{ik_3 L}) + G(\omega) \cdot (e^{-ik_3 M} - e^{-ik_3 L}))e^{-i\omega t} d\omega \quad (D.14)$$

The signals calculated for 1 mm thick PZT ceramic and 25 μm thick PVDF film and the expected surface motion of the sample $h(t)$ are shown in Fig. 4.11. It was assumed that the sensor is small and makes no significant distortion of the sample surface motion. These curves were calculated using MathCAD. The sensitivity of the sensor (deformation of the piezoelement) depends on the elastic properties of the sample.

References

[1] R. M. White, Generation of Elastic waves by transient surface heating, *J. Appl. Phys.* **34** (1963) 3559.

[2] T. H. P. Chang, Proximity effect in electron beam lithography, *J. Vac. Sci. Technol.* **12** (1975) 1271.

[3] L. R. F. Rose, Point-source representation for laser generated ultrasound, *J. Acoust. Soc. Am.* **75** (1984) 723.

[4] P. A. Doyle, On epicentral waveforms for laser generated ultrasound, *J. Phys. D: Appl. Phys.* **19** (1986) 1613.

[5] D. A. Hutchins, Ultrasonic generation by pulsed lasers, *Physical Acoustics* **18** (ed. by W. P. Mason and R. N. Thurston), Academic Press Inc. (1988) 21.

[6] F. Alan and G. C. Wetsel, Photothermal and photoacoustic effects in condensed matter, *Physical Acoustics* **18** (ed. by W. P. Mason and R. N. Thurston), Academic Press Inc. (1988) 167.

[7] D. A. Hutchins, D. E. Wilkins, Elastic waveforms using laser generation and electromagnetic acoustic transducer detection, *J. Appl. Phys.* **58** (1985) 2469.

[8] D. A. Hutchins, D. E. Wilkins, Polarized shear waves using laser line sources and electromagnetic acoustic transducer detection, *Appl. Phys. Lett.* **47** (1985) 789.

[9] R. J. Dewhurst, D. A. Hutchins, S. B. Palmer, and C. B. Scruby, Quantitative measurements of laser-generated acoustic waveforms, *J. Appl. Phys.* **53** (1982) 4064.

[10] K. Kimura, K. Nakanishi, A. Nishimura, M. Mannami, Acoustic Radiation Induced by Intensity Modulated Ion Beam, *Jap. J. Appl. Phys.* **24** (1985) L449.

[11] T. Kambara, Y. Kanai, T. M. Kojima, Y. Nakai, A. Yoneda, K. Kageyama, Y. Yamazaki, Acoustic emission from fast heavy-ion irrediation on solids, *Nucl. Inst. Meth. Phys. Res.* **B164-165** (2000) 415.

[12] C. B. Scruby, R. J. Devhurst, D. A. Hutchins, and S. B. Palmer; Quantitative studies of thermally generated elastic waves in laser irradiated metals, *J. Appl. Phys.* **51** (1980) 6210.

[13] D. N. Rose, H. Turner, and K. O. Legg, Ion acoustic microscopy, *Can. J. Phys.* **64** (1986) 1284.

[14] J. Teichert, L. Bischoff, B. Köhler, Evidence for acoustic waves induced by focused ion beams, *Appl. Phys. Lett.* **69** (1996) 1544.

[15] B. C. Deemer, A study of the acoustic signal generated by pulse-modulated ion beams incident on an aluminum target, *PhD dissertation*, The John Hopkins University (1996).

[16] F. Alan McDonald, On the calculation of laser-generated ultrasound pulses, *J. Nondestr. Eval.* **9** (1990) 223.

[17] E. Fermi, A statistical method for the determination of some atomic properties and the application of this method to the theory of the periodic system of elements, *Z. Phys.* **48** (1928) 73.

[18] O. B. Firsov, Rasseianie ionov na atomah, *Zh. Eksp. Teor. Fiz.* **34** (1958) 447.

[19] A. Sommerfeld. Asymptotische Integration der Differentialgleichung des Thomas-Fermischen Atoms, *Z. f. Phys.* **78** (1932) 283.

[20] J. Lindhard, V. Nielsen and M. Scharff, *Mat. Fys. Medd. Dan. Selk.* **36** (1968) 10.

[21] G. Molier, Theorie der Streuung schneller geladener Teilchen I: Einzelstreuung am abgeschirmten Coulomb-Feld, *Z. Naturforschung* **2a** (1947)133.

[22] N. Bohr, The penetration of atomic particles through matter, *Mat. Fys. Medd.* **18** (1948) 19.

[23] M. T. Robinson and I. M. Torrens, Computer simulation of atomic-displacement cascades in solids and in the binary collision approximation, *Phys. Rev.* **B 9** (1974) 5008.

[24] J. Lindhard and M. Scharff, Energy dissipation by ions in the keV region, *Phys. Rev.* **124** (1961)128.

[25] J. P. Biersack and D. Fink, Implantation of boron and lithium in semiconductors and metals, *Ion implantation in semiconductors* (ed. By S. Namba,), 211-218, Plenum Press (1975).

[26] H. H. Andersen, C. C. Hanke, H. Sørensen, P. Vajda P, Stopping power of Be, Al, Cu, Ag, Pt and Au for 5-12 MeV protons and deuterons, *Phys. Rev.* **153** (1968) 338.

[27] J. Lindhard, M. Scharff and H. E. Schiott, Range concepts and heavy ion ranges, *Mat. Fys. Medd. Dan. Vid. Selsk.* **33** (1963) 1.

[28] G. H. Kinchin and R. S. Pease, The displacement of atoms in solids by radiation, *Rep. Progr. Phys.* **18** (1955) 1.

[29] M. J. Norgett, M. T. Robinson, and I. M. Torrens, A Proposed Method of Calculating Displacement Dose Rates, *Nucl. Eng. Des.* **33** (1975) 50.

[30]   P. Sigmund, Theory of sputtering. I. Sputtering yield of amorphous polycrystalline targets, *Phys. Rev.* **184** (1969) 383.

[31]   Y. Yamamura, N. Matsunami, and N. Itoh, a new empirical formula for the sputtering yield, *Rad. Eff. Lett.* **68** (1982) 83.

[32]   J. Bohdansky, An universal relation for the sputtering yield of monoatomic solids at normal ion incidence, *Nucl. Inst. Meth. Rhys. Res.* **2** (1984) 587.

[33]   L. Bischoff, J. Teichert, Focused Ion Beam Sputtering of Silicon and Related Materials, *FZR-217* (1998).

[34]   H. Nishi, T. Inada, T. Sakury, T. Kaneda, T. Hisatsugu, and T. Furuya, Uniform doping of channeled-ion implantation, *J. Appl. Phys.* **49** (1978) 608.

[35]   R. G. Wilson, Boron, fluorine, and carrier profiles for B and BF_2 implants into crystalline and amorphous Si, *J. Appl. Phys.* **54** (1983) 6879.

[36]   D. R. Myers, R. G. Wilson, and J. Comas, *J. Vac. Sci. Technol.* **16** (1979) 1893.

[37]   C. Park, K. Klein, A. Tasch, and J. Zeigler, *J. Electrochem. Soc.* **138** (1991) 2107.

[38]   Handbook of ion implantation technology, ed. by J. F. Ziegler, Elsevier Science Publishing B. V. (1992).

[39]   L. D. Landau, E. M. Lifschitz, Theory of Elasticity, 3rd rev. enl. ed. Oxford, England: Pergamon Press, 1986.

[40]   A. I. Beltzer, *Acoustics of Solids*, Springer-Verlag Berlin (1988).

[41]   J. Rosenbaum, *Bulk acoustic wave theory and devices*, Artech House Inc. (1988).

[42]   J. P. Wolfe, *Acoustic wave propagation in solids*, Cambridge University Press (1998).

[43]   J. W. S. Rayleigh, On waves propagated along the plane surface of elastic solid, *Proc. London Math. Soc.* **17** (1887) 4.

[44]   H. Lamb, On waves in an elastic plate, *Proc. Roy. Soc. London* **A93** (1917) 114.

[45]   www.efunda.com

[46]   A. Berezovski, J. Engelbrecht, G. A. Maugin Thermoelastic wave propagation in inhomogeneous media, *Arch. Appl. Mech.* **70** (2000) 694.

[47]   K. Yoshikawa, N. Hasebe, Green's function of the displacement boundary value problem for a heat source in an infinite plane with an arbitrary shaped rigid inclusion, *Arch. Appl. Mech.* **69** (1999) 227.

[48]   A. Villarreal and J. A. Scales Distributed three-dimensional finite-difference modeling of wave propagation in acoustic media, *Computers in physics* **11** (1997) 388.

[49]   N. I. Nikitenko, *Teoria teplomassoperenosa*, Naukova Dumka, Kiev (1983).

[50]   J. E. Sinclair, Epicentre solutions for point multiple sources in an elastic half-space, *J. Phys. D: Appl. Phys.* **12** (1979) 1309.

[51]   D. J. Mous, R. Koudijs, P. Dubbelman and H.A.P. van Oosterhout, The HVEE Tandetron line: new developments and design considerations, *Nucl. Inst. Meth. Phys. Res.* **B62** (1992) 421.

[52]   M. Friedrich, W. Bürger, D. Henke, S. Turuc, The Rossendorf 3 MV Tandetron: a new generation of high energy implanters, *Nucl. Inst. Meth. Phys. Res.* **A382** (1996) 357.

[53]   L. Bischoff, E. Hesse, G. Hofmann, F. K. Naehring, W. Probst, B. Schmidt, and J. Teichert, High current FIB system for micromechanics application, *Microelectronic Engineering* **21** (1993)197.

[54]   Ch. Akhmadaliev, G. L. R. Mair, C. J. Aidinis and L. Bischoff, Frequency spectra and electrohydrodynamic phenomena in a liquid gallium field-ion-emission source, *J. Phys.* **D 35** (2002) L91.

[55]   Ch. Akhmadaliev, L. Bischoff, J. Teichert, K. Kazbekov, Ion acoustic microscope based on IMSA-100 focused ion beam system, *Vacuum* **69** (2003) 431.

[56]   Ch. Akhmadaliev, L. Bischoff, J. Teichert, K. Kazbekov, Ion acoustic microscopy for imaging of buried structures based on a focused ion beam system, *Microelectronic engineering* **57-58** (2001) 659.

[57]   D. A. Hutchins and J. D. Macphail, A new design of capacitance transducer for ultrasonic displacement detection, *J. Phys.* **E 18** (1985) 69.

[58]   C. B. Scruby, H. N. G. Wadley, A calibrated capacitance transducer for the detection of acoustic emission, *J. Phys. D: Appl. Phys.* **11** (1978) 1487.

[59]   D. A. Hutchins, Ultrasonic sensors, *From instrumentation to nanotechnology*, Gordon & Breach, London (1991) 99.

[60]   G. G. Fattinger, P. T. Tikka, Modified Mach-Zender laser interferometer for probing bulk acoustic waves, *Appl. Phys. Lett.* **79** (2001) 290.

[61]   D. A. Hutchins, D. E. Wilkins and G. Luke, Electromagnetic acoustic transducers as a wideband velocity sensors, *Appl. Phys. Lett.* **46** (1985) 634.

[62]   T. M. Jr. Proctor, An improved piezoelectric acoustic emission transducer, *J. Acoust. Soc. Am.* **71** (1982) 1163.

[63]   www.americanpiezo.com

[64]   www.piezotech.fr

[65] H. T. Soh, I. Ladabaum, A. Atalar, C. F. Quate, and B. T. Khuri-Yakub, Silicon micromachined ultrasonic immersion transducers, *Appl. Phys. Lett.* **69** (1996) 3674.

[66] S.-C. Chang and W. H. Ko, Capacitive sensors, *Sensors: A comprehensive survey* **7** (ed. by W. Göpel, J. Hesse, J. N. Zemel), VCH Verlagsgeselschaft mbH (1994) 105.

[67] B. T. Khuri-Yakub, C.-H. Cheng, F.-L. Degertekin, S. Ergun, S. Hansen, X.-C. Jin, O. Oralkan, Silicon micromachined ultrasonic transducers, *Jpn. J. Appl. Phys.* **39** (2000) 2883.

[68] A. S. Ergun, A. Atalar, B. Temerkuran and E. Özbay, A sensitive detection method for capacitive ultrasonic transducers, *Appl. Phys. Lett.* **72** (1998) 2957.

[69] T. C. Hale and K. Telschow, Optical lock-in vibration detection using photorefractive frequency domain processing, *Appl. Phys. Lett.* **69** (1996) 2632.

[70] H. Höfler and M. Seib, Optical surface morphology inspection technique, *Sensors: A comprehensive survey* **6** (ed. by W. Göpel, J. Hesse, J. N. Zemel), VCH Verlagsgeselschaft mbH (1992) 552.

[71] I. Thornton, R. Rautiu, S. Brush *LEAD: the facts*, IC Consultants Ltd., London (2001).

[72] D. Adliene, L. Pranevicius and A. Ragauskas, Acoustic emission induced by ion implantation, *Nucl. Instr. Meth.* **209/210** (1983) 357.

[73] G. E. Sieger and H. W. Lefevre, Time-resolved measurement of acoustic pulses generated by MeV protons stopping in aluminum, *Phys. Rev.* **A 31** (1985) 3929.

[74] B. Taylor, H. J. Maris, and C. Elbaum, Focuing of phonons in crystalline solidsdue to elastic anisotropy, *Phys. Rev.* **B3** (1971) 1462.

[75] Y. Sugawara, O. B. Wright, O. Matsuda, M. Takigahira, Y. Tanaka, S. Tamura, and V. E. Gusev, Watching Ripples on Crystals, *Phys. Rev. Lett.* **88** (2002) 185504-1.

[76] S. Y. Sokolov, On the problem of the propagation of ultrasonic oscillations in various bodies, *Elek. Nachr. Tech.* **6** (1929) 454.

[77] O. Mülhäuser, Verfahren zur Zustandsbestimmung von Werkstoffen, besonders zur Ermittlung von Fehlern darin, *DRP 565889* (1931).

[78] S. Y. Sokolov, *Dokl. Akad. Nauk USSR* **64** (1949) 333.

[79] F. A. Firestone, Flaw detecting device and measuring instrument, *U. S. Patent 2280226* (1940).

[80] D. O. Sproule, Improvements in or relating to apparatus for flaw detection and velocity measurements by ultrasonic echo methods, *Brit. Pat. 774675* (1952).

[81] F. Kruse, Zur Werkstoffprüfung mittels Ultraschall, *Akust. Z.* **4** (1939).

[82]   R. Pohlmann, Über die Möglichkeit einer akustischen Abbildung in Analogie zur optischen, *Z. Phys.* **113** (1939) 697.

[83]   R. A. Lemons and C. F. Quate, "Acoustic Microscope - Scanning Version," *Appl. Phys. Lett.* **24** (1974) 163.

[84]   H. K. Wickramasinghe, R. C. Bray, V. Jipson, C. F. Quate, and R. Salcedo, Photoacoustics on a microscopic scale, *Appl. Phys. Lett.* **33** (1978). 923.

[85]   R. L. Thomas, J. J. Pouch, Y. H. Wong, L. D. Favro, P. K. Kuo, A. Rosencwaig, Subsurface flaw detection in metals by photoacoustic microscopy, *J. Appl. Phys.* **51** (1980) 1152.

[86]   T. Hoshimiya, H. Endoh and Y. Hivatashi, Observation of Surface Defects using Photoacoustic Microscope and Quantitative Evaluation of Defect Depth, *Jpn. J. Appl. Phys.* **35** (1996) 3172.

[87]   C. F. Quate, A. Atalar, and H. K. Wickramasinghe, Acoustic Microscopy with Mechanical Scanning – a Review, *Proc. IEEE* **67** (1979)1091.

[88]   I. R. Smith, H. K. Wickramasinghe, G. W. Farnell, and C. K. Jen, Confocal surface acoustic wave microscopy, *Appl. Phys. Lett.* **42** (1983) 411.

[89]   C. F. Quate, Acoustic microscopy, *Physics Today* **8** (1985) 34.

[90]   R. J. Gutfeld von and R. L.Melcher, 20 MHz acoustic wave from pulsed thermoelastic expansions of constrained structures, *Appl. Phys. Lett.* **30** (1977) 257.

[91]   E. Brandis and A. Rosencwaig, Thermal wave microscopy with electron beams, *Appl. Phys. Lett.* **37** (1980) 98.

[92]   D. G. Davies, Scanning electron acoustic microscopy and its application, *Phil. Trans. R. Soc. Lond.* **A 320** (1986) 243.

[93]   L. J. Balk Scanning electron acoustic microscopy, *Advances in Electronics and Electron Physics* **71** (ed. By P. W. Hawkes) (1988) 1.

[94]   G. S. Cagrill, Electron beam acoustic imaging, *Physical Acoustics* **18** (ed. by W. P. Mason and R. N. Thurston), Academic Press Inc. (1988) 125.

[95]   G. Busse, Imaging by optically generated thermal waves, *Phil. Trans. R. Soc. Lond.* **A 320** (1986) 181.

[96]   J. C. Murphy, J. W. Maclachlan, L. C. Aamodt, Image contrast processes in thermal and thermoacoustic Imaging, *IEEE Trans. on Ultrasonics and Frequency control*, **UFFC-33, 5** (1986) 529.

[97]   T. Hoshimiya and K. Miyamoto, Photoacoustic microscope using linear motor drive pulse stages, *Jpn. J. Appl. Phys.* **39** (2000) 3172.

[98] Yoshiaki Tokunaga and Keimei Tamura, Study of New Technique for Three Dimensional Images in Photoscoustic Microscope, *Jpn. J. Appl. Phys.* **35** (1996) 2892.

[99] R. S. Gilmore, K. C. Tam, J. D. Young, and D. R. Howard, Acoustic microscopy from 10 to 100 MHz for industrial applications, *Phil. Trans. R. Soc. Lond.* **A 320** (1986) 215.

[100] K. L. Muratikov, A. L. Glazov, D. N. Rose and J. E. Dumar, Photoacoustic effect in stressed elastic solids, *J. Appl. Phys.* **88** (2000) 2948.

[101] L. Reimer, Scanning electron microscopy, Springer, Berlin, Heidelberg (1995).

[102] P. D. Prewett and G. L. R. Mair, Focused Ion Beam from Liquid Metal Ion Sources, Research Studies Press Ltd. (1991).

[103] J. Melngailis, Focused ion beam technology and applications, *J. Vac. Sci. Technol. B* **5** (1987) 469.

[104] L. Bischoff, J. Teichert, S. Hausmann, G. L. R. Mair, Investigation and optimization of emission parameters of alloy liquid metal ion sources, *Nucl. Inst. Meth. Phys. Res.* **B161-163** (2000) 11.

[105] R. C. Dorf, *The electrical engineering handbook*, CRC Press Inc., (1993)1128.

[106] W. Jackson and N. M. Amer, Piezoelectric photoacoustic detection: Theory and experiment, *J. Appl. Phys.* **51** (1980) 3343.

[107] J. Bernstein, R. Miller, W. Kelley, P. Ward, Low-noise MEMS vibration sensor for geophysical applications Technical Digest, *Solid-State Sensor and Actuator Workshop, Hilton Head Island, SC, June 8-11* (1998) 55.

[108] T. B. Gabrielson, Mechanical-thermal noise in micromachined acoustic and vibration sensors, *IEEE Trans. Electron Devices* **ED-40** (1993) 903.

[109] R. L. Weaver and O. I. Lobkis, Ultrasonics without a source: Thermal fluctuation correlation at MHz frequencies, *Phys. Rev. Lett.* **87** (2001) 134301-1.

[110] B. Schmidt, L. Bischoff, J. Teichert, Writing FIB implantation and subsequent anisotropic wet chemical etching for fabrication of 3D structures in silicon, *Sensors and Actuators* **A 61** (1997) 369.

[111] W. Knapp, L. Bischoff, J. Teichert, Electron emission characteristics of solidified gold alloy liquid metal ion sources, *Appl. Surf. Sci.* **146** (1999) 134.

Acknowledgements

Erklärung

Hiermit versichere ich, dass ich die vorliegende Arbeit ohne zulässige Hilfe Dritter und ohne Benutzung anderer als der angegebenen Hilfsmittel angefertigt habe. Die aus fremden Quellen direkt oder indirekt übernommen Gedanken sind als solche kenntlich gemacht. Die Arbeit wurde bisher weder im Inland noch im Ausland in gleicher oder ähnlicher Form einer anderen Prüfungsbehörde vorgelegt.

Diese Dissertation wurde im Institut für Ionenstrahlphysik und Materialforschung im Forschungszentrum Rossendorf unter der wissenschaftlichen Betreuung von Dr. Lothar Bischoff und Prof. Dr. Manfred Helm angefertigt.

Die Promotionsordnung der Fakultät für Mathematik und Naturwissenschaften der Technischen Universität Dresden vom 20. März 2000 erkenne ich an.

Dresden, den 28. März 2004